Effects of increasing aerothermodynamic fidelity on hypersonic trajectory optimisation for flight testing purposes

J. van Oostrom

January 9, 2015

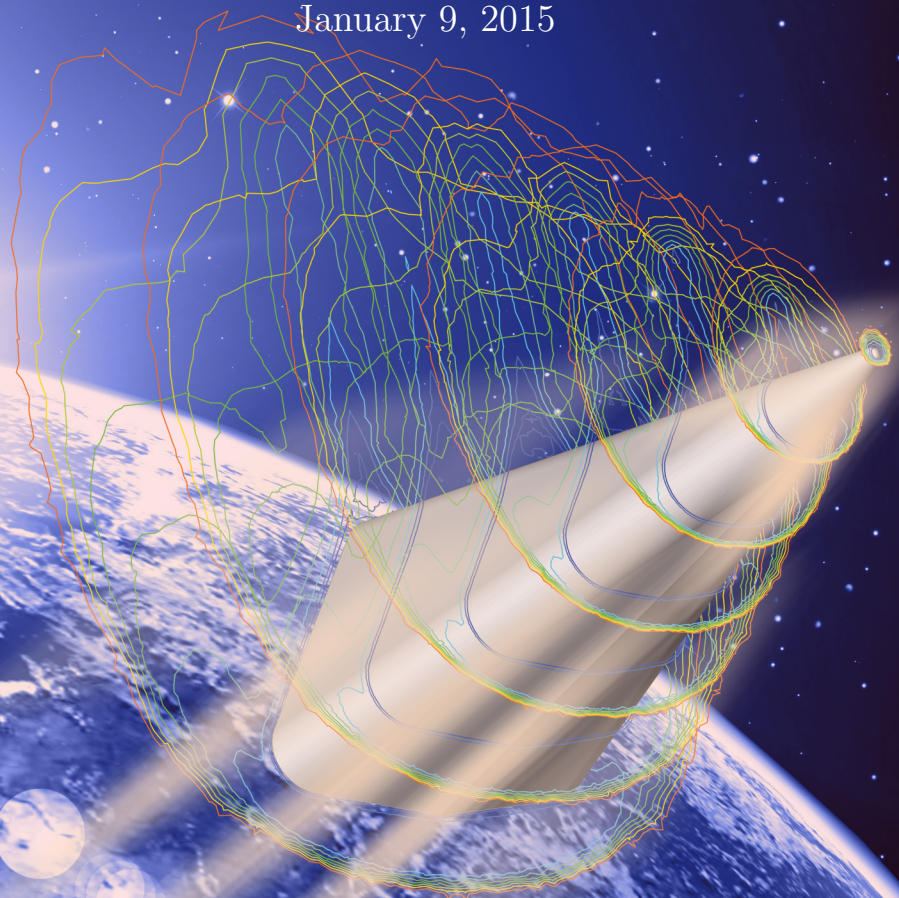

Aerodynamics

Faculty of Aerospace Engineering

TU Delft

Delft University of Technology

Effects of increasing aerothermodynamic fidelity on hypersonic trajectory optimisation for flight testing purposes

Master of Science Thesis

For obtaining the degree of Master of Science in Aerospace Engineering
at Delft University of Technology

J. van Oostrom

January 9, 2015

Faculty of Aerospace Engineering · Delft University of Technology

Delft University of Technology

Preface

I present to you my master thesis report. The last 10 months, I have been working on my research project, combining aerodynamics with elements of re-entry mechanics. This report represents the research work, presenting the used methods and theories and the obtained conclusions in my work.

The report can be split up into two parts. One part that applies to hypersonic aerothermodynamics, the other part applies to trajectory optimisation. These two parts converge towards a joint conclusion. A new optimal trajectory is obtained from the combination of improved aerodynamics and the trajectory optimisation. In the appendices the numerical results that have been obtained in this thesis can be found. These results can be used for future research.

I would like to thank my supervisors, Ferry Schrijer, Erwin Mooij and Kees Sudmeijer, for sharing their knowledge and guiding me through a complete research project. The weekly meetings resulted in much laughter, something I *might* miss after my graduation. Furthermore, I express my gratitude towards my fellow graduate students in the infamous aerodynamics basement for their help and support in my thesis, as well as the great time both during working hours and outside of the office. Lastly, I would like to thank my family and my partner, for bearing with me and giving me love and support for the duration of my thesis, and beyond.

Delft,
January 9, 2015

Jeffrey van Oostrom

Summary

In a previous study, the optimal re-entry trajectory of Hyperion-2 has been derived. The mission of the vehicle is to measure hypersonic boundary-layer transition, a phenomena in which the laminar boundary layer turns into a turbulent boundary layer. This is an important feature in hypersonic flow to investigate, as it introduces peak heating and increases drag. A constant Mach 10 flight has been performed, optimising for flight time, whilst maintaining a large Reynolds number range, in which transition occurs ($Re_{trans} = 1 \times 10^6$). Hyperion-2 is a theoretical experimental vehicle studied at Delft University of Technology.

This thesis has been performed to answer the following main research question:

Compared to modified Newtonian method results, what is the effect of using Navier-Stokes based aerodynamics for Hyperion-2 on flight-experiment objectives?

This is a two-part question. One part concerns the differences between the aerodynamic coefficients and the other part concerns the differences in optimal re-entry trajectory.

The aerodynamic database that contains values for lift, drag and moment coefficients at various angles of attack and Mach numbers has, in previous work, been created using the modified Newtonian method. This is a simple engineering method, yet is widely used as conceptual design method. The present thesis aims to increase the fidelity of the database by employing a computational fluid dynamics (CFD) software package called SU^2. During a validation and verification study it was found that the software is able to accurately compute the shock characteristics (position and shape) and pressure coefficients of simple geometries. The normalised heat fluxes could be validated with wind tunnel data, however the computation of the heat flux could not be verified using theory. The error in heat flux computation has been identified in the solver architecture. SU^2 has not been proven useful for chemical reactions as for now, thus this is not taken into account. Turbulence models have also not been included in this thesis.

It has been found that the lift and drag coefficients are increased by 5% using CFD for angles of attack lower than 10°. For larger angles, the difference increases to 15% and 10% for the lift and drag coefficient respectively. The moment coefficient is 50% larger for low angles of attack using CFD compared to the modified Newtonian theory, due to the more accurate

pressure distribution on the surface. Larger angles of attack decrease the difference to 28% at 45°.

The trajectory optimisation software used in the previous and present thesis uses a three-degrees-of-freedom flight-mechanical model. The atmospheric model uses is the 1976 United States Standard Atmosphere. The optimisation algorithm is based on Differential Evolution. The entry conditions of the vehicle are the burnout conditions of the Brazilian VS-40 launcher. The optimal trajectory takes four constraints into account: controllability constraint, stagnation-point heat flux constraint, flap deflection constraint to prevent shock wave boundary layer interaction and pitch trim constraint. Three different optimal trajectories have been derived: an unconstrained trajectory, a constrained trajectory including controllability constraint and a constrained trajectory without controllability constraint.

Using either aerodynamic databases results in a similar optimal trajectory. The difference in flight time is negligible and an optimal flight time of about 31 s is achievable. The associated Reynolds sweep is 1.2025×10^7, which is an increase of 3% compared to previous work. The controllability constraint cannot be satisfied in this trajectory, resulting in a ineffective upper flap and an overeffective lower flap. The position of the centre of mass for a trimmed flight is shifted 3% towards the nose of the vehicle using the database generated by SU^2. The centre of mass position with respect to the z-direction has shifted towards the centreline of the vehicle, from 0.155 m to 0.127 m below the centreline.

Future research regarding this specific vehicle and mission should focus on improving the aerodynamic model by including heat flux computations and chemistry effects. This requires further development of SU^2. Turbulence models should also be included and a better computational mesh of Hyperion-2 must be created. The trajectory optimisation software currently models the flaps using the modified Newtonian method. The flaps should be included in the CFD model, obtaining aerodynamic coefficients at various flap deflections. Using an adjoint approach, which is present in SU^2, only a small number of computations has to be performed compared to the number of computations in present thesis.

Nomenclature

Latin Symbols

a	Temperature lapse rate	[K/m]
b	Vehicle triangular base width	[m]
c	Flap chord	[m]
C_D	Drag coefficient	[-]
C_L	Lift coefficient	[-]
C_M	Moment coefficient	[-]
C_P	Pressure coefficient	[-]
c_p	Specific heat coefficient at constant pressure	[J/(kg K)]
D	Aerodynamic drag	[N]
d	Nose diameter	[m]
E	Total energy	[J]
G	Universal gravitational constant	[m^3/(kg s^2)]
g	Gravitational acceleration	[m/s^2]
h	Enthalpy	[J/kg]
h	Vehicle triangular base height	[m]
J_i	Jeffrey constant	[-]
k	Thermal conductivity constant	[W/K]
L	Aerodynamic lift	[N]
L	Flap length	[m]
L_c	Vehicle cone length	[m]
M	Mach number	[-]
m	Mass	[kg]
p	Pressure	[N/m^2]
Pr	Prandtl number	[-]
q	Heat flux	[W/m^2]
q_r	Radiative heat flux	[W/m^2]
R	Characteristic radius	[m]
R	Specific gas constant	[J/(kg K)]

R_N	Vehicle nose radius	[m]
r_N	Vehicle triangular base radius	[m]
Re	Reynolds number	[-]
$\mathbf{r}$	Position vector	[m]
T	Temperature	[K]
t	Measurement time	[s]
$\mathbf{V}$	Velocity vector	[m/s]
$\dot{w}_i$	Species rate of change	[C/s]
x_{com}	Vehicle x-position of centre of mass w.r.t. triangular base	[m]
z_{com}	Vehicle z-position of centre of mass positive downwards	[m]

Greek Symbols

α	Angle of attack	[rad]
δ	Flap-deflection angle	[rad]
δ	Latitude	[rad]
δ	Shock stand-off distance	[m]
γ	Flight-path angle	[rad]
γ	Specific heat ratio	[-]
θ	Surface inclination angle	[rad]
θ_c	Vehicle cone angle	[rad]
θ_d	Vehicle dihedral angle	[rad]
θ_u	Vehicle upper triangular base angle	[rad]
λ	Second coefficient of viscosity	[Pa s]
μ	Dynamic viscosity	[Pa s]
ρ	Density	[kg/m^3]
σ	Bank angle	[rad]
τ	Longitude	[rad]
χ	Azimuth angle	[rad]

Subscripts

0	Initial conditions
0	Total conditions
aw	Adiabatic wall conditions
e	Boundary layer edge conditions
$f1$	Upper flap
$f2$	Lower flap
w	Wall conditions

Abbreviations

ARD	Atmospheric Re-entry Demonstrator
AUSM	Advection Upstream Splitting Method

BFD	Blunted flat plate
CC	Circular cylinder
CFD	Computation Fluid Dynamics
CFL	Courant-Friedrichs-Lewy
CGNS	CFD General Notation System
CIRA	Centro Italiano Ricerche Aerospaziali
DLR	Deutsches Zentrum für Luft- und Raumfahrt
DOF	Degree Of Freedom
ESA	European Space Agency
GUI	Graphical User Interface
HLLC	Harten-Lax-van Leer-Contact
IXV	Intermediate eXperimental Vehicle
JST	Jameson-Schmidt-Turkel
LEO	Low Earth Orbit
MDO	Multidisciplinary Design Optimisation
MPI	Message Passing Interface
MUSCL	Monotonic Upstream-Centered Scheme for Conservation Laws
NASA	National Aeronautics and Space Administration
RANS	Reynolds-Averaged Navier-Stokes
SU^2	Stanford University Unstructured
SHEFEX	SHarp Edge Flight EXperiment
TPS	Thermal Protection System
TU Delft	Delft University of Technology

Table of Contents

Chapter 1

Introduction

Imagine yourself. It is the year 2030 and you are sitting in an airplane-like vehicle. Airplane-like, since the question is, is it really an airplane? You look outside the window and you see the Earth below you. Not like when in an airplane, but different. You can actually see the curvature of the Earth. You look up and you see a display saying "Arriving in Tokyo in 30 minutes". And then you realize, you just boarded the vehicle an hour ago. In New York City.

This is the future that Ronald Reagan envisioned when he held his State of the Union in 1986 (Reagan, 1986). A new Orient Express was to take off from Dulles airport, accelerate to at least 25 times the speed of sound, and land in Tokyo, just two hours later. This is what Ronald Reagan expected by the end of the 90s. The reality is, however, that this is still not the case.

1.1 The hypersonic regime

When air flows with velocities of five times the speed of sound or higher, it is generally considered hypersonic. If Mach one is considered the speed of sound, then the hypersonic regime is defined as $M \geq 5$. The difference between hypersonic flow and supersonic flow ($1 < M < 5$) has great impact on vehicle design. For example, the shock wave that is generated will be closer to the vehicle surface, and a thick layer in which large frictional forces are present is generated. The flow has a high velocity and the kinetic energy is high. Due to the frictional forces, the air is slowed down and heat is generated. This can result in high temperatures, in the order of 10,000 K behind a normal shock (Anderson, 2006 and Gnoffo, 1999).

The high temperatures itself cause many issues that have to be overcome to achieve Ronald Reagan's vision. Materials need to be developed that can withstand the temperatures. Other techniques such as active cooling must be used to reduce the thermal stresses. Also, the vehicle

geometry plays a significant role in heat generation. A blunt body reduces the temperatures, but such a shape reduces aerodynamic performance. A perfect balance must be found to be able to cruise with high velocities through the atmosphere.

When air is heated up, the chemistry changes. Regular air is mainly dominated by concentrations of oxygen (O_2) and nitrogen (N_2). Around 800 K, air is excited due to vibrational energy, which affects gas properties. Figure 1.1 shows the ionisation and dissociation diagram of oxygen and nitrogen. At 2500 K oxygen begins to dissociate, breaking the molecule apart into two atoms (2 O). At 4000 K, nitrogen also begins to dissociate into atomic nitrogen (2 N). Finally, at 9000 K the air is completely dissociated and starts to ionise, a process where an electron (e^-) moves freely around, resulting in positively charged nitrogen and oxygen ions (N^+ and O^+). The mixture of species (N_2, N, N^+, O_2, O, O^+) has enough energy to re-

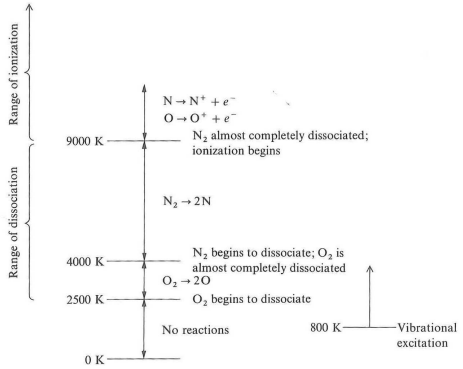

Figure 1.1: Dissociation and ionisation diagram of N_2 and O_2 (Anderson, 2006).

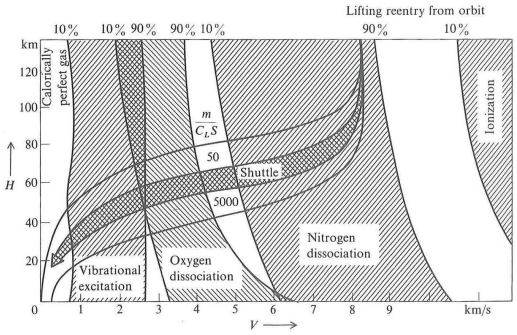

Figure 1.2: Velocity-altitude map with Shuttle re-entry corridor and areas of vibrational excitation, dissociation and ionisation (Anderson, 2006).

act with either the surface material of the vehicle or with other species itself, creating, for example, NO as well. Especially atomic oxygen is highly corrosive and is damaging to materials. The ionised species create a layer of plasma around the body, which is responsible for the communication blackout in re-entry. Figure 1.2 shows the Shuttle velocity-altitude map. Nitrogen and oxygen is already dissociated at the beginning of the trajectory ofthe Space Shuttle. When the velocity is decreased and the altitude decreases, only oxygen is still dissociated while nitrogen has recombined to nitrogen molecules. After the oxygen dissociation phase, the vibrational excited molecules are still present. In the final leg of the re-entry trajectory, the velocity and altitude are decreased to a point where no chemical effects occur. Chemically reacting flows must be taken into account when considering hypersonic flow.

The presence of different chemical species in a flow calls for a different gas model than the well-known perfect gas model. The specific heat ratio γ is not constant anymore and the value of c_p becomes dependent of temperature. Forward and backward reaction rates need to be taken into account. These reaction rates are determined experimentally and the coefficients are difficult to compute. To deal with these chemical mechanisms (nonequilibrium flow), engineering methods have been derived to either treat the chemical composition as fixed in time and space (frozen flow) or only fixed in time (equilibrium flow) (Anderson, 2006 and

Gnoffo, 1999).

1.2 Previous work

The problems described in the previous section (high heating, chemically reacting flow, the need to develop heat-resisting materials) have been identified by different research institutions, such as DLR (German space agency), ESA (European Space Agency) and NASA (United States space agency).

Research projects

Currently, DLR has a project called SHEFEX, which stands for SHarp Edged Flight EXperiment. The purpose of the project is to gain more insight into the hypersonic regime, such that more experimental data is available to validate numerical codes. The geometry is a sharp-edged vehicle with a facetted thermal protection system (TPS). The first choice is made to obtain decent propulsive and aerodynamic efficiency, however, at the cost of higher thermal loads. The TPS is chosen to investigate the ease of servicing the panels. To date, two SHEFEX vehicles have been launched and the third SHEFEX vehicle is under development and planned for launch in 2015 (Eggers et al., 2005, Weihs et al., 2008 and Weihs, 2013).

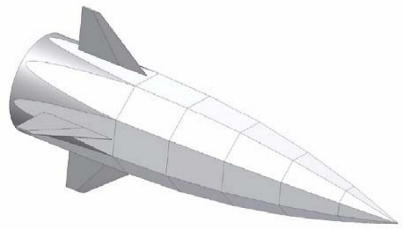

Figure 1.3: DLR SHarp Edge Flight EXperiment (SHEFEX) II geometry (Weihs et al., 2008).

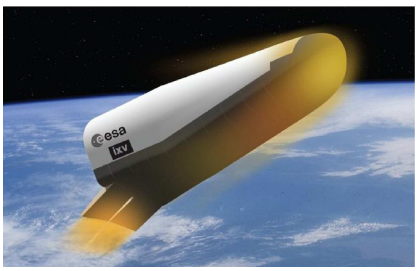

Figure 1.4: ESA Intermediate eXperimental Vehicle (IXV) rendering in re-entry (European Space Agency, 2011).

ESA is currently working on the Intermediate eXperimental Vehicle (IXV). Unlike the SHEFEX I and II, this project is focussed on controlled re-entry. It uses a lifting body and has two large body flaps to control the movement of the vehicle by banking. ESA already has performed a ballistic re-entry using the ARD (Macret and Leveugle, 1999). Using this controlled re-entry vehicle, ESA is able to get insight into the hypersonic flight regime in terms of thermal loads, gas mixture and material performance. This data can be used to validate numerical software. The IXV was to be launched in 2014, but has been postponed until a later date (Zaccagnino et al., 2011).

This thesis is based on the research project called Hyperion, designed by Sudmeijer et al. (1995). The project focuses on creating a theoretical framework for the design of low-cost

re-entry vehicles. Hyperion is a testbed that intends to develop the technology needed for a reusable launcher and re-entry vehicle, such that it is capable to fly to Low Earth Orbit (LEO) several times per week with payload. The project started with a bluntednose vehicle, called Hyperion-1. Then, complexity was increased to a sharper nose, with designation Hyperion-2. Future vehicles that will be designed may contain wings to increase lift-over-drag and controllability (Hyperion-2A).

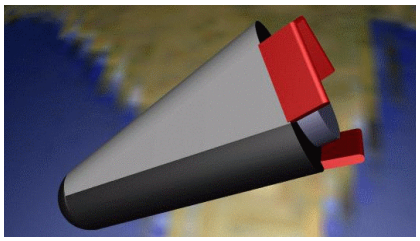

Figure 1.5: Artist impression of Hyperion-1 (Mooij et al., 1998).

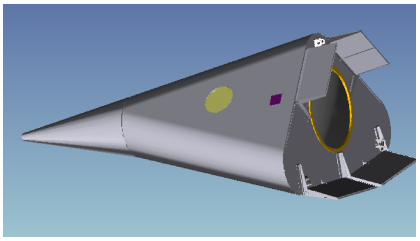

Figure 1.6: Artist impression of Hyperion-2 (Mooij et al., 1999).

Dijkstra (2012) has written a trajectory optimisation program based on the differential evolution optimisation algorithm. This software has been designed to simulate a re-entry mission of Hyperion-2. The mission is dedicated to measure hypersonic boundary-layer transition, thus a large Reynolds number range is needed, that includes the transition Reynolds number, which is in the order of 10^6. The software is based on a three degrees of freedom (DOF) flight mechanical model. It models the Earth with the 1976 United States Standard Atmosphere model. The heat flux is computed using Fay-Riddell theory. The aerodynamic coefficients are based on the Newtonian theory. This is a simplified method to compute the aerodynamic coefficients of a body (see chapter 2). Dijkstra (2012) has found that a constant Mach 10 flight is possible for 31 s with a Reynolds sweep of 12×10^6 while upholding the heat flux, maximum flap deflection to prevent shock wave boundary layer interaction, and pitch trim constraints whilst capturing transition. This is a remarkable conclusion, however, the methods used to compute the aerodynamic coefficients and heat flux may not be sufficient in detailed design of a re-entry vehicle.

Trajectory optimisation and aerodynamics

To put the work of Dijkstra (2012) and the work of the present thesis in perspective, some re-entry vehicle designs are reviewed regarding aerodynamic database creation. The design of a re-entry vehicle consists of the conceptual design phase, preliminary design phase and the detailed design phase (Hammond, 2001). In the concept design phase, multiple candidate vehicle concepts are defined given the mission requirements. The force and moment coefficients are calculated using approximate methods, which will be used to derive various trajectories for the mission. For each concept also top-level design of structural system, propulsion system, avionics and thermal protection system is performed. Once a concept is selected, the preliminary and detailed design phase starts. In these two phases the vehicle configuration is defined and refined. The aerodynamic coefficients are obtained using CFD and windtunnel tests. The aerodynamic database consists of force and moment coefficients and heating rates

by convection and radiation, for both steady and unsteady flow. The database is continuously updated as the vehicle configuration is refined. An iterative process between aerodynamics, structures, propulsion and trajectory simulation refines the configuration even further. Finally, the vehicle is tested in actual flight experiments to verify the aerodynamic parameters and the vehicle design can be refined further.

Tava and Suzuki (2002) have performed a multidisciplinary design optimisation (MDO) of a re-entry vehicle regarding shape and trajectory. The aerodynamic coefficients are computed using Newtonian theory. The heat flux has been computed using the Chapman equation and a three DOF point mass flight mechanics model is used. The exponential atmosphere model has been used to model the Earth. In this study, the approximated models for the aerodynamic coefficients have been used to reduce computational time in the conceptual design of a reentry vehicle. Using this optimisation, the baseline vehicle geometry and mission are defined. This baseline vehicle can then be used in detailed design.

In the work of Wood et al. (1996), a laminar thin-layer Navier-Stokes solver called LAURA has been used to analyse the aerodynamics of a re-entry capsule (COMET). For Mach numbers above 10, finite-rate chemistry has been included. In the conceptial work of the COMET, the modified Newtonian method has been used to compute the aerodynamic coefficients and an initial trajectory has been defined. It was found that the LAURA code predicts a 15% higher drag coefficient and a 12% higher moment coefficient. Furthermore, below Mach 10 the drag coefficient of the reacting-flow gas is 2% higher than for a perfect gas, which increases when the Mach number increases. Lastly, it was found that the effect of including the wake of the vehicle in the computational domain for small angles of attack was negligible. This study shows that there can be a large difference between approximated methods and Navier-Stokes solutions, but that for conceptual design the modified Newtonian method might just suffice to derive a baseline vehicle for detailed design.

More recently, ESA has performed an aerodynamic analysis of the IXV, as introduced earlier. The aerodynamic database has been generated using two different CFD solvers (Di Benedetto et al. (2014) and Pezzella et al. (2014)). The first is LORE which is an inhouse tool of ESA/ESTEC and TU Delft (Walpot, 2002), and the H3NS code by CIRA (Italian Aerospace Research Centre). Both solvers solve the full Navier-Stokes equations including thermochemical nonequilibrium. The numerical results have been complemented by wind tunnel experimental data to create a full aerodynamic database for the IXV.

The short review shows that different projects use different approaches when it comes to aerodynamic database generation. For conceptual design, approximate engineering methods are used as it saves computational time. However, Wood et al. (1996) shows that the aerodynamic coefficients for that particular project are higher when using full CFD simulations. This claim is supported by Meeroff (2010). The difference in aerodynamic coefficient between various methods influences the vehicle design, such that a vehicle that is designed using approximate methods might not be feasible when CFD analysis of the vehicle is performed. The detailed design phase of the IXV of ESA uses full Navier-Stokes equations, indicating that approximate methods are only suitable for conceptual design, if suitable at all. When the geometry becomes more complex, the approximate methods might not be valid, for example, when considering a vehicle including flaps.

1.3 Thesis question and goal

The description of the previous work done shows that there is still room to contribute to future research. This thesis will focus on using CFD simulation software to generate an aerodynamic database for the trajectory software by Dijkstra (2012). The database and the optimal trajectory can then be compared to the work of Dijkstra (2012), who used a modified Newtonian method. The main research question is therefore formulated as follows:

Compared to modified Newtonian method results, what is the effect of using Navier-Stokes based aerodynamics for Hyperion-2 on flight-experiment objectives?

To answer the main question, different subquestions are formulated. These subquesions give insight in smaller portions of the problem, thus contributing to the main question. The questions are formulated as follows:

1. What is the difference in aerodynamic coefficients between the two aerodynamic models?
2. What is the difference in estimated maximum heat flux and overall heat flux when comparing the aerodynamic models?
3. What is the maximum sustained Mach 10 flight time for the improved aerodynamic model given a Reynolds sweep that covers boundary-layer transition?
4. What is the largest possible Reynolds sweep within the thermal load constraints?

The final goal of the thesis is related to the work performed by Dijkstra et al. (2013). The goal of the thesis is defined as follows:

Determine what the differences are in Reynolds sweep, flight time and optimal centre of gravity position using different aerodynamic models, hereby verifying the optimal trajectory of Dijkstra et al. (2013).

The subgoals to achieve this main goal are:

1. Select and validate a suitable CFD code for high-fidelity re-entry flow simulations,
2. Generate model mesh of Hyperion-2 to be used in the CFD code,
3. Create the aerodynamic database using the CFD code,
4. Perform a trajectory optimisation with both (modified Newtonian and CFD) aerodynamic databases,
5. Compare the aerodynamic databases and optimal trajectories.

1.4 Report structure

This chapter is an introductionary chapter to the work presented in this thesis. Chapter 2 provides a detailed description of all the theoretical frameworks considered in this thesis. Section 2.1 provides the theoretical framework regarding the CFD software SU^2. The governing equations and numerical methods are presented in this section. The methods and tools regarding the trajectory optimisation of Dijkstra (2012) are reviewed in section 2.2. The aerodynamic model, time integration method, numerical optimisation method, flight mechanics and atmospheric model are presented.

Since the CFD software is an integral part in this thesis work, chapter 3 is focussed on validating the software on critical points regarding this thesis. Section 3.1 defines the validation cases, solver settings and geometries. Sections 3.2 to 3.4 shows the performance of SU^2 compared to theory and experiments on shock characteristics, pressure distribution and heat flux. Finally, in section 3.5 all information presented in chapter 3 is summarised.

With the use of SU^2 and the trajectory optimisation software by Dijkstra (2012), results regarding aerodynamic coefficients and optimal trajectory have been obtained. Chapter 4 presents these results and compares them with the previous work. First, in section 4.1 the experimental setup for both the CFD simulation software as the trajectory optimisation software will be defined. Section 4.2 shows the results of the CFD simulation using the Hyperion-2 model, presenting the aerodynamic database and validating the results by using theory. Section 4.3 compares the results from SU^2 with the modified Newtonian database. In section 4.4 the results of the trajectory optimisation software will be discussed, which will be compared to previous work of Dijkstra (2012) in section 4.5.

Finally, with all the information from chapters 2 to 4, the thesis question and subquestions can be answered. Chapter 5 summarises the answers to all these questions. Furthermore, recommendations for future research are given.

Chapter 2

Theory

This chapter summarises all theory necessary to work with and understand both the computational fluid dynamics (CFD) software SU^2 and the trajectory optimisation software by Dijkstra (2012). Section 2.1 defines the theoretical framework for SU^2, presenting a brief introduction to SU^2, physical models and numerical methods. Section 2.2 will provide theory regarding the physical model, numerical methods, flight mechanics and Earth atmosphere model used in the trajectory optimisation software.

2.1 Theoretical framework of SU^2

The first section gives a brief introduction to the capabilities of SU^2. The physical models and numerical methods that are used in SU^2 are presented after that.

2.1.1 Introduction to SU^2

SU^2 stands for Stanford University Unstructured. It is an open-source, unstructured grid, finite element or finite volume CFD solver. It is written in the C++ language and has supporting Python scripts that allow for automation of various processes and improve the ease of use. The software is able to run parallel using multiple cores or multiple machines to reduce the computation time. A Graphical User Interface (GUI) is under development, to input the solver settings and mesh files. For now, an extensive configuration file together with a mesh file either formatted in the SU^2 native format or the standardised CFD General Notation System (CGNS) is needed to get the program working.

SU^2 has many features and functions and these functions are ever increasing due to the ongoing development of the software. A few key features are listed in this section (Palacios

et al., 2013 and Palacios et al., 2014).

Solver options

SU^2 has a wide variety of solvers available. Amongst others, it has the Reynolds-Averaged Navier-Stokes equations (RANS), the laminar Navier-Stokes equations and Euler equations (both with and without chemistry). The ranges of these solvers start from subsonic and reach out to hypersonic flow. Specific solvers are able to model variations in chemistry (multi-species), which are dominantly present in hypersonic high temperature flow. It has capabilities of solving non-equilibrium flow, two-phase flows, electrodynamics and more. The software also incorporates functions to compute plasma flows.

The solver is a vertex-centered finite-volume based solver. Currently, there are six spatial discretisation schemes available, and more are in development:

- Jameson-Schmidt-Turkel (JST, centered scheme, second-order accurate)
- Lax-Friedrich (centered scheme, first-order accurate)
- Roe first-order (upwind scheme, first-order accurate)
- Roe second-order (upwind scheme, second-order accurate using MUSCL scheme and Venkatakrishnan's limiter)
- HLLC first- and second-order (approximate Riemann solver with Venkatakrishnan's limiter)
- AUSM first- and second-order (approximate Riemann solver with Venkatakrishnan's limiter)

The implicit and explicit time integration schemes are:

- Backward and forward Euler (first-order accurate)
- Runge-Kutta explicit (up to fourth-order accurate)
- Dual time stepping (second-order accurate)

Parallel computation

As mentioned in the introduction to this chapter, SU^2 is able to run the solver in parallel mode. This means that the workload of the computation is split over multiple cores. This makes the program interesting to even run on modern laptops (simple geometries).

The software uses the Message Passing Interface (MPI) standard to run the parallel computations. The protocol it uses is the OpenMPI protocol, which is also open source. While parallel

computations run smoothly on a Linux based operating system, the support for Windows is not available yet.

To access the parallel possibilities, the software has to be compiled from source, using the correct settings for parallel computations. To divide the grid into segments such that a segment can be run per core is done by METIS. Using a simple Python script, the whole domain decomposition and recomposition is done automatically. Next to the solver, also the optimisation scripts can be run in parallel.

Direct and adjoint solvers

SU² offers both direct and adjoint solvers. The first computes the flow field and is able to give values for the aerodynamic coefficients. The adjoint solver is able to calculate gradients and sensitivities of the obtained solutions. The adjoint solver is a powerful tool in optimisation processes.

Mesh adaptation and deformation

The software has built in scripts that is able to adapt the mesh in a strategic way. Using an adjoint solution it gains information about the gradients in the flow, hence enabling the code to adapt the mesh according to these gradients. This technique is interesting for shock capturing purposes and refining the mesh near the boundary layer.

SU² also has a mesh deformation solver. This program is able to deform the mesh at, for example, a flap that is deflected. It is also used in the shape optimisation algorithms. This way SU² can also be used to find the optimal shape for a given objective function.

The software is able to deliver a sliding mesh, either translational or rotational. This feature can be used in the design and analysis of a rotation propeller blade. Python scripts are available to facilitate this process.

2.1.2 Physical models

The physical models that are present in SU² are explained in detail here. First the Navier-Stokes equations are discussed, then the Euler equations are discussed.

Navier-Stokes equations

The Navier-Stokes equations are considered to be the complete governing flow equations. The equations are derived by applying the conservation laws (conservation of mass, momentum and energy) on a given control volume. Originally, the Navier-Stokes equation is the momentum equation only. Nowadays, the combination of mass, momentum and energy conservation are considered the Navier-Stokes equations. The resulting equations, including what contribution

each term provides, yield (Anderson, 2006):

$$\underbrace{\frac{\partial \rho}{\partial t}}_{\substack{\text{time rate of change} \\ \text{of mass}}} + \underbrace{\nabla \cdot (\rho \mathbf{V})}_{\substack{\text{mass flow out} \\ \text{of volume } \mathcal{V}}} = 0 \tag{2.1}$$

$$\underbrace{\frac{\partial \rho_i}{\partial t}}_{\substack{\text{time rate of change} \\ \text{of species mass}}} + \underbrace{\nabla \cdot (\rho_i \mathbf{V}_i)}_{\substack{\text{species mass flow out} \\ \text{of volume } \mathcal{V}}} = \underbrace{\dot{w}_i}_{\substack{\text{species mass rate of change} \\ \text{due to chemical reactions}}} \tag{2.2}$$

$$\begin{aligned} &\underbrace{\frac{\partial (\rho \mathbf{V})}{\partial t}}_{\substack{\text{change of momentum} \\ \text{due to unsteady} \\ \text{fluctuations}}} + \underbrace{\rho (\mathbf{V} \cdot \nabla \mathbf{V})}_{\substack{\text{momentum flow out} \\ \text{of volume } \mathcal{V}}} + \underbrace{\nabla p}_{\substack{\text{pressure force} \\ \text{on } S}} \\ &+ \underbrace{\rho \mathbf{f}}_{\substack{\text{body force}}} + \underbrace{\nabla \cdot \left[\mu \left(\frac{\partial u_i}{\partial x_j} + \frac{\partial u_j}{\partial x_i} \right) + \lambda \nabla \cdot \mathbf{V} \right]}_{\substack{\tau_{\mathbf{ij}}\text{, surface force} \\ \text{due to viscosity}}} = 0 \end{aligned} \tag{2.3}$$

$$\begin{aligned} &\underbrace{\frac{\partial (\rho E)}{\partial t}}_{\substack{\text{time rate of change} \\ \text{of energy}}} + \underbrace{\nabla \cdot (\rho \mathbf{V}) E}_{\substack{\text{energy flow out} \\ \text{of volume } \mathcal{V}}} \\ &= \underbrace{\nabla \cdot (k \nabla T)}_{\substack{\text{transport of energy} \\ \text{due to thermal} \\ \text{conductivity}}} - \underbrace{\nabla \cdot \left(\sum_i \rho_i \mathbf{V}_i h_i \right)}_{\substack{\text{transport of energy} \\ \text{due to chemical} \\ \text{diffusion}}} \\ &- \underbrace{\nabla \cdot \mathbf{q_R}}_{\substack{\text{transport of energy} \\ \text{due to radiation}}} - \underbrace{\nabla \cdot (p \mathbf{V})}_{\substack{\text{work done} \\ \text{due to pressure}}} + \underbrace{\nabla \cdot (\mathbf{V} \cdot \boldsymbol{\tau}_{ij})}_{\substack{\text{work done} \\ \text{due to viscous stresses}}} \end{aligned} \tag{2.4}$$

The Navier-Stokes equations include viscous effects, radiative effects, chemical reactions, species continuity (equation 2.2), diffusion and conduction. To fully simulate a flow, all these terms are necessary, especially for the hypersonic high temperature flow considered in this thesis. However, creating a CFD software package to take all terms into account that can be validated and verified is difficult. In addition, the computational time would increase drastically. The CFD software used in this thesis is SU^2, as introduced earlier. SU^2 has capabilities of computing chemically reacting flow, however, this feature is not fully developed

yet. Since the software is not specialised towards hypersonic flows, the following quantities from equations 2.1 to 2.4 are not included in the flow analysis of the Hyperion-2:

- Species continuity (equation 2.2),
- body force,
- transport of energy due to chemical diffusion,
- transport of energy due to radiation.

The resulting governing flow equations for the analysis of the Hyperion are as follows:

$$\frac{\partial \rho}{\partial t} + \nabla \cdot (\rho \mathbf{V}) = 0 \tag{2.5}$$

$$\frac{\partial (\rho \mathbf{V})}{\partial t} + \rho (\mathbf{V} \cdot \nabla \mathbf{V}) + \nabla p + \nabla \cdot \left[\mu \left(\frac{\partial u_i}{\partial x_j} + \frac{\partial u_j}{\partial x_i} \right) + \lambda \nabla \cdot \mathbf{V} \right] = 0 \tag{2.6}$$

$$\frac{\partial (\rho E)}{\partial t} + \nabla \cdot (\rho \mathbf{V}) E = \nabla \cdot (k \nabla T) - \nabla \cdot (p \mathbf{V}) + \nabla \cdot (\mathbf{V} \cdot \boldsymbol{\tau}_{ij}) \tag{2.7}$$

Euler equations

Before analysing Hyperion-2 (or any other test case) with the full Navier-Stokes equations, the Euler equations are used to get a good initial impression of the flow field. An Euler solution can also be used to restart a Navier-Stokes solution, to improve the convergence.

The Euler equations consist of the continuity equation, momentum equation and energy equation applied by taking the integral of these properties over a finite control volume. The partial differential equations that result from the analysis are (continuity, momentum and energy, respectively) (Anderson, 2006):

$$\frac{\partial \rho}{\partial t} + \nabla \cdot (\rho \mathbf{V}) = 0 \tag{2.8}$$

$$\frac{\partial (\rho \mathbf{V})}{\partial t} + \rho (\mathbf{V} \cdot \nabla) \mathbf{V} + \nabla p = 0 \tag{2.9}$$

$$\frac{\partial (\rho E)}{\partial t} + \nabla \cdot (\mathbf{V} (\rho E + p)) = 0 \tag{2.10}$$

These equations describe the compressible, inviscid, non-reacting flow. Diffusion, thermal conduction and radiative energy are also not included. The Euler equations are relatively easy to solve with numerical methods. These equations give an initial estimation of the flow field, although viscous effects are not modelled. These equations can be altered to include chemical reactions, by adding species continuity and reaction rates. The downside of this model is the lack of viscous effects, thus the presence of a boundary layer, which is dominantly present in hypersonic flow.

Stagnation-point heat flux: Fay and Riddell

A well-accepted engineering method to determine the stagnation point heat flux on a vehicle in a hypersonic flow is the method derived by Fay and Riddell. The equations are based on the transformed boundary layer energy equation. The assumptions associated with Fay and Riddell are (Fay and Riddell, 1958) listed below and visualised in figure 2.1.

1. The shock-layer is partially dissociated and the flow conditions at the outer edge of the boundary layer are those for local thermodynamic and chemical equilibrium. The chemical reactions only take place in the boundary layer and the thermodynamic state of the flow outside the boundary layer does not change over time.
2. Regions of nonequilibrium, equilibrium or frozen flow may be present in the boundary layer, depending on the characteristic time for a fluid element to move through the flow field (τ_f) and the characteristic time for a fluid element to reach chemical equilibrium (τ_c).
3. The inviscid velocity distribution at the outer edge of the boundary layer in the stagnation region is given by the incompressible relation:

$$u_e = ax, \qquad a = \left(\frac{du_e}{dx}\right)_s \tag{2.11}$$

4. The wall can be equilibrium catalytic or non-catalytic. That means that the surface material influences the chemical composition, such that the chemical composition at the wall are the local equilibrium values at the temperature and pressure at the wall (equilibrium catalytic) or the surface material has no influence on the chemical composition at all (non-catalytic).
5. The gas is assumed to consist of heavy particles and light particles (binary mixture, molecules or atoms). This is a simplification to diffusion, such that an average for the transport coefficients can be assumed for the molecules and atoms seperately.

The equations derived by Fay and Riddell can be divided into three specific types of flow: an equilibrium boundary layer, a frozen boundary layer with equilibrium catalytic wal and a frozen boundary layer with a non-catalytic wall. The equations yield (Fay and Riddell, 1958 and Anderson, 2006):

1. Equilibrium boundary layer (spherical nose):

$$\begin{aligned} q_w =& 0.76 Pr^{-0.6} \left(\rho_e \mu_e\right)^{0.4} \left(\rho_w \mu_w\right)^{0.1} \sqrt{\left(\frac{du_e}{dx}\right)_s} \left(h_{0_e} - h_w\right) \\ & \times \left[1 + \left(Le^{0.52} - 1\right)\left(\frac{h_D}{h_{0_e}}\right)\right] \end{aligned} \tag{2.12}$$

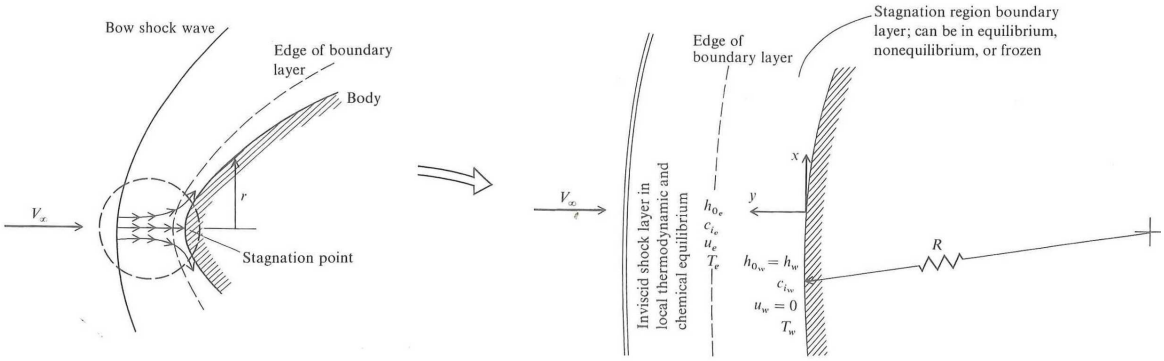

Figure 2.1: Overview of the stagnation region flow model (Anderson, 2006). The figure on the left shows the bow shock wave and the stagnation region where the shock wave can be assumed a normal shock. The figure on the right shows a close-up of the stagnation region, where outside the boundary layer an inviscid shock layer is present. In the boundary layer, equilibrium, nonequilibrium or frozen flow can be present.

2. Frozen boundary layer with an equilibrium catalytic wall (spherical nose):

$$\begin{aligned} q_w =& 0.76 Pr^{-0.6} \left(\rho_e \mu_e\right)^{0.4} \left(\rho_w \mu_w\right)^{0.1} \sqrt{\left(\frac{du_e}{dx}\right)_s} \left(h_{0_e} - h_w\right) \\ & \times \left[1 + \left(Le^{0.52} - 1\right)\left(\frac{h_D}{h_{0_e}}\right)\right] \end{aligned} \tag{2.13}$$

3. Frozen boundary layer with a non-catalytic wall (spherical nose):

$$q_w = 0.76 Pr^{-0.6} \left(\rho_e \mu_e\right)^{0.4} \left(\rho_w \mu_w\right)^{0.1} \sqrt{\left(\frac{du_e}{dx}\right)_s} \left(h_{0_e} - h_w\right) \tag{2.14}$$

The stagnation-point velocity gradient is given using a pressure distribution based on the Newtonion theory:

$$\left(\frac{du_e}{dx}\right)_s = \frac{1}{R}\sqrt{\frac{2\left(p_e - p_\infty\right)}{\rho_e}} \tag{2.15}$$

The results of Fay and Riddell will be used in this thesis to validate the heat flux computed by SU², in chapter 3.

2.1.3 Numerical methods

This section is split up in spatial discretisation and time integration methods. Spatial descretisation methods are required to cast the governing flow equations (for example Navier-Stokes)

into a discretised form for the use of CFD. Time integration methods are necessary to step through time in order to get a steady state solution using the CFD solver. First, two spatial discretisation schemes are presented, followed by various time integration methods.

Spatial discretisation

For hypersonic flow, there are two main spatial discretisation techniques for the convective fluxes that are useful; the central scheme and the upwind scheme. Both methods discretise the governing flow equations to solve the state at a certain cell vertex.

Central scheme A central scheme is based on the Taylor expansion. Performing a Taylor expansion around a first order derivative yields (Anderson, 1995, Hirsch, 2007 and Blazek, 2001):

$$\begin{aligned}\left(\frac{\partial u}{\partial x}\right)_i &= \frac{u_{i+1}-u_i}{\Delta x} - \frac{\Delta x}{2}\left(u_{xx}\right)_i - \frac{\Delta x^2}{6}\left(u_{xxx}\right)_i + \dots \\ &= \frac{u_{i+1}-u_i}{\Delta x} + \mathcal{O}\left(\Delta x\right)\end{aligned} \tag{2.16}$$

Using the same Taylor expansion, a relation for u_{i-1} can be derived:

$$\begin{aligned}\left(\frac{\partial u}{\partial x}\right)_i &= \frac{u_i-u_{i-1}}{\Delta x} + \frac{\Delta x}{2}\left(u_{xx}\right)_i + \frac{\Delta x^2}{6}\left(u_{xxx}\right)_i + \dots \\ &= \frac{u_i-u_{i-1}}{\Delta x} + \mathcal{O}\left(\Delta x\right)\end{aligned} \tag{2.17}$$

When these forward and backward difference equations are added up, the central difference equation is obtained:

$$\left(\frac{\partial u}{\partial x}\right)_i = \frac{u_{i+1}-u_{i-1}}{2\Delta x} + \mathcal{O}\left(\Delta x^2\right) \tag{2.18}$$

In the central scheme, the evaluated grid point is computed using grid points in front and behind the central point. The finite difference representation of the first derivate is of order two. The central scheme does not generate two independent solutions of the equations, which physically means that upstream variables can be changed by this scheme. This causes instability in the solution, thus artificial dissipation must be added to increase the stability. An example of a central scheme with artificial dissipation is the Jameson-Schmidt-Turkel scheme, which is also present in SU^2.

Upwind scheme Upwind schemes are biased towards computing the current grid point by using the grid points upstream of the current grid point (Anderson, 1995, Hirsch, 2007 and Blazek, 2001):

$$u_i = f\left(u_{i-1}, u_{i,2}, ..., u_{i-n}\right) \tag{2.19}$$

The upwind scheme takes into account the wave propagation direction, which the central schemes do not. This makes the upwind scheme suitable for an accurate computation of the boundary layer. For capturing discontinuities, upwind schemes are particularly interesting.

When considering supersonic flow, the information can only propagate in downstream direction, thus using only upstream values to compute a certain grid point state is valid. The downside of upwind schemes are notable in the higher-order accuracy schemes where limiters are needed to prevent oscillations near discontinuities.

Time integration

There are various numerical time integration methods available. In SU^2, the Euler method and Runge-Kutta method are considered.

Numerical integration methods are used to solve ordinary or partial differential equations. An intergration method may have either an implicit scheme, an explicit scheme or both.

Explicit schemes are generally easier to implement and to solve. For example, let x_{n+1} denote the state of a differential equation at $t = t_{n+1}$ (the new state) and x_n at $t = t_n$ (the old state). Then, for an explicit scheme, the new state would be calculated using:

$$x_{n+1} = f\left(x_n, x_{n-1}, x_{n-2}, \ldots\right) \tag{2.20}$$

Implicit schemes are more difficult to implement, as the new state is also included in the function to compute the new state. Generally speaking, implicit schemes take more time to compute, as the new state has to be computed iteratively, thus more function evaluations are necessary to compute the new state. Consider again the old and new states as mentioned above, then an implicit scheme would be:

$$x_{n+1} = g\left(x_{n+1}, x_n, x_{n-1}, \ldots\right) \tag{2.21}$$

Although explicit schemes seem more interesting since they are easier and require less computation time, implicit schemes are more stable than explicit schemes. Moreover, implicit schemes may attain a higher order of accuracy, while using a larger step size than explicit schemes. Decreasing the step size in explicit schemes to attain a higher order has a negative effect: as the error in computation decreases (truncation error), the rounding error due to the small step size increases. In this section, the explicit schemes of the integration methods are discussed.

Euler method The Euler method is the simplest integration method available. The Euler integrator is evaluated at the beginning of the step size interval. The method requires sufficient initial values to the differential equation. For example, consider an ordinary differential equation of the form (Butcher, 2008):

$$\begin{aligned} \frac{dx}{dt} = & x'(t) = \lambda(t)x(t), \quad t > 0 \\ & x(0) = c \text{ (initial condition)} \end{aligned} \tag{2.22}$$

The initial condition of $x'(t)$ can also be computed:

$$x'(0) = \lambda(0)c \tag{2.23}$$

The step size h can be the time step or the grid size. Using this step size, the time step can be written as $t_n = nh$ with $n = 1, 2, 3, \ldots$. The value for $x(t)$ will be denoted as $x(t_n) = x_n$ and $x(t_n + h) = x_{n+1}$. The Euler integration scheme has the following form:

$$\begin{aligned} t_{n+1} &= t_n + h \\ x_{n+1} &= x_n + hx'_n \\ x'_{n+1} &= \lambda_{n+1} x_{n+1} \end{aligned} \tag{2.24}$$

For small step sizes, this method proves to be rather accurate. However, as the step size is increased, the error is also increased. An advantage of the Euler method is that it is fast.

Runge-Kutta method The Runge-Kutta method is a higher order integration method. To compute a next time step, it uses information about the previous time step, similar to the Euler method. The Runge-Kutta integrator is different from the Euler method. Whereas Euler only evaluates the new time step based on information at the beginning of the step interval, the Runge-Kutta method uses information about different locations from the step interval. The general Runge-Kutta scheme is given by the following equations (Griffiths and Higham, 2010):

$$x_{n+1} = x_n + h \sum_{i=1}^{s} b_i k_i \tag{2.25}$$

Where

$$k_i = f\left(t_n + c_i h_i, x_n + h \sum_{j=1}^{s} a_{i,j} k_j\right) \tag{2.26}$$

And

$$c_i = \sum_{j=1}^{s} a_{i,j}, \quad i = 1 : s \tag{2.27}$$

In these equations s denotes the number of stages the Runge-Kutta integrator uses. The coefficients c_i, b_i and $a_{i,j}$ are, per Runge-Kutta stage, given in Butcher arrays (Butcher, 2008). The Butcher array for a full Runge-Kutta method is given in table 2.1.

Table 2.1: Butcher array for a full Runge-Kutta method (Griffiths and Higham, 2010 and Butcher, 2008).

c_1	$a_{1,1}$	$a_{1,2}$	$\ldots$	$a_{1,s}$
c_2	$a_{2,1}$	$a_{2,2}$	$\ldots$	$a_{2,s}$
$\vdots$	$\vdots$	$\vdots$		
c_s	$a_{s,1}$	$a_{s,2}$	$\ldots$	$a_{s,s}$
	b_1	b_2	$\ldots$	b_s

Many arrays are developed for different stages and orders. Even higher-order schemes (up to order 8) are available for the Runge-Kutta method.

As mentioned before, implicit methods are more difficult to implement, require more computational time and are more stable than explicit methods. Larger time steps can be taken whilst

maintaining higher order accuracy. In SU^2, the explicit Euler and Runge-Kutta schemes and implicit Euler scheme is implemented. To achieve convergence, a small time step (CFL number) is required with a fourth order Runge-Kutta explicit scheme. Due to the small time step, the order of accuracy is reduced for this method (due to rounding errors), and stability is not guaranteed. Hence, the implicit Euler method is used as a larger time stepping value can be used, the solution tends to converge and the order of accuracy remains unchanged.

2.2 Theoretical framework of the trajectory optimisation software

This section provides the theory used in the trajectory optimisation software by Dijkstra (2012). First the aerodynamic model (modified Newtonian theory) is explained. Then, the numerical methods regarding time integration and numerical optimisation are discussed, followed by flight mechanical theory. Lastly, the environment model is defined.

2.2.1 Modified Newtonian method

The simplest flow model for hypersonic flow is the Newtonian method. This method is previously used by Dijkstra (2012) to compute the aerodynamic coefficients (C_L, C_D, C_m) of Hyperion-2. The Newtonian method is very easy to use and fairly accurate for low angles of attack (Anderson, 2006). This model can be used to verify the CFD results of simple geometries (flat plate, sphere).

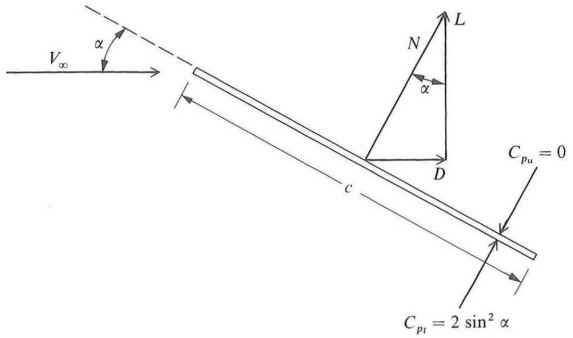

Figure 2.2: Flat plate aerodynamic forces according to Newtonian method (Anderson, 2006). At the leeward side of the flat plate, the pressure coefficient is zero.

The modified Newtonian method differs from the Newtonian method by taking into account the effect of specific heat ratio γ when determining the maximum pressure coefficient. The Newtonian method is based on the assumption that when a flow impinges a surface, the momentum normal to the surface is completely lost during the impact, whereas the tangential momentum will remain unaltered. This leads to a relation for the pressure coefficient C_P

(Anderson, 2006):

$$C_p = C_{p_{max}} \sin^2 \theta \tag{2.28}$$

In this equation, angle θ is the angle between the freestream velocity and the inclined plate, as indicated by figure 2.2. $C_{p_{max}}$ is obtained from the Rankine-Hugoniot relations (normal shock wave):

$$C_{p_{max}} = \frac{2}{\gamma M_\infty^2} \left\{ \left[\frac{(\gamma+1)^2 M_\infty^2}{4\gamma M_\infty^2 - 2(\gamma-1)} \right]^{\gamma/(\gamma-1)} \left[\frac{1-\gamma+2\gamma M_\infty^2}{\gamma+1} \right] - 1 \right\} \tag{2.29}$$

In chapter 3 the Newtonian theory will be used to compare the pressure distribution of a blunted flat plate. The pressure distribution of Hyperion-2, which will be computed with SU^2 will also be compared using this simplified theory.

2.2.2 Numerical methods

The numerical time integration method used in the trajectory optimisation software is the third order explicit Adams-Bashforth method, as will be explained first. Then, the Differential Evolution algorithm will be presented.

Adams-Bashforth method

The Adams-Bashforth method is a linear multi-step method and is based on a Taylor expansion. The term multi-step indicates that the integration is performed using information from more than one time step. This generally means that information about multiple derivatives is needed, see for example a Taylor series expansion. Computing these derivatives is proven difficult. Adams and Bashforth have derived a scheme in which information about the derivatives is not necessary. The downside is that more initial conditions are needed. These extra initial values can be obtained by using other self starting schemes such as the Euler method. Using a low order self starting scheme can reduce the order of the overall integration. A self starting scheme of the same order should be considered.

$$x_{n+2} = x_{n+1} + \frac{1}{2} h \left(3x'_{n+1} - x'_n \right) \tag{2.30}$$

$$x_{n+3} = x_{n+2} + \frac{1}{12} h \left(23x'_{n+2} - 16x'_{n+1} + 5x'_n \right) \tag{2.31}$$

Equation 2.30 and 2.31 show the results of a two and three step Adams-Bashforth scheme, respectively (Griffiths and Higham, 2010). In these equations, x' denote the initial function (differential equation). The Adams-Bashforth scheme can be expanded to higher orders to increase accuracy at the cost of stability.

Differential evolution

Differential Evolution is an evolution-based algorithm, such as a genetic algorithm. The difference between genetic evolution and differential evolution is the way the individuals are being assessed. In genetic algorithms, the assessment is based on animal behaviour or social phenomena. Differential evolution makes use of mathematical arguments, which leads to a simple and fast linear operator (Feoktistov, 2006).

The algorithm of Differential Evolution is as follows. From the initial population, three individuals are chosen. From the first two individuals, the (scaled) difference in direction and length is determined. This difference is added to the third individual, generating a possible location for a new individual, with as reference the third individual. The vector from the third individual towards the new individual is called the mutation vector and is given by equation 2.32 and illustrated in figure 2.3 (Feoktistov, 2006).

$$U = X_{r,3} + F\left(X_{r,2} - X_{r,1}\right) \tag{2.32}$$

In equation 2.32 U is the mutation vector, F is the scaling factor and $X_{r,n}$ are the randomly

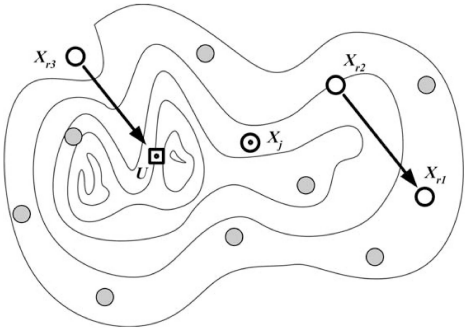

Figure 2.3: Determination of the mutation vector U (Feoktistov, 2006).

chosen individuals. The new individual is called the trial individual. Every parameter of the vector U is calculated according a probability Cr, which is freely chosen, depending on the problem. At least one of the parameters is directly inherited by the trial individual X without the probability factor. For example, when the individual has parameters angle of attack, centre of mass position and flap dimensions, one of the parameters will be directly inherited, while the other parameters are determined using a randomiser. The last thing that remains is to determine if the trial individual is better than the current individual, by comparing the fitness level. The fitness level is a value that indicates how close to th optimal value the individual is. For example, when there is a minimisation problem with a function with a minimum value (objective function) of zero, then the fitness level is the function evaluation of the current individual. The closer to zero the fitness level is, the better. If the fitness level is equal or better, the trial individual is accepted. The trial individual is then directly placed in the population. This process is repeated over the various individuals, converging towards an optimal result where the objective function is as close to zero as possible.

This optimisation algorithm is easy to program, powerful and fast. It is used in the trajectory optimisation software by Dijkstra (2012), which will be used to define an optimal trajectory for

the improved aerodynamic database of the Hyperion-2. The implementation of the differential evolution algorithm for the trajectory optimisation is as follows. Each individual has 6 fixed parameters and additional parameters depending on the number of control nodes. The control nodes are used to control the angle of attack of the vehicle, and are mapped in the mass-normalised energy domain for the controlled flight. The control solution that is defined by the control nodes is made continouos by a Hermite spline interpolation. The fixed parameters in the individuals are the z- and x-positions of the centre of mass, the cords of the two flaps and the lengths of the two flaps. In each generation, a trajectory is generated with the different individuals. In the next generation, a trial individual is constructed, and a new trajectory is created. If the objective value is increased (measurement time at constant Mach number), the new individual is accepted in the population. This process is repeated until convergence parameters are reached or a set number of generations (or iterations).

2.2.3 Flight Mechanics

This section summarises the theory of flight mechanics. First the reference frames are discussed, then the transformation matrices are explained. After that, the translational equations of motion for a non-propulsive flight with no sideslip are given.

Reference frames

This section defines the reference frames that are of interest in trajectory calculations. Multiple frames are needed to simplify the equations of motions in a certain reference frame. These reference frames can converted by using transformation matrices (Mooij, 1998).

(Pseudo) Inertial planetocentric reference frame (I) This reference frame has its origin at the centre of mass (c.o.m.) of the central body around which the vehicle is moving, for example, Earth. The Z_I-axis is pointed towards the north. The X_I-axis is directed at the vernal equinox. Usually the vernal equinox is taken at January 1, 2000 at 12:00. The Y_I-axis completes the right-hand system. For this reference frame, the $O_I X_I Z_I$-plane coincides with the equatorial plane of the body.

Rotating planetocentric reference frame (R) The rotating planetocentric reference frame coincides with the inertial planetocentric reference frame. However, the X_R-axis points to the intersection of the equator and the zero longitude line (Greenwich line). The Z_R-axis points north (collinear with Z_I) and the Y_R-axis completes the right hand system.

Body reference frame (B) This frame is fixed to the vehicle, where the origin is located at the c.o.m. of the vehicle. The X_B-axis is positive in the vehicle's forward direction and lies in the plane of symmetry. The Z_B-axis points in the vehicle's downward direction and also lies in the plane of symmetry. Again, the Y_B-axis completes the right-hand reference frame.

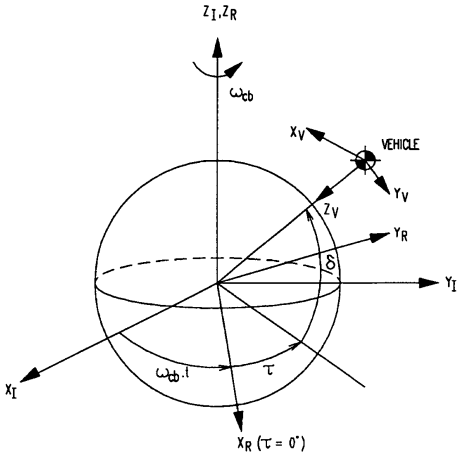

Figure 2.4: This figure displays the intertial (I), planetocentric (R) and vertical (V) reference frames (Mooij, 1994).

Vertical reference frame (V) This vehicle fixed reference frame is also located at the c.o.m. of the vehicle. The Z_V-axis points towards the central body's c.o.m. (along the radial component of the gravitational acceleration). The X_V-axis points towards the northern hemisphere of the central body and lies in a meridian plane. The Y_V-axis completes the right-hand reference frame.

The next two frames have a groundspeed based and an airspeed based variant. The difference in these frames lies in the presence of wind. When there is no wind (as is the case in this thesis), both frames coincide.

Trajectory reference frame (T) The Z_T-axis is pointed downwards in the verticle plane. The X_T-axis is defined along the velocity vector relative to the rotating planetocentric frame. Again, the Y_T-axis completes the right-handed system.

Aerodynamic reference frame (A) In this frame, the X_A-axis points in the very same direction as the X_T-axis, namely along the velocity vector. The Z_A-axis coincides with the opposite aerodynamic lift force direction. The Y_A-axis completes the right-handed system.

Transformation matrices

In the previous section, different reference frames have been defined. These reference frames can be used effectively, by easily transforming vectors from one reference frame to another. This is done by means of transformation matrices or quaternions. The transformation matrices are derived from unit axis-rotations and include the Euler angles.

For each axis and rotation angle, a transformation matrix exists. For a rotation about the

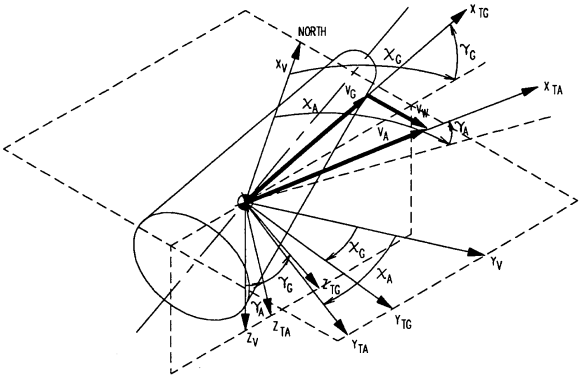

Figure 2.5: This figure displays the trajectory reference frame (T) and the vertical (V) reference frame (Mooij, 1994).

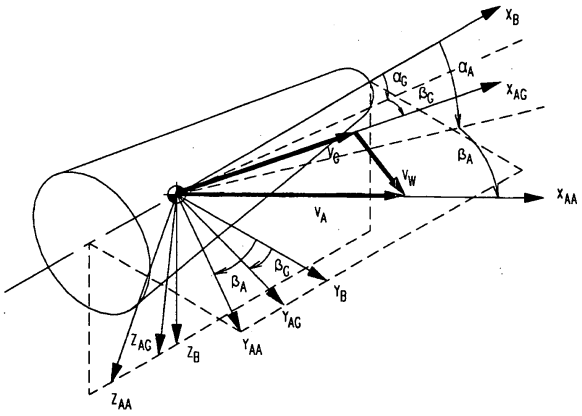

Figure 2.6: This figure displays the aerodynamic reference frame (A) and the body (B) reference frame (Mooij, 1994).

X-axis by an angle of ϕ_x, the transformation matrix yields:

$$\mathbb{T}_{BA} = \begin{bmatrix} 1 & 0 & 0 \\ 0 & \cos\phi_x & \sin\phi_x \\ 0 & -\sin\phi_x & \cos\phi_x \end{bmatrix} \tag{2.33}$$

For rotations about the Y- and Z-axis by an angle of ϕ_y and ϕ_z respectively, the matrices read:

$$\mathbb{T}_{BA} = \begin{bmatrix} \cos\phi_y & 0 & -\sin\phi_y \\ 0 & 1 & 0 \\ \sin\phi_y & 0 & \cos\phi_y \end{bmatrix} \tag{2.34}$$

$$\mathbb{T}_{BA} = \begin{bmatrix} \cos\phi_z & \sin\phi_z & 0 \\ -\sin\phi_z & \cos\phi_z & 0 \\ 0 & 0 & 1 \end{bmatrix} \tag{2.35}$$

In the aerospace field, the attitude of the vehicle (angle of attack, bank angle and sideslip angle) can be transformed to different reference frames using a rotation about the three Euler angles (ϕ_x, ϕ_y, ϕ_z). The sequence is a rotation about the Z-, Y- and X-axis respectively, hence $\phi_z \rightarrow \phi_y \rightarrow \phi_x$. This yields a complete transformation matrix from an arbitrary frame B to an arbitrary frame A:

$$\mathbb{T}_{AB} = \mathbb{T}_x \mathbb{T}_y \mathbb{T}_z \tag{2.36}$$

Translational equations of motion

Dijkstra (2012) uses a three-degrees-of-freedom flight dynamic model, thus only the translational equations of motion are considered. The velocity and position vectors are usually described in spherical coordinates. These vectors can also be expressed in Cartesian coordinates, using a certain frame of reference. The velocity vector is described by the modulus (V), the flight path angle (γ) and the heading (χ). The position vector is described using the distance (R), the latitude (δ) and the longitude (τ). These vectors are expressed with respect to the rotating planetocentric reference frame (R-frame). Figure 2.7 shows the velocity and position vectors with their corresponding parameters.

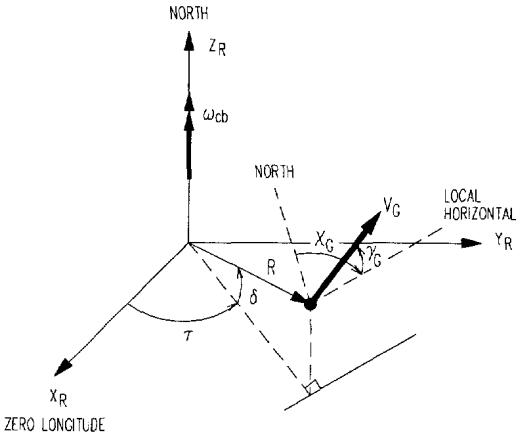

Figure 2.7: Definition of the flight parameters, the position vector and the velocity vector in the R-frame. The angles are all indicated positive (Mooij, 1998).

The equations of motion with respect to the rotating frame (R) yield:

$$\mathbf{F}_R = m\frac{d^2\mathbf{r}_{cm}}{dt^2} + 2m\boldsymbol{\omega}_R \times \mathbf{V}_R + m\boldsymbol{\omega}_R \times (\boldsymbol{\omega}_R \times \mathbf{r}_{cm}) \tag{2.37}$$

In this equation $\mathbf{F}_R$ is the summation of all external forces acting on the vehicle (propulsive, aerodynamic and gravitational), $2\boldsymbol{\omega}_R \times \mathbf{V}_R$ is the apparent Coriolis acceleration (due to the vehicle's motion in a rotating frame) and $\boldsymbol{\omega}_R$ is the rotational rate of the R-frame. This equation can be solved to yield dynamic and kinematic equations. This is a complex mathematical procedure which is elaborated in Mooij (1994). Essentially, an intermediate reference frame between the spherical coordinates and the rotating frame is defined in which the components of equation 2.37 are defined. The two systems with three equations can then be solved for the dynamic and kinematic equations (Mooij, 1994). Since sideslip and propulsion is not included, the equations yield:

$$\begin{aligned}\dot{V} = &-\frac{D}{m} - g_r \sin\gamma - g_\delta \cos\gamma \cos\chi \\ &+ \omega_R^2 R \cos\delta \left(\sin\gamma \cos\delta - \cos\gamma \sin\delta \cos\chi\right)\end{aligned} \tag{2.38a}$$

$$\begin{aligned} V\dot{\gamma} =& \frac{L}{m}\cos\sigma - g_r\cos\gamma + g_\delta\sin\gamma\cos\chi \\ &+ 2\omega_R V\cos\delta\sin\chi + \frac{V^2}{R}\cos\gamma \\ &+ \omega_R^2 R\cos\delta\left(\cos\delta\cos\gamma + \sin\gamma\sin\delta\cos\chi\right) \end{aligned} \tag{2.38b}$$

$$\begin{aligned} V\cos\gamma\dot{\chi} =& -\frac{L}{m}\sin\sigma + mg_\delta\sin\chi \\ &+ 2\omega_R V\left(\sin\delta\cos\gamma - \cos\delta\sin\gamma\cos\chi\right) \\ &+ \frac{V^2}{R}\cos^2\gamma\tan\delta\sin\chi + \omega_R^2 R\cos\delta\sin\delta\sin\chi \end{aligned} \tag{2.38c}$$

The kinematic equations that correspond to these dynamic equations are given by:

$$\dot{R} = V\sin\gamma \tag{2.39}$$

$$\dot{\tau} = \frac{V\sin\chi\cos\gamma}{R\cos\delta} \tag{2.40}$$

$$\dot{\delta} = \frac{V\cos\chi\cos\gamma}{R} \tag{2.41}$$

Note that for $\gamma = \pm 90^\circ$ (which corresponds to vertical flight) and $\delta = \pm 90^\circ$ singularities exist. These singularities are not of importance, as these flight conditions do not occur for the trajectory of Hyperion-2.

2.2.4 Environment model

The atmosphere is defined by the gravity distribution, temperature distribution and pressure distribution as function of altitude. First the gravity model is discussed, after which the atmospheric conditions follow.

Gravity model

The gravity models that are frequently used are either for a spherical planet or a non-spherical planet. The first offers the basis of all models of the second. The non-spherical gravity model is an extension to the spherical gravity model. These extensions go by the name of spherical harmonics.

Spherical Earth The Earth's gravity model is based on Newton's law of universal gravitation. Consider two point masses at a vector distance $\mathbf{r}_{12}$. There exists a gravitational force between the two point masses. If one of the masses is small compared to the other mass, it

can be neglected and only the mass of the, for example, Earth is taken into account. The gravitational acceleration yields (Tewari, 2007):

$$\mathbf{g} = -GM_e \frac{\mathbf{r}_{12}}{r_{12}^3} = -\mu \frac{\mathbf{r}_{12}}{r_{12}^3} \tag{2.42}$$

In this equation G is the universal gravitational constant which is equal to $6.67259 \times 10^{-11}\,\mathrm{m}^3/(\mathrm{kg\,s}^2)$ (Tewari, 2007).M_e is the mass of the Earth. The product of G and M_e is also the parameter μ. This equation is only valid for a spherical Earth.

Non-spherical Earth As is well known, the Earth is far from spherical. For example, due to the rotation of the Earth and the centrifugal mass distribution, the Earth tends to be flatter around the poles and larger in radius around the equator. The Earth has an oblate shape. Not only this deviation in shape is present, but many more. The shape has an influence on the gravitational acceleration field close to a planet and can be described by the mathematical model of spherical harmonics. The equations for the gravitational acceleration are given in the radial direction and the north direction (see figure 2.7) in equation 2.43 (Mooij, 1994):

$$g_r = \frac{\mu}{r^2}\left[1 - \frac{3}{2}J_2\left(\frac{R_e}{r}\right)^2\left(3\sin^2\delta - 1\right)\right] \tag{2.43a}$$

$$g_\delta = -3\frac{\mu}{r^2}\left(\frac{R_e}{r}\right)^2 \sin\delta\cos\delta J_2 \tag{2.43b}$$

In this equation, the quantity μ is the product of GM_e, R_e is the equatorial radius of the Earth and r is the distance to the centre of the vehicle. The terms J_2, J_3 and J_4 are the so-called *Jeffrey constants*. These are the constants that model the effects of, for example, the aforementioned oblation. The J_3 and J_4 constants are considerably small compared to J_2 and are often neglected while still having an accurate gravity model (Tewari, 2007).

Atmospheric model: 1976 United States Standard Atmosphere

The standard atmosphere model is defined from various measurements in the atmospher and is this an average. This has lead to a defined variation of temperature T with altitude. There are constant temperature regions in the atmosphere, which are called the isothermal regions. In addition, there are linear variations of temperature with altitude which are called the gradient regions. Through the equation of state, when temperature is a function of altitude, then so are density and pressure.

Isothermal regions In the isothermal regions, the temperature does not vary with altitude. The equation for the pressure yields:

$$\frac{p}{p_1} = e^{-\frac{g_0}{RT}(h-h_1)} \tag{2.44}$$

The density can be computed with the equation of state, completing the state variable equations for the isothermal region

Gradient regions In these regions, the temperature varies linearly with altitude, hence the temperature gradient (lapse rate) is given by:

$$a \equiv \frac{\mathrm{d}T}{\mathrm{d}h} = \frac{T - T_1}{h - h_1} \tag{2.45}$$

The temperature is not fixed, thus a different pressure equation holds for the gradient regions:

$$\frac{p}{p_1} = \left(\frac{T}{T_1}\right)^{-\frac{g_0}{aR}} \tag{2.46}$$

Again, through the equation of state the density can be obtained. The variation of the temperature with altitude is linear, as previously mentioned. The equation for the temperature yields:

$$T = T_1 + a\,(h - h_1) \tag{2.47}$$

Note that the variables with subscript '1' in each of these equations correspond to the values at the base of the isothermal or gradient region. A temperature profile as a function of height is given in figure 2.8 (based on the values in Tewari (2007)).

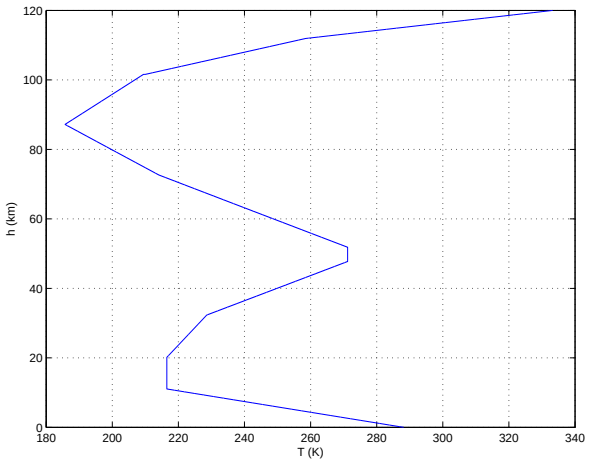

Figure 2.8: Temperature profile as function of height.

The temperature gradients (or lapse rates) are determined experimentally. Various standard atmosphere models are available. Below an altitude of 86 km, the 1976 U.S. Standard Atmosphere can be used. In this region, the hydrostatic equilibrium is considered a valid assumption. Above 86 km the temperature varies non-linearly in this model. The 1962 U.S. Standard Atmosphere can be used as extension for altitudes up to 2000 km. This model also employs a linear temperature variation in the gradient regions.

Chapter 3

Validation and verification of the CFD software

According to the Oxford Dictionary (Stevenson, 2010), the definition of validation is 'to demonstrate the truth or value'. This aspect is particularly important when using a software package that needs to simulate real flow. Before the software is used, it is validated and verified first to gain trust and confidence in the software and the results. This chapter is devoted to the validation of Stanford University Unstructured (SU^2), the computational fluid dynamics (CFD) software used in this thesis. This verification and validation is performed using simple shapes, as ample reference data is available in literature, the problems are easy to model and the to be verified parameters are present without interaction of phenomena that might be present in complex geometries. First, the settings and conditions regarding the validation and verification are discussed. Then, the shape of the shock wave and the shock stand-off distance of a flat plate with a blunt leading edge is verified with theory and validated with experimental data in section 3.2. The pressure distribution of a flat plate with a spherical nose is considered in section 3.3. Section 3.4 will verify and validate the heat flux of a sphere. Finally, section 3.5 will summarise the conclusions drawn in this chapter.

3.1 Settings and conditions

The verification and validation geometries used are the blunted flat plate and the circular cylinder. For these two geometries, there is ample comparison data, either numerical, experimental or theoretical. The blunted flat plate and the circular cylinder are easy to model, easy to mesh and the computational time is low. Using these standardised test geometries, the software can be validated and verified for different hypersonic characteristics, such as shock standoff distance, shock shape, pressure distribution and heat flux. Since the aerodynamic coefficients (thus pressure distribution) and heat fluxes are of interest in this thesis, it is important that these quantities are validated and verified for simple shapes. If the simple

shapes show an accuracy within 10% with measurements, the software performs well.

The solver definition will be the same for all test cases. The physical flow definition, geometry and mesh will be different, depending on the validation data. For all test cases, the following solver settings are used:

- Numerical scheme: Jameson-Schmidt-Turkel (JST) second order centered scheme. This scheme uses artificial dissipation for stability. The Venkatakrishnan's limiter is used and set to 0.012. This scheme has been chosen as the available upwind scheme only produces results when a first order scheme is used. The second order upwind scheme (MUSCL approach) does not work. A second order central scheme provides more accurate results than a first order upwind scheme,
- Integration scheme: Euler implicit with CFL number of 5. These settings have been chosen since the solution converges quickly with high accuracy,
- Convergence criteria: A minimum value of the residual (density) is set to -10 (log) and the residual reduction to 6. These limits are quite high, but it ensures proper convergence for both test cases,
- Physical model: Navier-Stokes equations. The terms included in these equations are elaborated in section 2.1.
- Laminar flow. Turbulence models have not been included in this verification and validation as the Reynolds numbers considered are relatively low.

The geometrical parameters of each test case is summarised in table 3.1. The mesh of the blunted flat plate is given in figure 3.1. The flat plate itself is given an isothermal wall boundary marker, where the temperature of the wall is kept constant. No use of inflow or outflow conditions are given, rather a farfield boundary marker is used. The symmetry boundary marker is used to indicate the symmetry plane. The flowfield consist of a unstructered mesh, using triangular shapes. The boundary layer has a structured rectangular mesh, stretched in flow direction, using a progression of 1.25. This gives a fine mesh distribution at the wall, increasing mesh size towards the edge of the boundary layer. The circular cylinder has a similar grid as the blunted flat plate. However, here is no symmetry plane and the geometry is taken as a half circle. The boundary layer is structured and the flow field is unstructured. The geometry of the circular cylinder is displayed in figure 3.2.

The freestream conditions and wall temperature for each test case are given in table 3.2. The parameters are identical to the experimental data. Test case 1 uses experimental data from Lees and Kubota (1957). Test case 3 is compared to Lukasiewicz (1962). Test case 4 is validated with data from Kubota (1957). The heat flux data (test cases 5 to 8) are obtained from Koppenwallner (1984).

Table 3.1: Geometry and mesh definition for all validation and verification cases. The abbrevation BFP stands for blunted flat plate and CC for circular cylinder. The last column shows the boundary layer thickness as specified in the mesh (structured grid).

No	Geometry	Validation	Radius [m]	# Cells	Max y^+	Mesh BL [m]
1	BFP	Shock shape	0.5	672,208	6.26	0.1
2	BFP	Stand-off distance	0.5	672,208	6.26	0.1
3	BFP	Plate pressure	0.5	672,208	6.26	0.1
4	BFP	Nose pressure	0.5	672,208	6.29	0.1
5	CC	Heat flux	0.0102	95,254	1.19	0.008
6	CC	Heat flux	0.0102	95,254	0.97	0.008
7	CC	Heat flux	0.0062	33,211	0.68	0.008
8	CC	Heat flux	0.0062	33,211	0.61	0.008
9	BFP	Heat flux	0.5	101,592	5.16	0.05
10	BFP	Heat flux	0.5	105,224	2.1	0.05
11	BFP	Heat flux	0.5	106,586	1.31	0.05
12	BFP	Heat flux	0.5	111,126	0.17	0.05
13	BFP	Heat flux	0.5	101,592	1.56	0.05
14	BFP	Heat flux	0.5	105,224	0.27	0.05
15	BFP	Heat flux	0.5	106,586	0.14	0.05
16	BFP	Heat flux	0.5	111,126	0.01	0.05

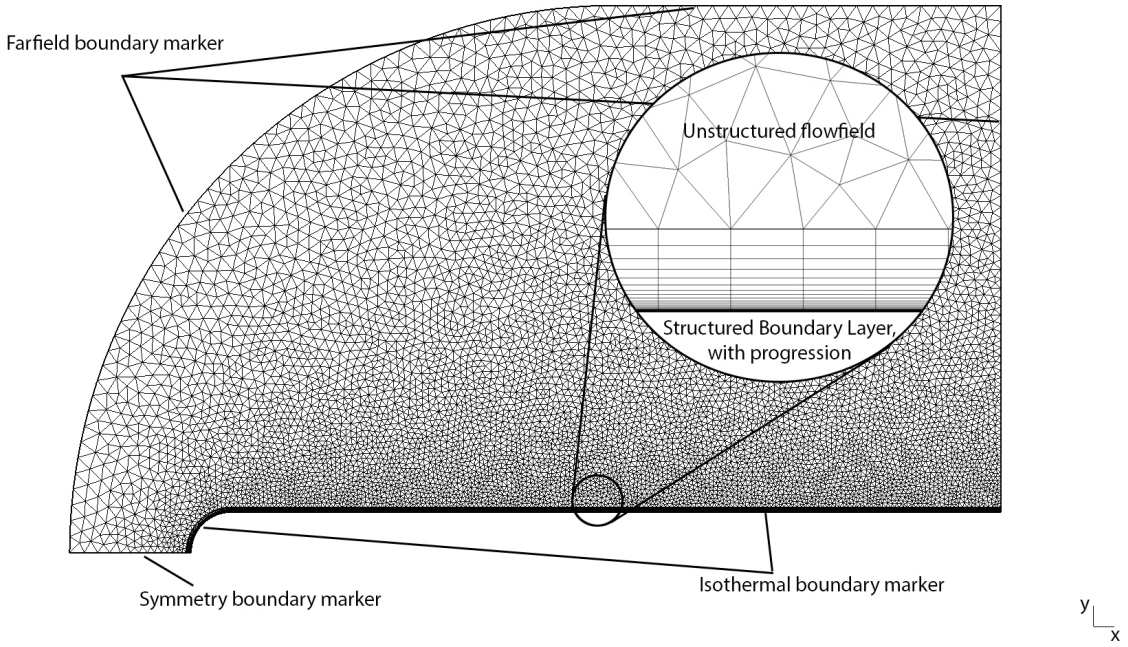

Figure 3.1: Flat plate geometrical model and mesh.

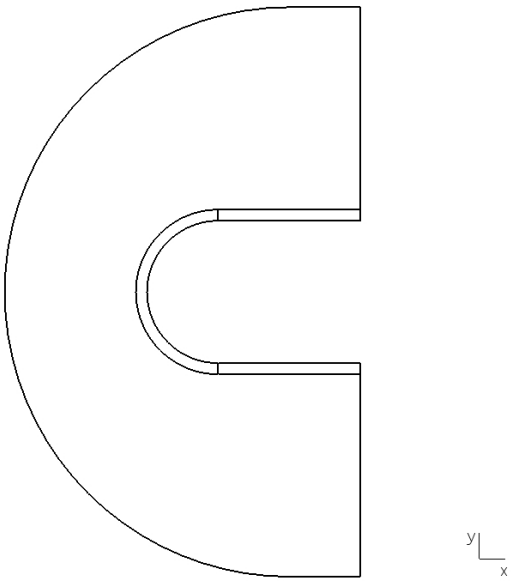

Figure 3.2: Circular cylinder geometrical model.

Table 3.2: Physical flow conditions for all test cases. The freestream parameters and wall temperature are based on the reference data of the test case.

No	M_∞	p_∞ [N/m^2]	ρ_∞ [kg/m^3]	T_∞ [K]	Re [1/m]	T_{wall} [K]
1	8.08	85.89	0.001	273.15	1.7×10^5	300
2	8.08	85.89	0.001	273.15	1.7×10^5	300
3	8.08	85.89	0.001	273.15	1.7×10^5	300
4	7.7	91.72	0.001	273.15	1.73×10^5	300
5	23.8	0.016	2.07×10^{-7}	273.15	94.8	300
6	21.5	0.011	1.45×10^{-7}	273.15	60.0	300
7	20.6	0.006	7.11×10^{-8}	273.15	28.2	300
8	18.9	0.005	6.15×10^{-8}	273.15	22.4	300
9	10	89.41	0.001	271.2	2.2×10^5	300
10	10	89.41	0.001	271.2	2.2×10^5	300
11	10	89.41	0.001	271.2	2.2×10^5	300
12	10	89.41	0.001	271.2	2.2×10^5	300
13	10	89.41	0.001	271.2	2.2×10^5	3000
14	10	89.41	0.001	271.2	2.2×10^5	3000
15	10	89.41	0.001	271.2	2.2×10^5	3000
16	10	89.41	0.001	271.2	2.2×10^5	3000

3.2 Shock characteristics

The position and shape of a shock are dependent on the Mach number. A shock wave influences the flow behind the shock. It is therefore important that the position of the shock and the shape of the shock are properly computed. Using experimental data and empirical relations, the shock shape and the shock stand-off distance (distance between body and shock) are validated.

Shock shape

The shape of the shock can be estimated by the blast-wave theory. The work of Lukasiewicz provides the following correlated relations for the shock shape of a blunt-nosed flat plate (Lukasiewicz, 1962):

$$\text{First approximation: } \frac{r}{d} = 0.774 C_D^{1/3} \left(\frac{x}{d}\right)^{2/3} \tag{3.1}$$

$$\text{Second approximation: } \frac{r}{d} = \frac{0.774 M_\infty^2 C_D}{M_\infty^2 \left[C_D/\left(x/d\right)\right]^{2/3} - 1.09} \tag{3.2}$$

In these equations, r depicts the y-position of the shock and d is the diameter of the blunt nose. The value of the drag coefficient C_D is 1.24, which is obtained by SU^2. In the second approximation, the freestream pressure ahead of the blast wave is taken into account, whereas this is not the case in the first approximation. Figure 3.3 shows the Mach contour of a blunt-nosed flat plate. As can be seen in the figure, both approximations are below the computed shock shape. It has been shown that the approximated shock shape is lower than the exact shock location (method of characteristics) (Lukasiewicz, 1962). The origin of the two approximations must be shifted to fit the measurement data. In blast-wave theory, an instantaneous release of energy at a point or line in space is assumed (Anderson, 2006), which is not the case in true hypersonic flow. The measurements of Lees and Kubota (1957) show a good agreement with the SU^2 shock shape. The average error is 3% and the maximum error is 11%. An outlier in the measurement data causes this larger error. It can be concluded that the shock shape is computed correctly, within 10% of the measurement data.

Shock stand-off distance

The shock stand-off distance is the distance between the blunt body and the shock wave. It is often denoted by either δ or Δ. Billig (1967) has correlated wind tunnel data to obtain an empirical relation for the shock shape and shock stand-off distance as a function of Mach number. For a sphere-cone and a cylinder-wedge configuration, Billig obtained equations 3.3 and 3.4. These relations are based on a hyperbolic shock shape and are correlated using windtunnel experiments (Billig, 1967).

$$\text{Sphere-cone: } \frac{\delta}{R} = 0.143 \ \exp\left[3.24/M_\infty^2\right] \tag{3.3}$$

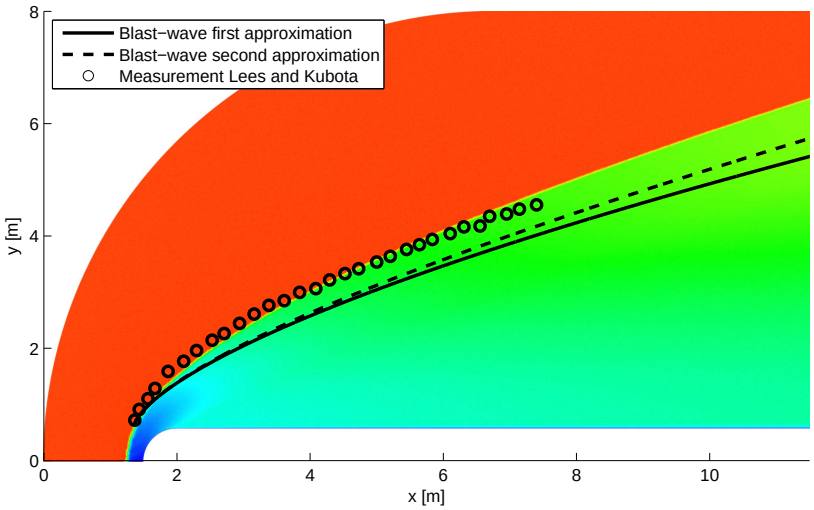

Figure 3.3: Shock shape comparison using blast-wave theory. The body is a flat plate with a blunted leading edge. The contour is the Mach number for $M_\infty = 8.08$.

$$\text{Cylinder-wedge: } \frac{\delta}{R} = 0.386 \ \exp\left[4.67/M_\infty^2\right] \tag{3.4}$$

The geometry is a cylinder-wedge configuration with a wedge angle of 0°. For three Mach numbers (6, 8.08 and 10), the shock stand-off distance is investigated. The calculated stand-off distance show a 2% error with respect to equation 3.4 by Billig (1967). Figure 3.4 shows the curve of equation 3.4 and the values from SU^2. The numerical values are summarised in table 3.3.

Table 3.3: Non-dimensional shock stand-off distance computed by SU^2 and the correlations of Billig (1967).

Mach	SU^2	Billig (eq. 3.4)
6	0.4390	0.4395
8.08	0.4140	0.4146
10	0.4040	0.4045

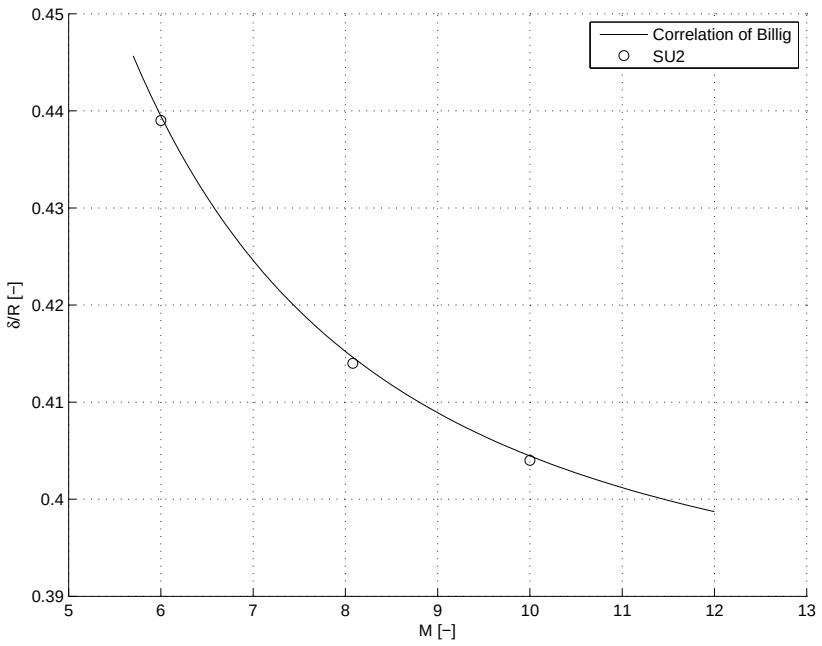

Figure 3.4: Shock stand-off distance using empirical relations (equation 3.4) by Billig (1967).

3.3 Pressure distribution

For the validation of the pressure distribution, the blunt-nosed flat plate is used. First, the pressure distribution in the nose region is compared to the modified Newtonian theory. Then, the pressure distribution is compared to windtunnel data from Lukasiewicz (1962) and grid convergence of the SU^2 computation will be studied. Windtunnel data from Kubota (1957) is used to compare experimental data with SU^2 in the nose region of the flat plate.

Modified Newtonian theory

The modified Newtonian theory gives relations for the pressure coefficient as function of freestream Mach number, local flow inclination and specific heat ratio γ. These relations are elaborated in chapter 2, but will be displayed again for convenience:

$$C_P = C_{P_{max}} \sin^2 \theta \tag{3.5}$$

$$C_{P_{max}} = \frac{2}{\gamma M_\infty^2} \left\{ \left[\frac{(\gamma+1)^2 M_\infty^2}{4\gamma M_\infty^2 - 2(\gamma-1)} \right]^{\gamma/(\gamma-1)} \left[\frac{1-\gamma+2\gamma M_\infty^2}{\gamma+1} \right] - 1 \right\} \tag{3.6}$$

Figure 3.5 shows the graph in which the modified Newtonian theory result and the result

obtained from a Navier-Stokes computation in SU^2 is plotted. As can be seen in the figure, the maximum pressure computed in SU^2 is slightly lower than the maximum pressure according to Newtonian theory. For Newtonian theory, the maximum pressure coefficient is 1.8276 and for SU^2 1.7122, which is a 6.3% difference. This difference is caused by the shape of the shock at the stangnation point. The shock at the stagnation point can be assumed a normal shock wave. However, due to the use of the symmetry plane and the use of unstructured grid elements in the farfield, the shock at that location is at an angle, hence the pressure is different after the shock. The pressure distribution on the circular nose correspond well, within a 10% difference. The Newtonian pressure reaches zero at $\theta = 90°$, which corresponds to equation 3.5. The Navier-Stokes solution shows that pressure is exerted on the flat plate downstream of the nose, which is also present in real flow.

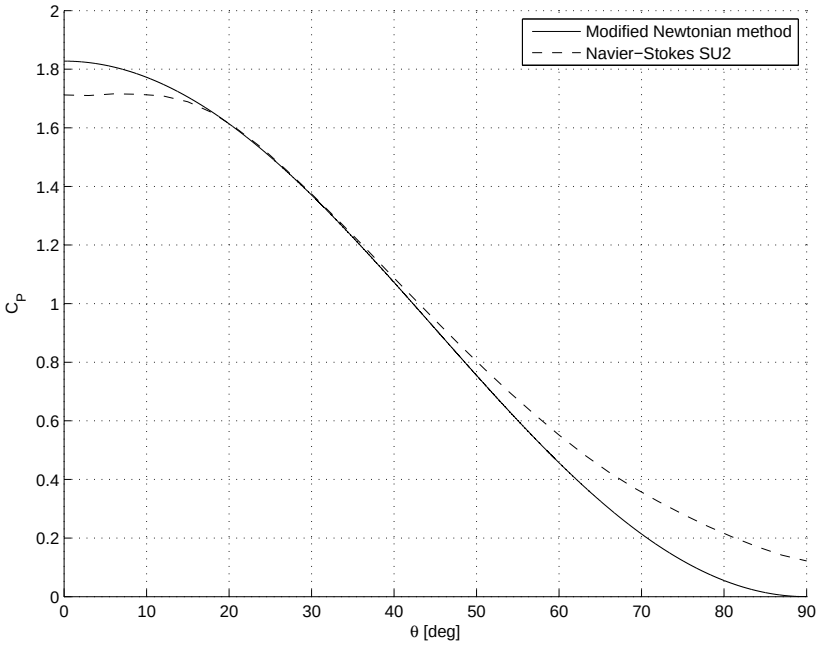

Figure 3.5: Comparison between modified Newtonian pressure and calculated pressure from a Navier-Stokes SU^2 computation.

Grid convergence for the pressure

To show that the pressure data is independent of grid size, a grid convergence study has been performed. The mesh is being refined and the flow is computed for every mesh size. When the pressures do not change with grid size, the grid has converged and grid effects do not influence the solution. For this comparison grids of 6363 (low density), 18,265 (medium density), 179,958 (high density) and 672,208 (very high density) elements are compared with experimental data by Lukasiewicz (1962).

Figure 3.6 shows that the results from SU^2 are nearly independent of grid size already at the lowest density. When the shock is captured correctly, the pressure will not vary a lot with

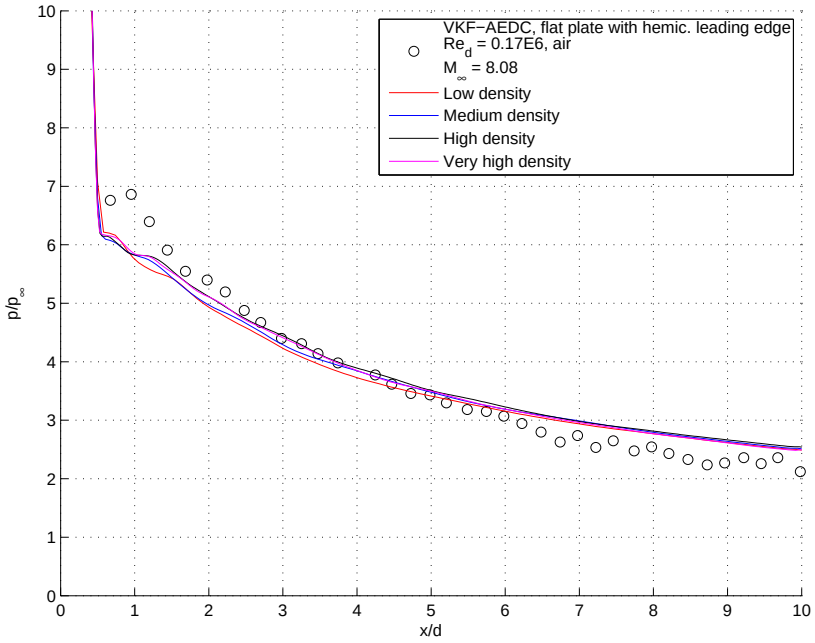

Figure 3.6: Grid convergence with Navier-Stokes SU^2 computations and comparison with experimental data from Lukasiewicz (1962).

grid size. The shock itself will be thicker as the discontinuity is smoothened over a larger area, which is shown in figure 3.7. The limits of a flow variable, i.e. the pressure before and after the shock, will remain the same. Since the pressure behind the shock does not vary with grid size, nor will the pressure distribution over the model.

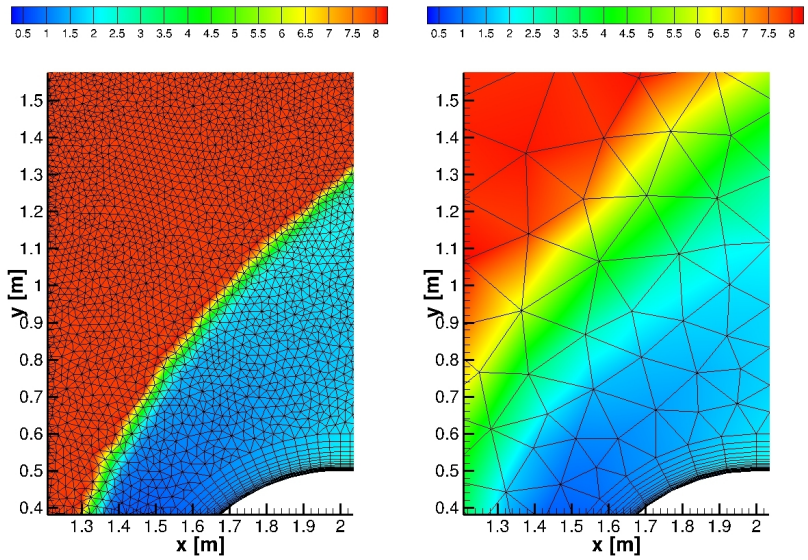

Figure 3.7: Effect of a larger cell size on the shock thickness. On the left, a fine grid where the shock is thin. On the right, a coarse grid where the shock is thick. Equal x and y positions are taken for both images.

Windtunnel data for the pressure

Using the windtunnel data from Lukasiewicz (1962), the pressure distribution can be compared with the output of SU^2. Figure 3.8 shows the measurement data and the SU^2 Navier-Stokes solution. The conditions are the same as for the Newtonian approach. As can be seen, the trend of the graph is followed accurately. The differences are less than 10 %.

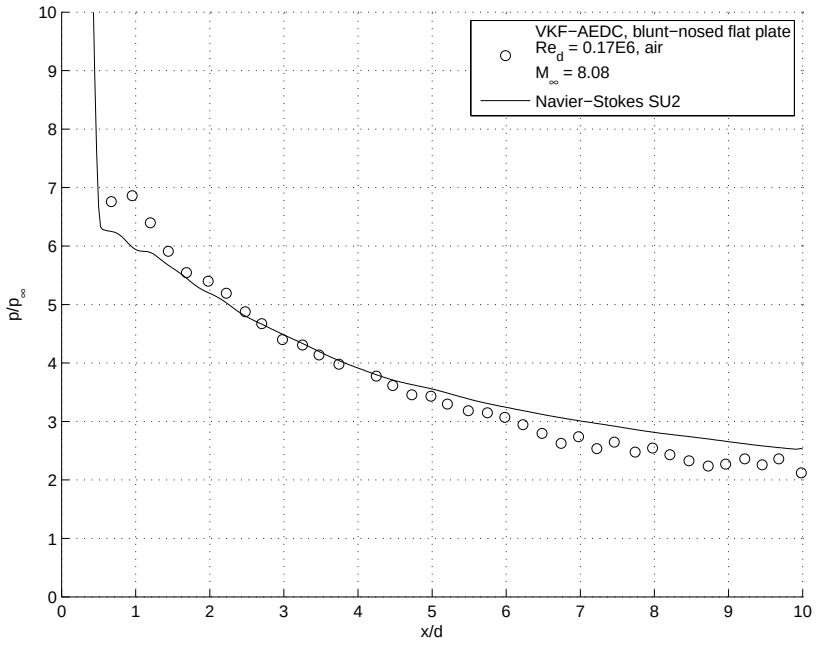

Figure 3.8: Comparison between experimental data from Lukasiewicz (1962) and calculated pressure from a Navier-Stokes SU^2 computation.

The data from Lukasiewicz (1962) lack data points on the blunted nose section of the flat plate. Kubota (1957) has performed measurements on a hemisphere cylinder slab at $M = 7.7$ and $Re = 1.73 \times 10^5$. Figure 3.9 shows the data of Kubota (1957), the SU^2 result and the modified Newtonian result. Note that the x-axis shows the s direction normalised with the diameter. The s direction is along the surface of the plate. The errors are in the order of 5%, thus the pressure distribution on the blunted nose section can be considered validated.

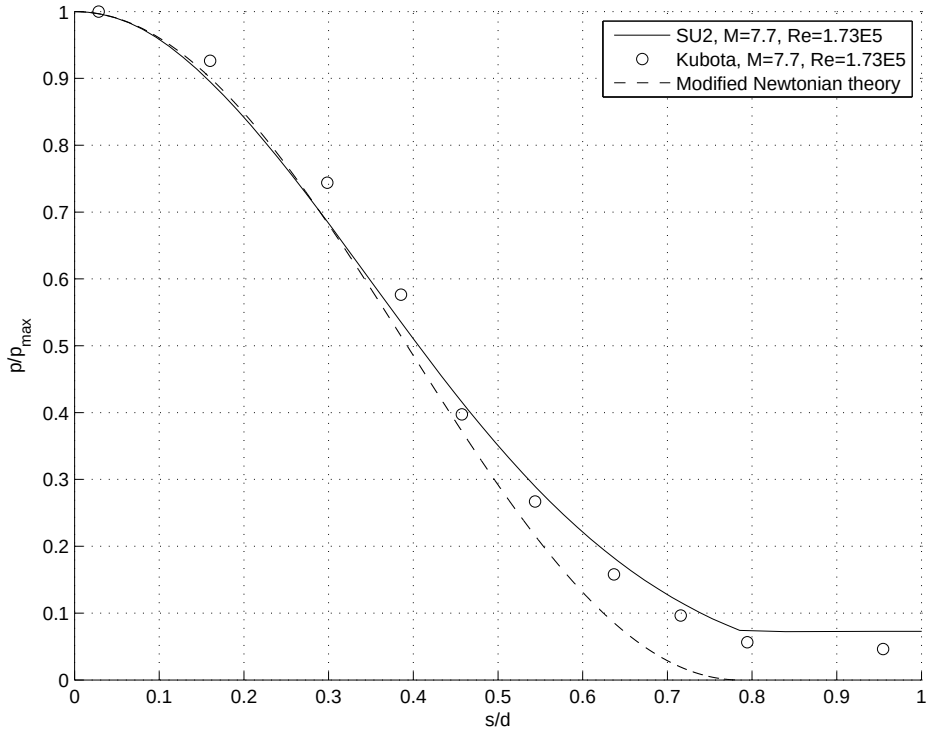

Figure 3.9: Comparison between experimental data from Kubota (1957), calculated pressure from a Navier-Stokes SU^2 computation and modified Newtonian theory.

3.4 Heat flux

One of the important quantities in hypersonic flow is the heat flux, mainly for the design of a thermal protection system of a vehicle. The heat flux indicates how much energy is exchanged between the flow and the vehicle. In order for a CFD computation to be usae in the design process of hypersonic vehicles, it is of paramount importance that the heat flux is predicted correctly. To validate this, the heat flux around a sphere is compared with measurement data. Furthermore, the Fay-Riddell equation for the stagnation point heat flux will be used to verify the heat flux computation.

Windtunnel data for the heat flux

Koppenwallner (1984) has performed experiments in which the heat transfer around a circular cylinder for a laminar flow is measured. The results were presented as the ratio between the heat flux to the stagnation point heat transfer. Various Mach numbers, Reynolds numbers and cylinder diameters are considered. The wall temperature was set to 300 K and the total temperature was 1500 K. Using the same flow conditions and geometrical model in SU^2, the results in figure 3.10 are obtained.

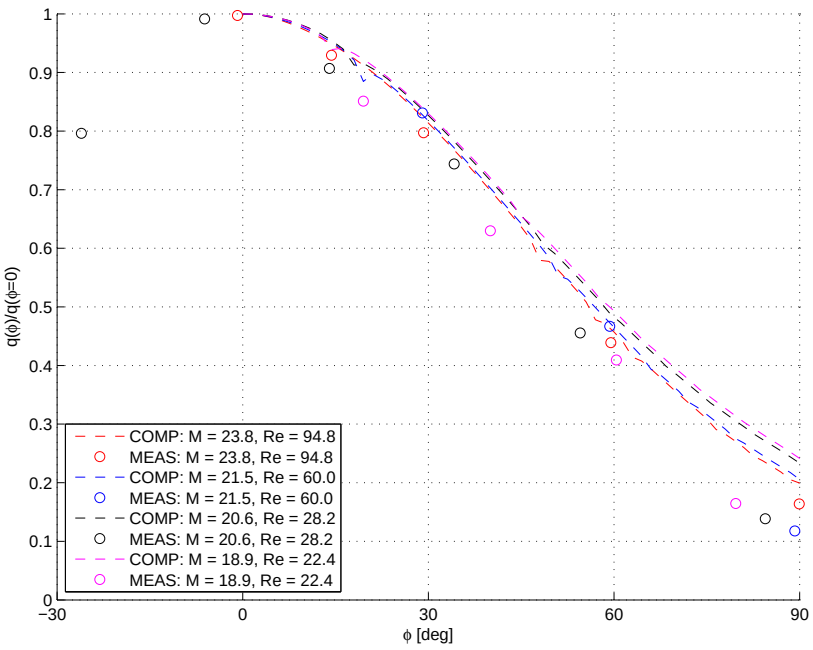

Figure 3.10: Heat transfer around a circular cylinder for a laminar flow, comparing SU^2 with Koppenwallner (1984).

As can be seen, the normalised heat fluxes from SU^2 show good agreement with the measurements for Mach numbers 23.8 and 21.5. The results for Mach numbers 20.6 and 18.9 tend to deviate from the measurements, showing a higher normalised heat flux. The model diameter is smaller in these cases. With these flow conditions, to keep an overall y^+ value of 1, a relatively large first cell height has been used. The difference between the measurement and computation is caused by insufficient boundary layer resolution. However, the results are within a 10% error margin. The normalised heat fluxes from SU^2 show outliers that are different from the trend of the line, that cause a local decrease in normalised heat flux. In figure 3.10, this effect is visible at, for example, $\phi \approx 20°$ and $\phi \approx 45°$. At these locations the density and energy residual are higher with respect to the average residuals on the wall, which is the cause of the offsets. This may be caused by insufficient boundary layer resolution. The solver cannot compute the solution correctly due to the height of the first cell. If the boundary layer resolution is increased (lower first cell height), these effects do not occur.

Heat flux computation by theory and SU^2

To validate the heat fluxes more thoroughly, the actual heat fluxes are compared with the Fay-Riddell equation. This equation is an empirical relation for the heat flux in the stagnation point of a body (i.e., where the air comes to a standstill). This equation is elaborated upton in chapter 2. For validation purposes, the Fay-Riddell equation for a frozen boundary layer with a noncatalytic wall (surface material has no effect on chemical reactions) is used (Fay

and Riddell, 1958):

$$q_w = 0.76Pr^{-0.6} \left(\rho_e \mu_e\right)^{0.4} \left(\rho_w \mu_w\right)^{0.1} \sqrt{\left(\frac{\mathrm{d}u_e}{\mathrm{d}x}\right)_s} \left(h_{aw} - h_w\right) \tag{3.7}$$

where

$$\left(\frac{\mathrm{d}u_e}{\mathrm{d}x}\right)_s = \frac{1}{R}\sqrt{\frac{2\left(p_e - p_\infty\right)}{\rho_e}} \tag{3.8}$$

and subscript e indicates edge of boundary layer conditions, subscript w indicates wall conditions, h_{0_e} is the total enthalpy and $(\mathrm{d}u_e/\mathrm{d}x)_s$ is based on Newtonian theory. A calorically perfect gas model is used, thus the enthalpy can be computed by using $h = c_p T$. For the computation of the temperatures and densities the normal shock relations are used (Anderson (2006)), since the portion of the bow shock at the stagnation point is a normal shock. The wall temperature T_w is set to 300 K. In SU^2 this is done by setting the isothermal wall boundary condition with the prescribed 300 K wall temperature on the body.

In general, the isothermal wall boundary conditions can be imposed by either setting the temperature at the wall to the prescribed temperature (300 K), or by setting the appropriate temperature gradient that is needed to achieve this wall temperature. The first option is a Dirichlet boundary condition (or strong boundary condition). The second option is a Neumann boundary condition (or weak boundary condition). The Neumann boundary condition is used in SU^2 since the solver architecture uses conservative variables (continuity, momentum and energy) in the actual flow solver, whereas the primitive variables (temperature, velocity and pressure) are only calculated in the preprocessing phase. The temperature gradient appears in the energy conservation equation. The equations for the weak isothermal boundary condition are found in the SU^2 source code:

$$\frac{\partial T}{\partial \eta} = \frac{T_{w+1} - T_w}{d_{ij}} \tag{3.9}$$

$$k = \frac{\mu c_P}{Pr} \tag{3.10}$$

$$q_w = -k\frac{\partial T}{\partial \eta} \tag{3.11}$$

In equation 3.9, $\partial T/\partial \eta$ is the temperature gradient normal to the wall, T_{w+1} is the temperature one cell above the wall, T_w is the to be imposed wall temperature, d_{ij} is the distance between the two nodes (i.e. the first cell height). Equation 3.10 shows the thermal conductivity constant k, μ the viscosity, c_P the specific heat capacity at constant pressure and Pr is the Prandtl number. Equation 3.11 is the actual weak boundary condition for the heat

flux q_w, thus temperature gradient. The weak boundary condition is used in the solver in the energy residual. A heat flux is computed, attempting to approximate the imposed wall temperature.

Grid convergence for the heat flux

When using SU^2, it was found that the computed heat flux values were very far off the values predicted by Fay and Riddell and wind tunnel measurements. It was found that this was caused by an error in the implementation of the heat flux computation. A bug fix was submitted and the error was corrected. However, the heat flux values still did not properly match the expected values. Therefore, a grid convergence study has been performed to assess the sensitivity of the convective heat flux to the mesh size near the wall. In this study, the boundary layer grid has been refined multiple times to see the effect on the heat flux. The geometry, mesh and flow definition of test cases 9 to 16 are used (see tables 3.1 and 3.2). It must be noted that when a higher wall temperature is used, the boundary layer thickness is increased. However, the local boundary layer thickness is considerably larger than the first cell height, even in the most coarse grid. The ratio between the first cell height and the boundary layer thickness is 0.04 for the wall temperature of 300 K and the coarse grid.

The results of test cases 9 to 12 ($T_w = 300\,\mathrm{K}$) are displayed in figure 3.11. The results of test cases 13 to 16 ($T_w = 3000\,\mathrm{K}$) are displayed in figure 3.12.

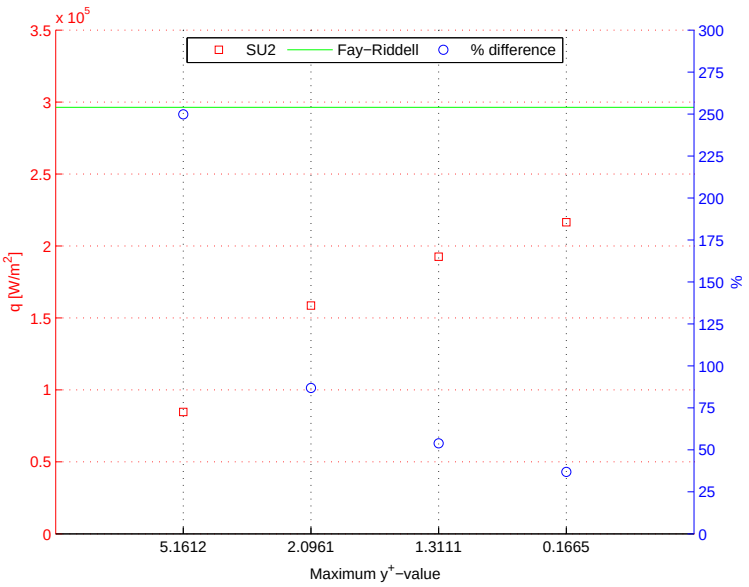

Figure 3.11: Blunted flat plate grid convergence with $T_w = 300\,\mathrm{K}$, comparing SU^2 with Fay and Riddell (1958).

Figure 3.11 shows the Fay-Riddell solution in green, which was calculated to be $2.96 \times 10^5\,\mathrm{W/m^2}$. The red squares show the result per grid density using SU^2. The blue circles show the percentage difference. The horizontal axis shows the maximum y^+-value.

For turbulent flows, this is a particular relevant quantity, whereas for laminar flow, it is a measure of the first cell height on the surface. As can be seen, the stagnation point heat flux converges properly towards the Fay-Riddell solution, for very low numbers of y^+ (i.e., the first cell height is reduced when the y^+ value is reduced).

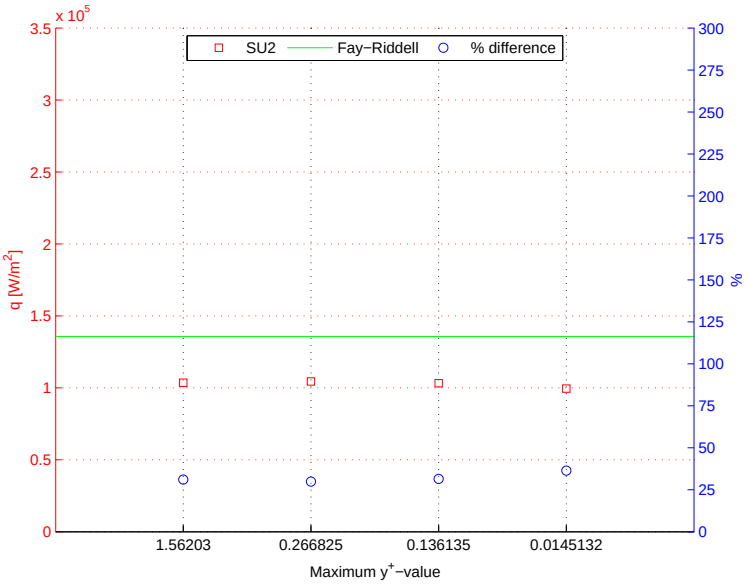

Figure 3.12: Blunted flat plate grid convergence with $T_w = 3000\,\mathrm{K}$, comparing SU^2 with Fay and Riddell (1958).

Figure 3.12 shows the Fay-Riddell solution ($q_w = 1.3564 \times 10^5\,\mathrm{W/m^2}$), SU^2 values and percentage difference in the same way as figure 3.11, but for a wall temperature of 3000 K. Note that the y^+-values are lower than for 300 K. The y^+ value is a function of viscosity, which is function of temperature, hence when the temperature changes, the y^+ value changes. However, the absolute first cell height is still equal in each corresponding case. In this test, the heat flux does not tend to converge towards the Fay-Riddell solution, with low y^+-values. The difference between these cases can be visualised by extracting the temperature profile in the stagnation point. For each case, this is displayed in figure 3.13.

Figure 3.13 shows the temperature profiles of the two different wall temperatures ($T_w = 300\,\mathrm{K}$ and $T_w = 3000\,\mathrm{K}$) and different grid densities. The temperature profiles are taken at the stagnation point, in the direction normal to the surface (η-ordinate). It can be seen that the temperature profiles are different between the test cases. For an imposed wall temperature of 300 K, coarse grid does not result in a wall temperature of 300 K, rather a wall temperature of 667 K. The denser the grid becomes, the better the wall temperature approaches 300 K. On the right side of the image, it can be seen that the wall temperatures are all nearly 3000 K, with a deviation of 3 K. This is a smaller deviation in absolute and relative sense compared to the wall temperature of 300 K.

The temperature of the flow just outside the boundary layer is close to the adiabatic wall temperature (temperature for which the wall has no heat exchange with the flow, i.e. $q_w =$

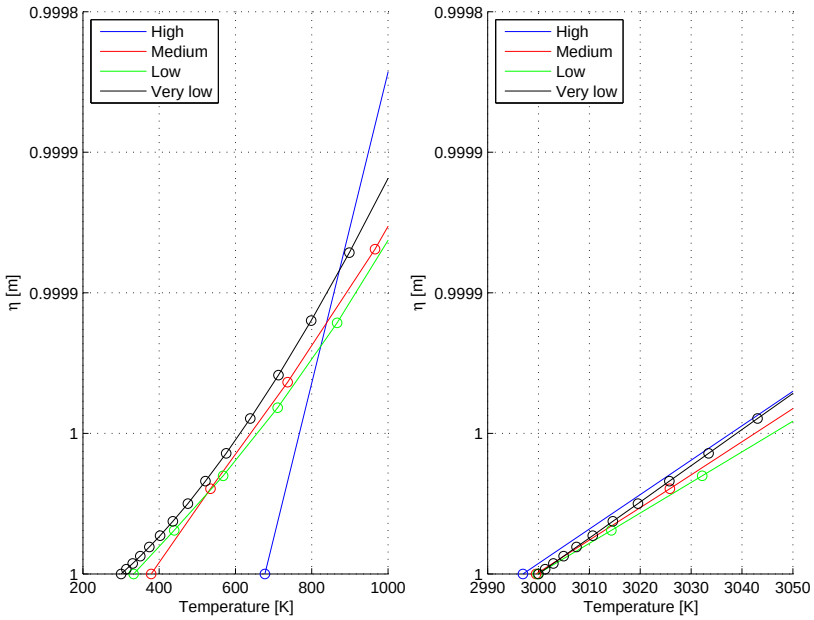

Figure 3.13: Temperature profiles for $T_w = 300\,\mathrm{K}$ and $T_w = 3000\,\mathrm{K}$ in the stagnation point of a blunted flat plate.

0). For the previous test cases (cases 9 to 16), this temperature is 5500 K. For a higher temperature wall, the temperature gradient from the wall is significantly lower than for a lower temperature wall, resulting in a wall boundary condition that is less strongly active. There is a smaller correction in temperature needed to obtain a higher wall temperature, than a lower wall temperature. In addition, the ratio between the first cell height and boundary layer thickness is smaller, as the boundary layer thickness is larger.

To summarise, it is accepted that the actual heat fluxes are not correct due to this way of imposing boundary conditions. Changing this in the source code would mean changing the complete architecture of the solver, which is time consuming, cumbersome and out of the scope of this thesis.

3.5 Validation and verification summary

To conclude the chapter on validation, the most interesting conclusions that can be drawn are summarised here.

In hypersonic flow, the shape and position of the shock is an important feature, which influence for example the heat transfer to the surface and possible chemical reactions. It has been found that SU^2 produces accurate results for these two elements. The shape and position correspond well to theory and measurement data.

The pressure computed by a full Navier-Stokes SU^2 computation correspond with theory and

experimental data. The pressure corresponds very well with the modified Newtonian theory. The measurement data from Lukasiewicz (1962) shows that SU^2 computes the pressure correctly. Furthermore it was shown that this validation is independent of grid size, using a grid convergence study.

The normalised heat fluxes show good agreement with experimental data from Koppenwallner (1984). However, when looking at the absolute values, comparing with Fay and Riddell (1958), SU^2 shows different values for the heat flux. In the grid convergence study for the heat flux it was found that the way the isothermal wall boundary condition has been implemented in SU^2 greatly influences the heat flux computation. The Neumann boundary condition should be changed to a Dirichlet boundary condition, though the architecture of the solver does not allow for this conversion in a straightforward way. The heat flux computed by SU^2 cannot (yet) be trusted.

Chapter 4

Results and comparison

The results of the CFD simulation software and the trajectory optimisation software are presented here. First, in section 4.1 the settings and parameters to run SU^2 and the trajectory optimisation software by Dijkstra (2012) are defined. Sections 4.2 and 4.3 discusses the CFD results and compares the results from SU^2 with the modified Newtonian database. In sections 4.4 and 4.5, the trajectory optimisation of both databases are shown and compared.

4.1 Experimental setup

The settings used in the CFD simulation and trajectory optimisation are given here. First, Hyperion-2 geometry, mesh layout and solver settings are discussed. Then, the search space, constraints and random seed are defined.

4.1.1 Aerodynamic database generation

The model of Hyperion-2 is based on concept 5 derived in the work of Mooij et al. (1999) (see figure 4.1). The geometry is analytically specified and presented by Mooij (2005). The values of the parameters are given in table 4.1. For the aerodynamic database generation using SU^2, the upper and lower flaps are not taken into account.

The grid of the Hyperion-2 model is displayed in figure 4.2. The grid consists of the body geometry and two shells that represent the farfield and a mesh refinement plane. A half body is used with a symmetry boundary condition to reduce the number of cells and computation time. The outer shell depicts the farfield boundary marker (excluding symmetry plane). The average mesh size in this area is 0.2 m. The inner shell is created to refine the mesh elements around the body. This ensures that the shock-wave is captured properly. The average mesh

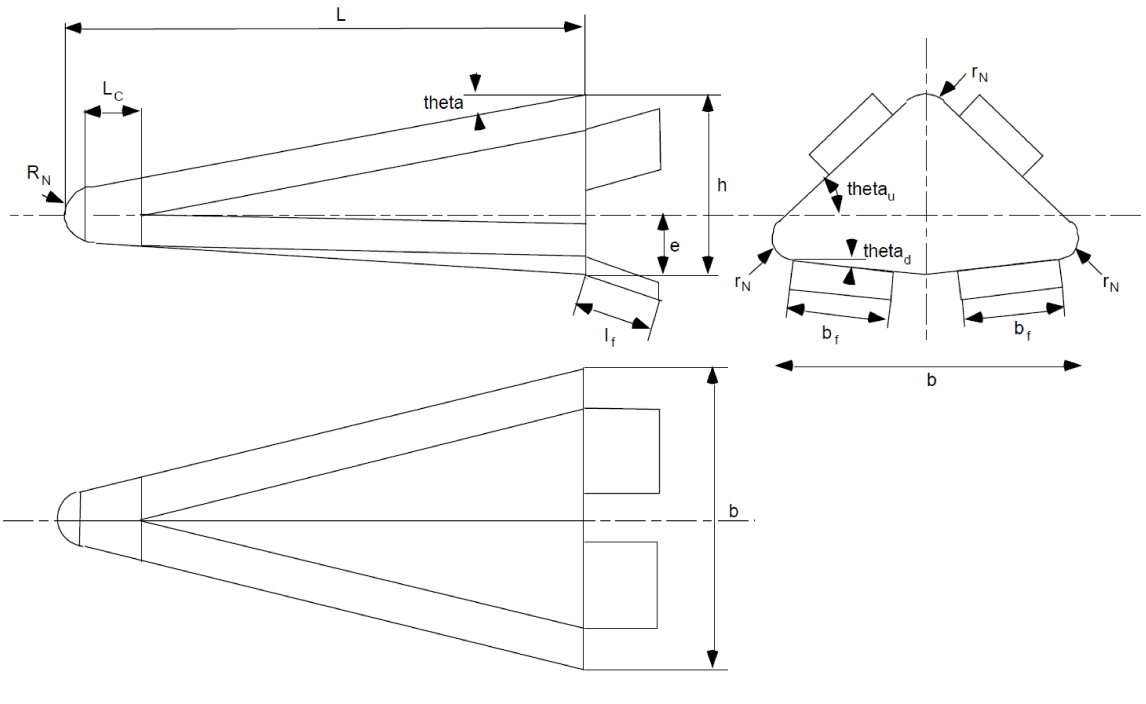

Figure 4.1: Hyperion-2 geometry description and parameter definition (Mooij et al., 1999).

Table 4.1: Hyperion-2 concept 5 geometrical parameters

Parameter	Value	Unit	Parameter	Value	Unit
R_N	0.026	[m]	θ_d	8.233	[deg]
L_c	0.504	[m]	θ_u	56.465	[deg]
θ_c	12.353	[deg]	r_N	0.135	[m]
h	0.988	[m]	b	1.137	[m]
μ	0.271	-	L	2.700	[m]

size in the inner shell is 0.05 m. The mesh at the body is even smaller, with an average size of 0.005 m. On the body surface, no-slip and adiabatic wall conditions are imposed by applying a constant heat flux boundary condition, where the heat flux is set to zero. The grid consists of fully unstructured three dimensional tetrahedral elements. Due to the geometry of the vehicle, a structured boundary layer could not be realised with the used meshing software. The complete mesh has 2,510,916 elements and 478,982 points. To ensure that the effect of the wake is captured in the simulation, the mesh of the wake of the vehicle has been set to twice the body length. The downstream extent of the mesh for the wake was chosen such that the flow in the wake becomes supersonic again. In this way, the downstream (farfield) boundary conditions cannot propagate back towards the vehicle and affect the flow field.

The following solver settings are used for the computations, as obtained through trial and error and experience from the validation phase:

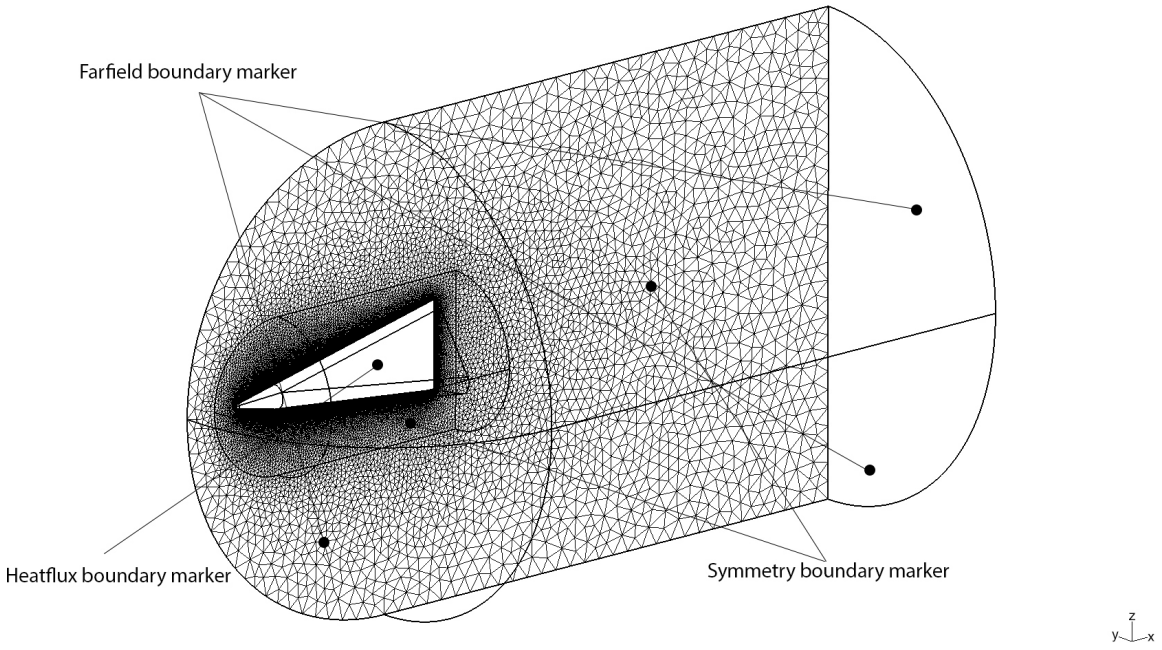

Figure 4.2: Hyperion-2 mesh layout and boundary marker definition.

- Numerical scheme: Jameson-Schmidt-Turkel (JST) second order centered scheme using the Venkatakrishnan's limiter (0.2),
- Integration scheme: Euler implicit with CFL number (time step variable) of 5, no CFL ramping,
- Convergence criteria: A minimum value of the residual (density) is set to -7 (log) and the residual reduction to 5,
- Physical model: Navier-Stokes equations,
- Laminar flow
- Constant heat flux wall of $0\,\mathrm{W/m^2}$

The reference area is $0.69\,\mathrm{m}^2$ (Sudmeijer, 1999). The moment reference origin position is taken equal to the modified Newtonian database of Dijkstra (2012), at $x_{com} = L/2$, $z_{com} = 0$, $y_{com} = 0$. A set of 120 simulations have been run spanning Mach numbers from 6 to 11, 13 and 16 and angles of attack ranging from 0 to 16° with a stepsize of 2°, 20 to 45° with a stepsize of 5°. The freestream conditions (Reynolds and temperature) are taken at 30 km height, where the trajectory optimisation software operates. The temperature is 226.65 K and the Reynolds number is a function of the flow velocity. The complete test matrix is available in appendix A.

4.1.2 Trajectory optimisation

The trajectory optimisation software by Dijkstra (2012) uses the differential evolution algorithm with the third order explicit Adams-Bashforth time integration method for the trajectory, elaborated in section 2.2.2. The equations of motion, reference frames, transformation matrices and Earth model are given in section 2.2.3. The optimal trajectory is obtained for three different cases: unconstrained flight, constrained flight with controllability constraint and constrained flight without controllability constraint. In the latter two cases the other three constraints are the heat flux constraint, shock wave boundary layer interaction constraint and the trimmability constraint. The heat flux constraint is set to $5\,\mathrm{MW/m^2}$, which is the maximum allowable heat flux when active cooling is applied (Mooij and Hänninen, 2002). The shock wave boundary layer interaction constraint is a constraint imposed on the flap deflection to prevent a strong shock wave boundary layer interaction. This interaction induces excessive heating and may cause loss of control effectiveness. Depending on the Mach number and Reynolds number, the flap deflection is limited, hence a maximum flap deflection exists for combinations of Mach and Reynolds number (Dijkstra et al., 2013). For trimmability, the flap positions are set initially for the lower and upper flaps, at -20° and 0° respectively. Initially, the lower flaps are used to achieve pitch trim along the trajectory. When the lower flaps can no longer trim the vehicle, the upper flaps are used. This constraint is effective when the dynamic pressure exceeds $100\,\mathrm{N/m^2}$. To ensure effectiveness of the flaps, a controllability constraint is imposed. The controllability constraint is the ratio between the change in flap deflection and the change in angle of attack ($\Delta\delta/\Delta\alpha$). When this ratio is large, it means that a large flap deflection is necessary to achieve a change in angle of attack, hence the flap becomes ineffective. In case of a small ratio, it means a small flap deflection induces a large change in angle of attack, hence the flap becomes overeffective. The controllability constraint of $\Delta\delta/\Delta\alpha \approx 2$ is imposed (Dijkstra, 2012).

The unconstrained flight only optimises for optimal flight time at a constant Mach number of 10. For this case, the aforementioned constraints are not imposed and the centre of mass position is chosen to be on the centreline at half body distance. This optimisation is performed to test the trajectory simulation software. The constrained flight cases both allow for an optimisation of flight time at a constant Mach number of 10 as objective function. An optimal combination of flap dimensions and centre of mass position to achieve this optimal flight time is thus found. Note that in the trajectory optimisation the x-position of the centre of mass is given as the distance from the back plane of the vehicle. The search parameters for the constrained flights are the centre of mass position and upper and lower flap dimensions. The search space indicates between which bounding values the optimiser must look for the optimal value. A broad search space may lead to slow convergence, or a local optimum. By evaluating several narrow search spaces that show overlap, a global optimum can be found and the optimal values are not dependent on search space boundaries.

The differential evolution algorithm (explained in section 2.2) uses random numbers to generate a trial individual. For example, when a new trial individual is created, a random value between the boundaries of the x-position of the centre of mass is generated and passed on to the trial individual. To be able to reproduce the results, the same random value sequence must be created. This can be achieved by a seed value, passed on to the random number

generator. For any integer used as seed value, a unique ŕandomśequence is generated. To eliminate the choice of seed value, various seed values are used and the results of the optimal trajectory and parameters are compared.

The integration time step is set to 0.25 s. A larger time step decreases the computational time, but also reduces accuracy. The differential evolution generation consists of 15 individuals. More individuals increases the chance on finding a global optimum, although more iterations are required, hence computational time. Only angle of attack control is used as Dijkstra (2012) showed that including bank control does not yield better results. The stop criteria are the maximum number of generations of 5000, the minimum Mach number of 8, or percentage difference between the average fitness and minimum fitness is below 0.005%. The differentiation constant and crossover constant are set to 0.6 (see section 2.2).

Table 4.2: Trajectory optimisation search spaces and random seed values for the constrained flight without controllability constraint.

seed value	2, 13, 16, 26, 66			
search space	1	2	3	4
x_{com}	$[0.6; 0.9]$	$[0.3; 0.9]$	$[0.0; 0.7]$	$[0.8; 1.4]$
z_{com}	$[0.0; 0.2]$	$[0.0; 0.3]$	$[0.0; 0.4]$	$[0.0; 0.6]$
c_{f1}	$[0.0; 0.4]$	$[0.0; 0.4]$	$[0.0; 0.4]$	$[0.0; 0.4]$
c_{f2}	$[0.0; 0.4]$	$[0.0; 0.4]$	$[0.0; 0.4]$	$[0.0; 0.4]$
L_{f1}	$[0.0; 0.785]$	$[0.0; 0.785]$	$[0.0; 0.785]$	$[0.0; 0.785]$
L_{f2}	$[0.0; 0.438]$	$[0.0; 0.438]$	$[0.0; 0.438]$	$[0.0; 0.438]$

The trajectory (unconstrained and constrained) starts with set entry conditions, the initial conditions for the flight. The theoretical Hyperion-2 will be launched with the Brazilian VS-40 and the burnout conditions for the second stage of the launcher is used as an input to the trajectory software. These entry conditions are (Mooij et al., 1999) given in table 4.3.

Table 4.3: Entry conditions of Hyperion-2 (Mooij et al., 1999).

Parameter	Value	Parameter	Value
h_0	120 km	V_0	3300 m/s
τ_0	0°	γ_0	-10.0°
δ_0	0°	χ_0	90°

4.2 CFD simulation results

The range of Mach numbers and angles of attack have been simulated with the settings presented in section 4.1. The computational time of one simulation was approximately 90 min. This section show flow field results for Mach 10 and the aerodynamic coefficient curves for a full angle of attack range. The Reynolds number for this Mach number at an altitude of 30 km is 3.7×10^6. The freestream conditions at this altitude are: freestream temperature $T_\infty = 226.65\,\mathrm{K}$, freestream density $\rho_\infty = 0.018\,\mathrm{kg/m^3}$, freestream laminar viscosiy $\mu_\infty = 1.49 \times 10^{-5}\,\mathrm{kg/(m\,s)}$ and freestream pressue $p_\infty = 1.18 \times 10^3\,\mathrm{N/m^2}$.

Figures 4.3 and 4.4 show the Mach contours of the symmetry plane of the Hyperion, for angles of attack of 0° and 16°, respectively. A shockwave that is close to the body is present due to the high freestream Mach number. The wake is partly subsonic, but reaches supersonic conditions quickly, which can be seen by the black line in the figures. Due to the increase of angle of attack, a more detached shock wave is present and the wake is larger. The shock angle has been measured in the case of $\alpha = 0°$. The shock angle is 14.1°. With a freestream Mach number of 10, the Mach number after the shock should be 6.78 according to oblique shock relations. The result of SU^2 shows a post-shock Mach number of 6.81. Figures 4.5 and 4.6 show two isosurfaces of the three dimensional flowfield. The outer isosurface represents all values of $M = 9$, the inner isosurface is for $M = 1$. These figures illustrate the shock shape in 3D. As can be seen, the shock shape is different in the case of an angle of attack of 16°. The vehicle is at an angle of attack, which causes the flow to encounter a different geometry than for an angle of attack of 0°. Figures 4.7 and 4.8 show the pressure on the lower side of the surface on Hyperion-2. The sharp line is a geometrical feature (the symmetry line) and has no physical meaning. At an angle of attack of 0° a large pressure is present at the nose of the vehicle. There is relatively low pressure on the surface further downstream. At an angle of attack of 16° however, there is a large pressure on the lower side of the body. The difference in pressure in the nose cone and the afterbody is caused by the kink in the geometry between those two parts. This difference in pressure is also visible in the symmetry plane pressure plot (figure 4.11).

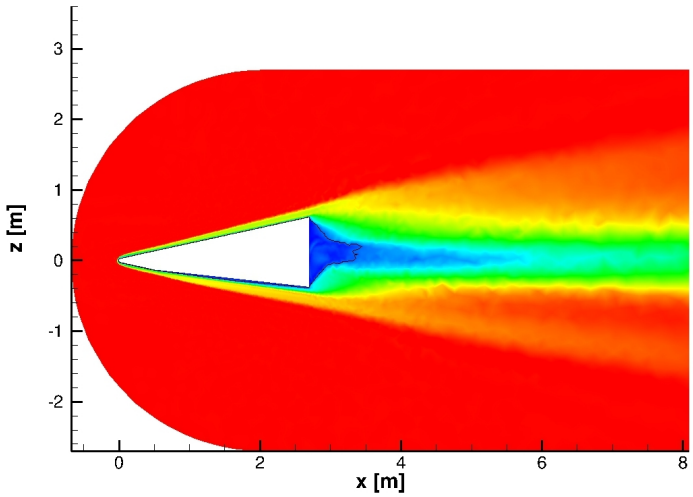

Figure 4.3: Symmetry plane flow field result for $M = 10$ and $\alpha = 0°$. The contours show Mach number. The black line is the contour line for $M = 1$.

Figure 4.9 shows the aerodynamic coefficient curves for $M = 10$. The value of the lift coefficient at zero angle of attack is negative and has a value of -0.019. The lift coefficient at zero angle of attack is 0.072. The maximum L/D occurs at 10° angle of attack, with a value of 2.22. (C_L and C_D are 0.345 and 0.156, respectively). The moment coefficient is -0.463 for this angle of attack. For $M = 10$, the numerical results are displayed in table 4.4. The aerodynamic characteristic curves for all Mach numbers are given in appendix B. The full database of Hyperion-2 generated by SU^2 is given in appendix C.

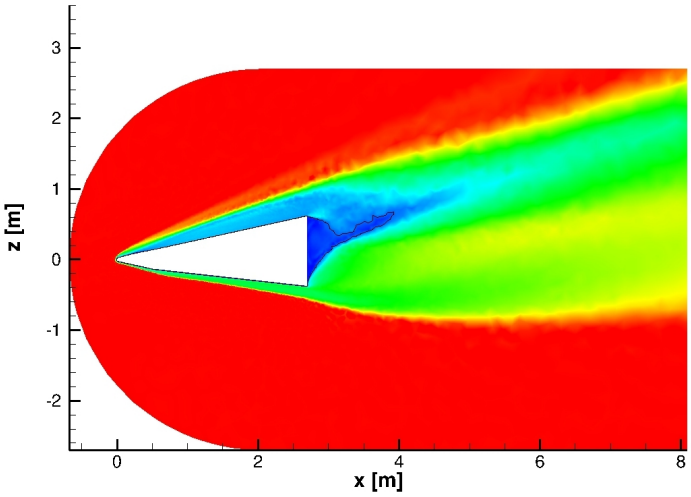

Figure 4.4: Symmetry plane flow field result for $M = 10$ and $\alpha = 16°$. The contours show Mach number. The black line is the contour line for $M = 1$.

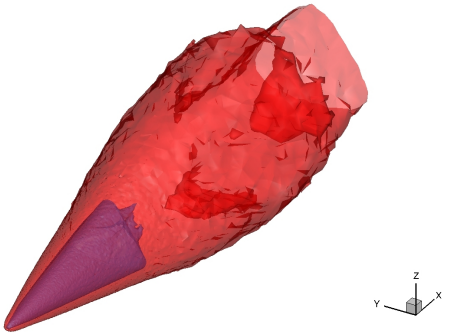

Figure 4.5: Isosurfaces for $M = 10$ and $\alpha = 0°$. The outer isosurface is of Mach 9 and inner of Mach 1.

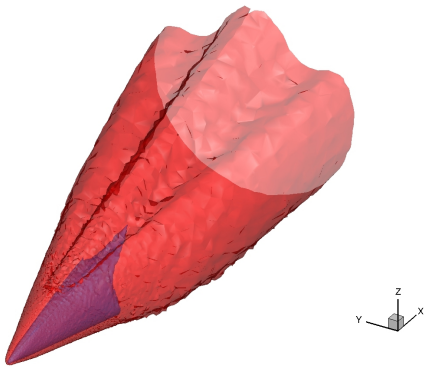

Figure 4.6: Isosurfaces for $M = 10$ and $\alpha = 16°$. The outer isosurface is of Mach 9 and inner of Mach 1.

To check whether the results obtained from SU^2 can be trusted, the simulation result has been compared to a modified Newtonian pressure distribution. The pressure distribution on the symmetry plane of Hyperion-2 is taken and compared to the modified Newtonian distribution. The result for various angles of attack can be found in figure 4.10. The pressure distribution for the Navier-Stokes computation is extremely noisy. Generally, a pressure distribution is much smoother and abrupt variations normally cause separation. However, in this case, the high (spatial) frequency fluctuations are caused by the usage of a fully unstructured grid. By performing a two-dimensional simulation with a structured boundary layer it can be shown that the discontinuities is indeed grid related. Figure 4.11 shows that in the case of a fully structured boundary layer mesh, the pressure distribution shows a continuous line, rather than a noisy one. The unstructured two dimensional result is less noisy than the three dimensional unstructured case. This can be explained by an even unfavourable positioning of the vertices

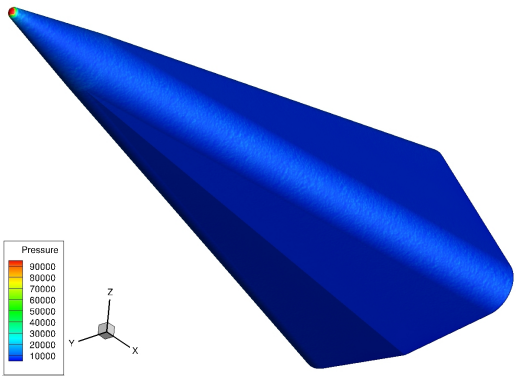

Figure 4.7: Pressure contours over the surface of Hyperion-2 at Mach 10 at $\alpha = 0°$.

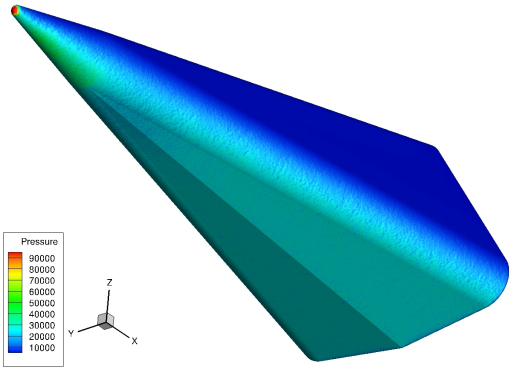

Figure 4.8: Pressure contours over the surface of Hyperion-2 at Mach 10 at $\alpha = 16°$.

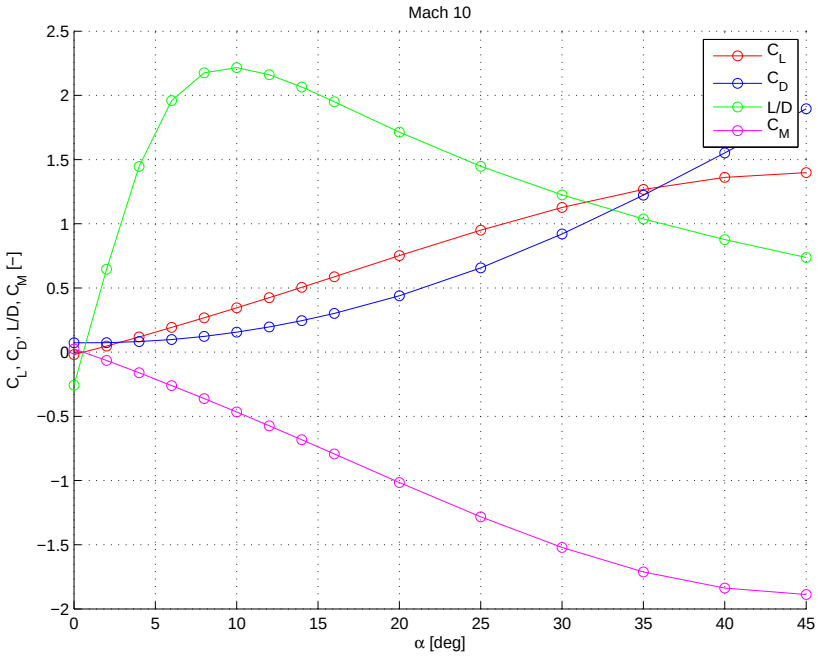

Figure 4.9: Aerodynamic coefficients for $M = 10$ by SU^2.

of the three dimensional elements compared to those of a two dimensional case.

Although the pressure distribution is not completely the same as the Newtonian pressure distribution, the trend of the distribution compares well. Hence, the lift and drag coefficients can be trusted.

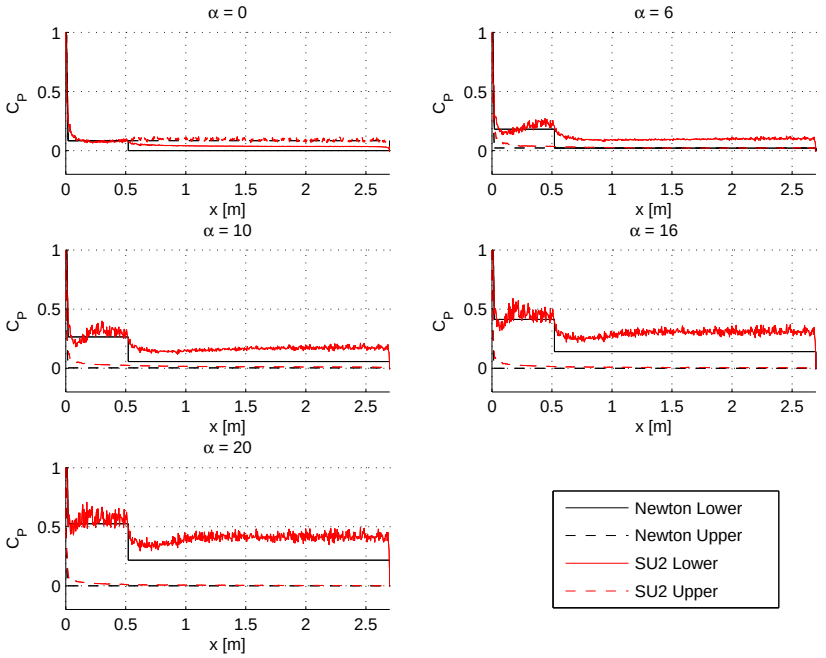

Figure 4.10: Comparison between SU^2 Navier-Stokes computation and modified Newtonian computation for the symmetry plane of Hyperion-2.

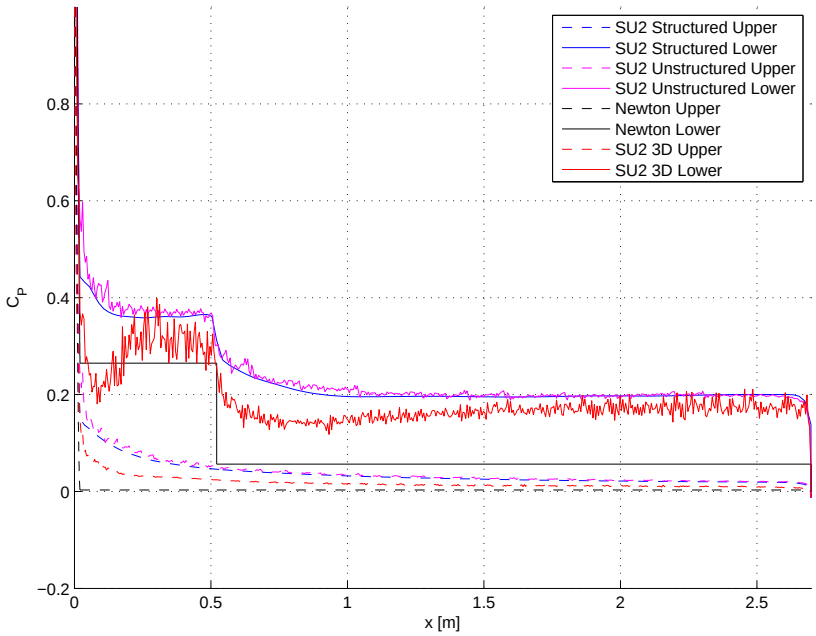

Figure 4.11: Comparison between SU^2 Navier-Stokes computation and modified Newtonian computation for the symmetry plane of Hyperion-2, including a structured and unstructured two dimensional simulation.

4.3 Comparison between CFD results and modified Newtonian result

The results obtained by SU^2 are compared with database generated with the modified Newtonian theory by Dijkstra (2012). The Mach 10 angle of attack range is used to compare the modified Newtonian theory with the Navier-Stokes CFD simulation. Table 4.4 shows the values for C_D, C_L, L/D and C_M per angle of attack for both databases. Figure 4.12 shows the aerodynamic coefficient curves for $M = 10$, for both the modified Newtonian theory as the SU^2 result.

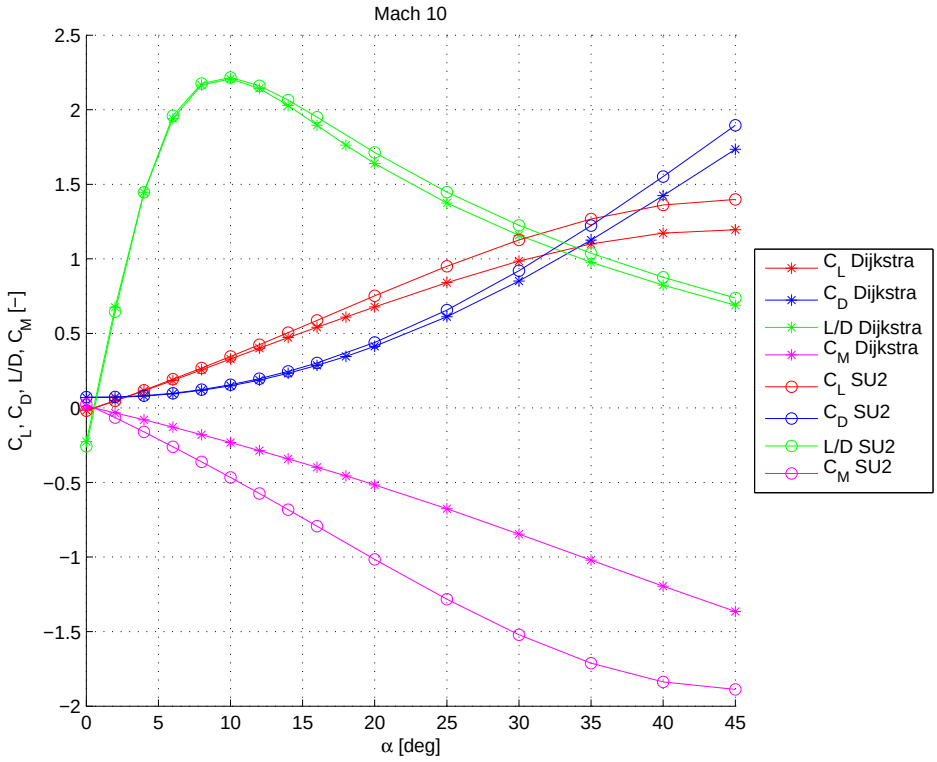

Figure 4.12: Aerodynamic coefficients for $M = 10$ for both modified Newtonian and SU^2 result.

As can be seen in figure 4.12, for low angles of attack ($\alpha < 10°$) the graphs for the lift coefficient, drag coefficient and lift-over-drag are very similar. The difference in the coefficients is approximately 5%. When the angle of attack is increased, the curves obtained by SU^2 show higher values than those for the modified Newtonian theory, resulting in differences up to 15% in lift coefficient and 10% in drag coefficient (see figure 4.13). In the Newtonian result, the surfaces that are in the shadow region of the flow (i.e., there is no direct impingement of the incoming flow on that surface) do not contribute to the pressure distribution, hence to lift- and drag coefficients. SU^2 does take these surfaces into account, which results in higher lift- and higher dragcoefficients. In addition, SU^2 takes viscous effects and the effect of the wake into account. Unfortunately, the contribution to each drag component cannot be identified in SU^2.

The moment coefficient uses the same reference origin for both cases. The difference between SU^2 and the modified Newtonian method is 50% from zero angle of attack and after an angle of attack of 20° the difference becomes lower, eventually 28% at 45°. Although the relative difference becomes smaller, the absolute difference becomes larger. The pressure distribution on the surface of the Hyperion is different in the case of an SU^2 compuation compared to the Newtonian method, which is the cause of the largely different moment coefficient curve.

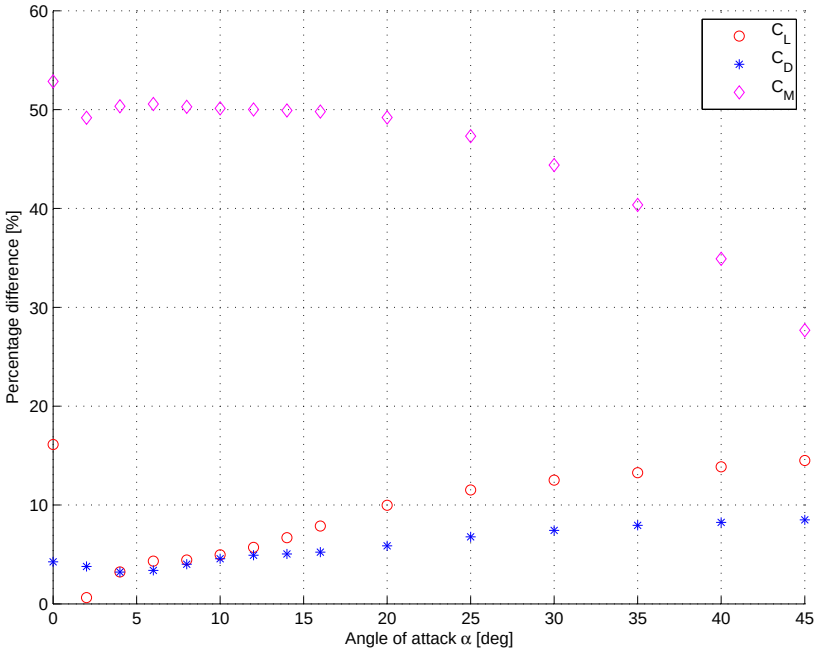

Figure 4.13: Percentage difference between aerodynamic coefficients using both modified Newtonian and SU^2 result.

Table 4.4: Numerical results of CFD and modified Newtonian method for $M = 10$.

	SU^2				Dijkstra (2012)			
α	C_D	C_L	L/D	C_M	C_D	C_L	L/D	C_M
0	0.0723	-0.0186	-0.2576	0.0252	0.0693	-0.0156	-0.2257	0.0119
2	0.0737	0.0476	0.6458	-0.0642	0.0709	0.0479	0.6755	-0.0327
4	0.0820	0.1187	1.4467	-0.1602	0.0794	0.1149	1.4465	-0.0796
6	0.0984	0.1928	1.9595	-0.2602	0.0951	0.1844	1.9405	-0.1287
8	0.1230	0.2677	2.1757	-0.3613	0.1181	0.2558	2.1661	-0.1797
10	0.1558	0.3451	2.2157	-0.4659	0.1487	0.3280	2.2067	-0.2324
12	0.1965	0.4245	2.1610	-0.5731	0.1868	0.4003	2.1428	-0.2865
14	0.2448	0.5054	2.0645	-0.6823	0.2325	0.4716	2.0287	-0.3418
16	0.3013	0.5874	1.9497	-0.7930	0.2855	0.5411	1.8955	-0.3980
20	0.4389	0.7520	1.7135	-1.0152	0.4131	0.6770	1.6389	-0.5158
25	0.6565	0.9501	1.4471	-1.2826	0.6120	0.8406	1.3735	-0.6757
30	0.9200	1.1266	1.2246	-1.5210	0.8516	0.9856	1.1573	-0.8458
35	1.2225	1.2679	1.0371	-1.7117	1.1254	1.0997	0.9772	-1.0210
40	1.5517	1.3610	0.8771	-1.8373	1.4238	1.1724	0.8234	-1.1959
45	1.8960	1.3984	0.7376	-1.8879	1.7349	1.1955	0.6891	-1.3652

4.4 Trajectory optimisation using CFD results

The aerodynamic database generated by SU^2 is used as input for the trajectory optimisation software. In this section, the optimal results of the trajectory simulation will be presented for an unconstrained and constrained flight. The optimisation of the constrained flight without controllability constraint is performed using various random seed values and search spaces. The complete result matrix is given in appendix E.

4.4.1 Unconstrained trajectory

The unconstrained flight is not bounded by any limiting function. This optimisation is done to check whether the trajectory calculation works, before applying constraints. Table 4.5 shows the optimal results for Reynolds sweep and Mach 10 measurement time. The transition Reynolds number $Re_{trans} = 1 \times 10^6$ is within the Reynolds range.

Table 4.5: Optimal results for the unconstrained trajectory

Re_b	Re_e	ΔRe	Δt (s)
4.48×10^5	1.22×10^7	1.18×10^7	31

Figure 4.14 shows the optimal unconstrained trajectory with respect to Reynolds number and heat flux. The vertical dashed lines indicate the constant Mach 10 flight, in which the transition measurement takes place. The horizontal line is the heat flux constraint, although this is not imposed in this case. The maximum heat flux is $5.95 \times 10^6\,\mathrm{W/m^2}$, which exceeds the maximum allowable heat flux by $0.95 \times 10^6\,\mathrm{W/m^2}$.

4.4.2 Constrained trajectory, with controllability constraint

The constrained flight with controllability constraint uses the imposed constraints as specified in section 4.1. In this optimisation, the best centre of mass position and flap dimensions are found for a fully trimmed flight. Based on Sudmeijer (1999), the maximum chord of both flaps is 0.4 m to prevent excessive hinge moments and maximum flap length for the upper and lower flaps are 0.785 m and 0.438 m, respectively. The length of the flaps are bounded by the available length of the vehicle at the locations of the flaps. The optimiser allows the dimensions of the flaps to range between zero and the maximum value. The x_{com} position may vary between 0.6 and 0.9, the z_{com} position between 0.0 and 0.2, as chosen by Dijkstra (2012). Table 4.6 shows the optimal values for this constrained trajectory. Figure 4.15 shows the variation of the Reynolds number and corresponding heat flux values for the optimal trajectory. As can be seen, the Reynolds sweep is rather small, as is the measurement time. The maximum heat flux stays away from the constraint value of $5.0 \times 10^5\,\mathrm{W/m^2}$. The values of the Reynolds sweep, begin and end Reynolds number and constant Mach 10 measurement time is given in table 4.7.

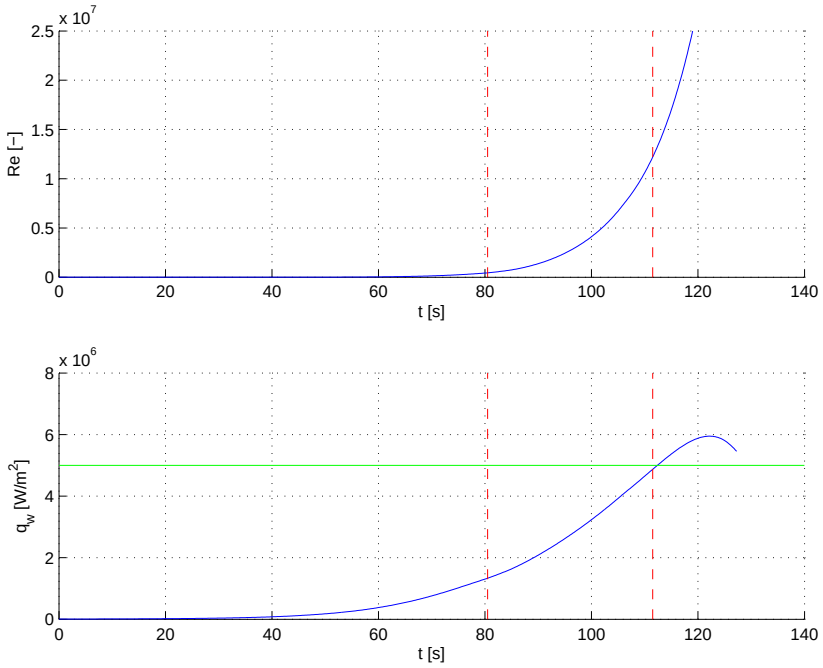

Figure 4.14: Results of the optimal unconstrained flight using the SU^2 database.

Table 4.6: Optimal geometrical results for the constrained trajectory, with controllability constraint

Parameter	Value (m)
x_{com}	0.869
z_{com}	0.006
c_{f1}	0.258
c_{f2}	0.250
L_{f1}	0.597
L_{f2}	0.435

The Reynolds sweep is small compared to the unconstrained flight (1.1758×10^7). The assumed transition Reynolds number of 1×10^6 is in the Reynolds sweep, however, the transition Reynolds number depends on the geometry of the vehicle such that transition might occur at a higher Reynolds number and can therefore not be measured. The measurement time is significantly decreased, to a value of 7.24 s, due to the applied constraints.

Table 4.7: Optimal results for the constrained trajectory with controllability constraint using the SU^2 database.

Re_b	Re_e	ΔRe	Δt (s)
7.47×10^5	1.69×10^6	9.43×10^5	7.24

The dominant constraint is the controllability constraint. Figure 4.16 shows the angle of attack during the flight, the inputs of the upper and lower flaps and the controllability constraint for both flaps. The angle of attack starts at a constant 30° (as determined in the optimisation) and eventually starts varying to maintain an as long as possible constant Mach

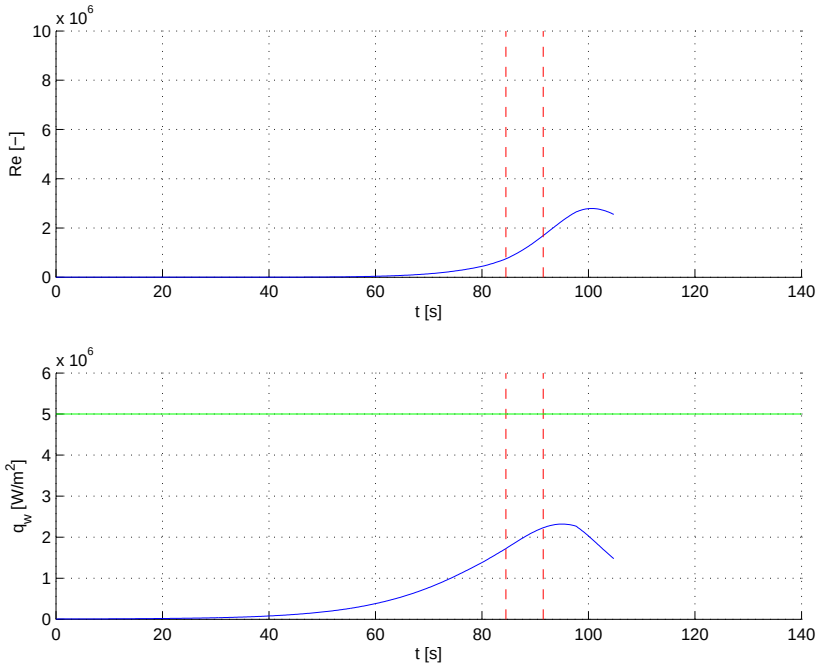

Figure 4.15: Results of the optimal constrained flight with controllability constraint using the SU^2 database.

10 flight (vertical lines). The maximum deflection to prevent shock wave boundary layer interaction is not reached anywhere in the flight (indicated by the purple line in the figure). The upper flap deflection is set to 0° when the flap is unable to trim the vehicle and the lower flap is used to trim the vehicle for the remainder of the flight. The horizontal lines in the last graph of figure 4.16 indicate the controllability constraints. The controllability parameter meets these constraints during the flight.

4.4.3 Constrained trajectory, without controllability constraint

This optimisation neglects the controllability constraint, which was the only constraint that was voilated during a fully constrained flight. This means that the $\Delta\delta/\Delta\alpha$ is not bounded by 1.5 and 2.5. For this trajectory a range of search spaces and random seed values are used in order to ensure an optimal value, independent of search space boundaries. All values and search spaces can be found in appendix E. Again, the optimisation is performed while obtaining optimal values for centre of mass position and flap dimensions. The lower flap dimensions are at their maximum values, while the upper flaps have a small surface area ($S_{flap} = 0.03\,\mathrm{m}^2$). Table 4.8 shows the optimal values for the flap dimensions and centre of mass position. These are the results of a wide search space for the centre of mass position (space 4).

As can be seen in figure 4.17, the complete flight is longer. At the end of the flight, the Mach number is 8, which is one of the stop criteria. The vertical lines indicate the constant Mach 10

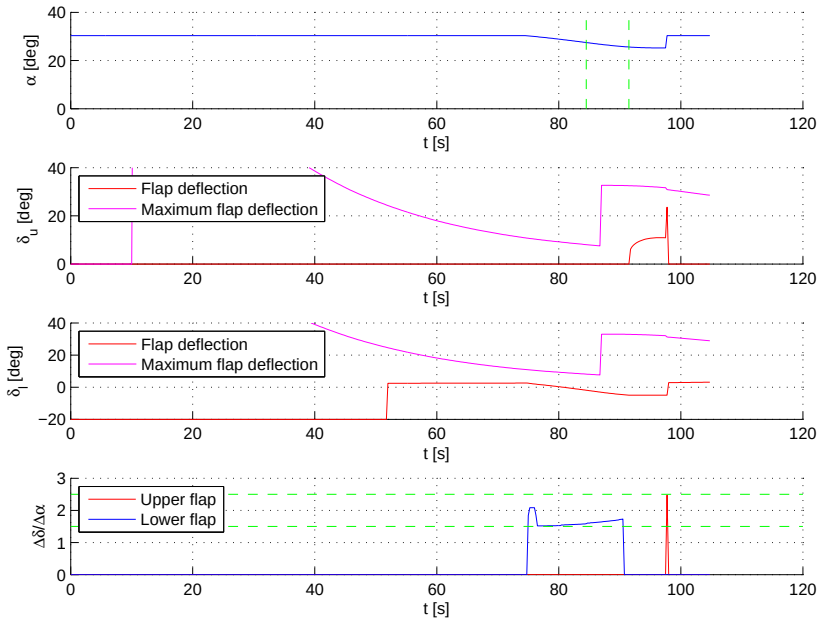

Figure 4.16: Control input of the optimal constrained flight with controllability constraint using the SU^2 database.

Table 4.8: Optimal geometrical results for the constrained trajectory, without controllability constraint.

Parameter	Value (m)
x_{com}	0.920
z_{com}	0.127
c_{f2}	0.400
L_{f2}	0.438

flight time, which is significantly larger than the flight with the controllability constraint. The maximum measurement time is 31.45 s. The Reynolds sweep is also significantly better than in the fully constrained flight. Within this Reynolds sweep (1.20×10^7) transition occurs. Without the controllability constraint, the heat flux constraint of 5×10^6 W/m^2 is reached, such that the trajectory must be adjusted to not violate this constraint. Table 4.9 summarises the optimal results for this trajectory.

Table 4.9: Optimal results for the constrained trajectory, without controllability constraint

Re_b	Re_e	ΔRe	Δt (s)
4.59×10^5	1.25×10^7	1.20×10^7	31.45

Since the position of the centre of mass is shifted to a different optimum compared to the trajectory with controllability constaint, the control inputs and angle of attack control are also different. Figure 4.18 shows the angle of attack, flap inputs and flap controllability. The initial angle of attack is larger, at $\alpha = 35°$. This angle of attack is reduced when Mach 10 is reached to maintain this Mach number. The maximum heat flux is reached at the end of the measurement, where the angle of attack must be increased to prevent violation of

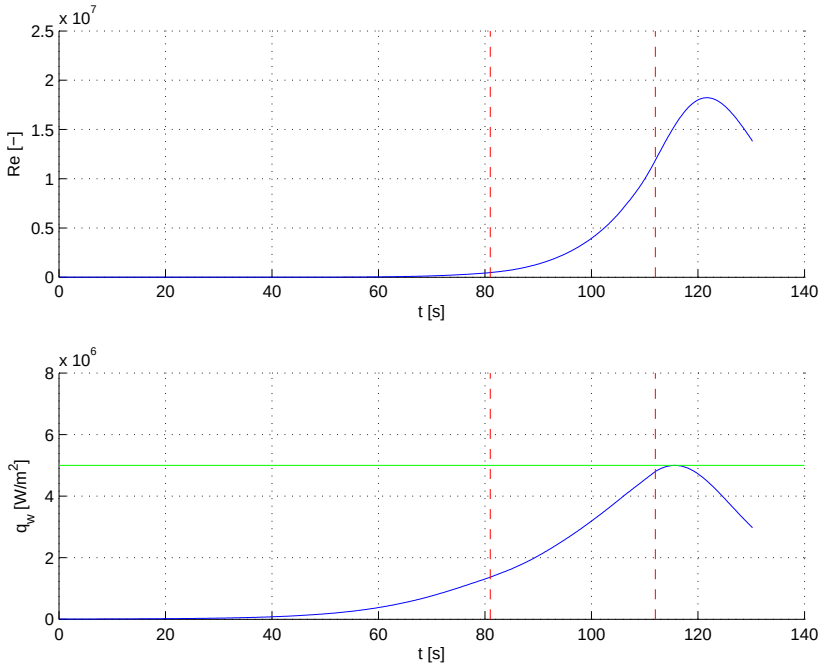

Figure 4.17: Results of the optimal constrained flight without controllability constraint using the SU^2 database.

this constraint. The upper flap is not effective in the measurement phase of the trajectory. Although the flap is deflected, the controllability parameter $\Delta\delta/\Delta\alpha$ reaches values up to 7, indicating that a large flap deflection results in a small angle of attack change, rendering the upper flap ineffective. The lower flap, however, is at times too effective. The flap deflection meets the shock wave boundary layer constraint just before the measurement interval. At the beginning and at the end of the interval, a small deflection of the lower flap results in an equal change in angle of attack ($\Delta\delta/\Delta\alpha = 1.0$).

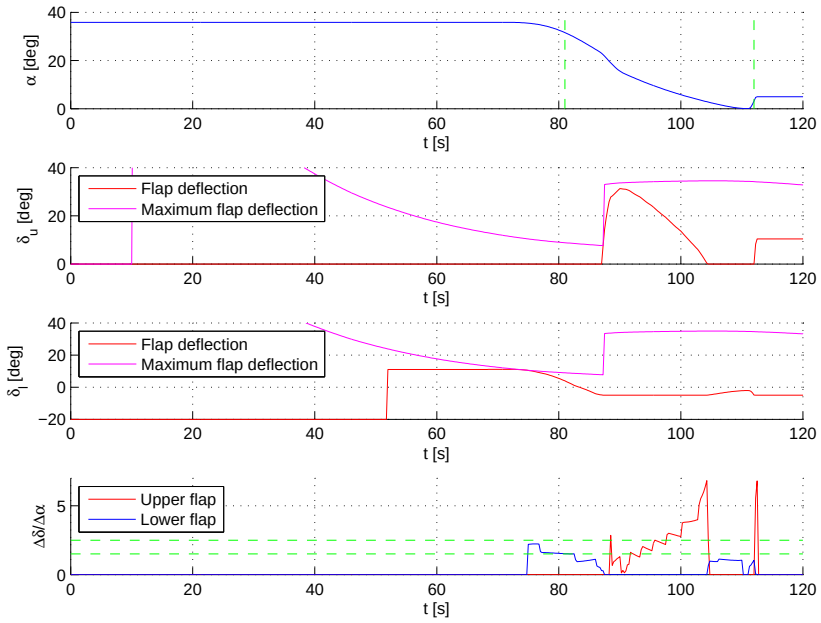

Figure 4.18: Control input of the optimal constrained flight without controllability constraint using the SU^2 database.

4.5 Comparison trajectory optimisation between CFD results and modified Newtonian results

Using the database of Dijkstra (2012) the results of the trajectory simulation have been reproduced. Using these results, the optimal trajectory using the database of SU^2 can be compared with that of Dijkstra (2012). The same settings have been used as in the SU^2 case. Also, a similar range of search spaces and random seed values have been used.

4.5.1 Unconstrained trajectory

Table 4.10 shows the optimal results for the unconstrained trajectory for both cases. The Reynolds sweep is lower for SU^2, a decrease of less than 5%. The measurement time, however, has been increased with 1.25 s. In both trajectories the transition Reynolds number is present.

Table 4.10: Optimal results for the unconstrained trajectory

	Re_b	Re_e	ΔRe	Δt (s)
SU^2	4.48×10^5	1.22×10^7	1.18×10^7	31
Dijkstra (2012)	4.85×10^5	1.28×10^7	1.24×10^7	29.75

Figure 4.19 shows the Reynolds and heat flux trajectory for the unconstrained optimisation. The heat flux violation for the Dijkstra (2012) case is 1.23×10^6 W/m^3, which is an increase of 4.7% compared to the present results. In both cases, the heat flux violation occurs after

the measurement phase of the flight.

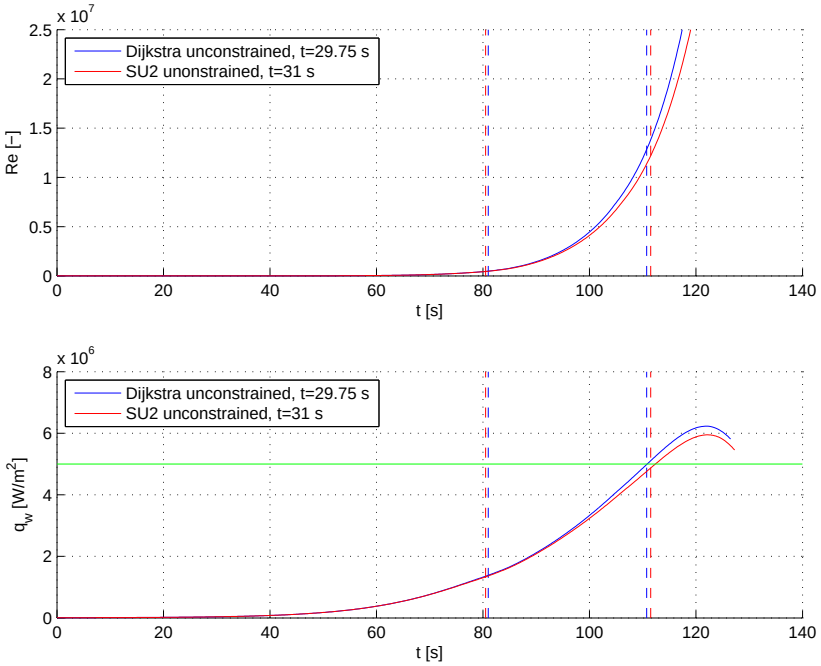

Figure 4.19: Comparison between results from Dijkstra (2012) and the SU^2 database for the unconstrained trajectories.

4.5.2 Constrained trajectory

This section covers the constrained trajectory with and without controllability constraint simultaneously. In the tables and graphs, the suffix (cb) indicates the constrained trajectory with controllability constraint. When there is no suffix, it indicates the constrained trajectory without controllability constraint.

The constrained trajectory takes the optimisation of the flap dimensions and centre of mass into account for a fully trimmed flight. Table 4.11 summarises the geometrical results of the trajectory simulation. In both cases (with or without controllability), the position of the centre of mass in x-direction is farther aft of the vehicle for Dijkstra (2012). Due to the difference in the pressure distribution (see section 4.3), x_{com} must be moved forward for a completely trimmed flight. The position is shifted 9.3% forward to 67.8% of the total body length in this thesis for the controllabilty constrained flight and 2.9% forward to 65.9% of the total body length for the constrained flight without controllability constraint. The position of z_{com} has been moved towards the centreline of the vehicle in the case of SU^2, for both constrained flights. The dimensions of the flaps are at their limiting values (maximum dimensions) when the controllability constraint is not taken into account. Both flaps are larger using the SU^2 database compared to Dijkstra (2012). The upper flap is increased 41.3% in surface area and the lower flap is increased 40.2% in surface area using SU^2.

The shift in centre of mass position and the larger dimensions of the flaps can be explained by the difference in moment coefficient. A larger moment coefficient needs to be countered and with the flaps at the maximum dimensions, the centre of mass position must shift forward. Since the constrained flights are both fully pitch trimmed flights, it becomes clear that, in trajectory determination, a trimmed flight is important and must be used. Comparing the results of the unconstrained flight (no trim) shows that if trim is not included, the effect of the difference in moment coefficient is not taken into account. Furthermore, the flaps are modelled using a modified Newtonian method. To increase the fidelity of the flap aerodynamics, a Navier-Stokes approach must be used.

Table 4.11: Optimal geometrical results for both constrained trajectories, using SU^2 database and from Dijkstra (2012). The parameters are in metre.

Parameter	SU^2 (cb) [m]	Dijkstra (2012) (cb) [m]	SU^2 [m]	Dijkstra (2012) [m]
x_{com}	0.869	0.617	0.920	0.843
z_{com}	0.006	0.064	0.127	0.155
c_{f1}	0.258	0.284	-	-
c_{f2}	0.250	0.239	0.400	0.400
L_{f1}	0.597	0.443	-	-
L_{f2}	0.435	0.325	0.438	0.438

Figure 4.20 shows the trajectories for the Reynolds number and heat flux for the constant Mach 10 flight for all cases. The trajectories are very comparable except for the fully constrained flight using the database from SU^2. The heat flux constraint is met in all other cases just after the measurement phase.

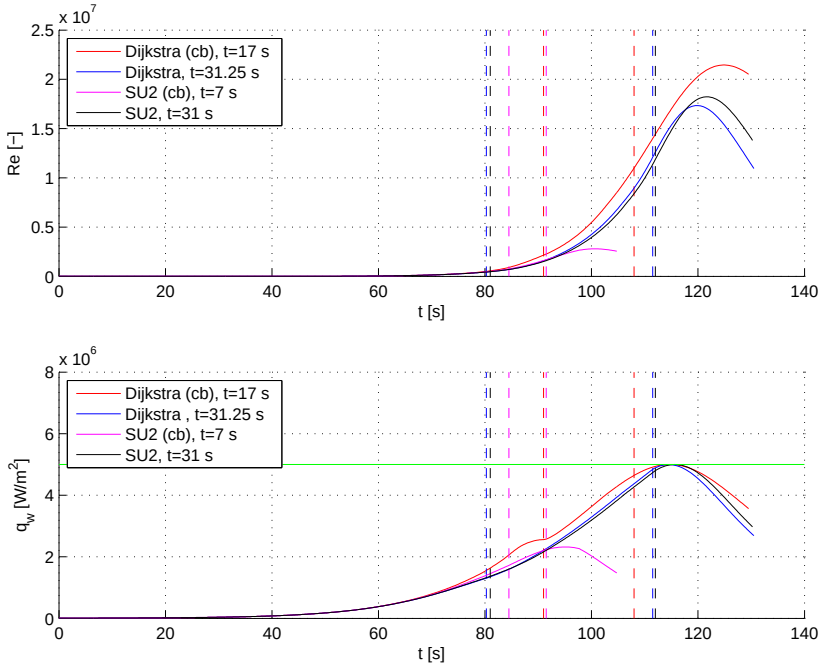

Figure 4.20: Comparison between results from Dijkstra (2012) and the SU^2 database for the constrained trajectories. Suffix (cb) indicates the presence of the controllability constraint.

Table 4.12 summarises the Reynolds ranges and measurement times for all cases. In the fully constrained case, the measurement time is reduced by 57.8% when the improved aerodynamic database is used, while also decreasing the Reynolds sweep by 89%. The differences are caused by the controllability constraint that poses a large limit to the flight profile. In both cases, transition is still measureable, assuming a transition Reynolds number of 1×10^6. The reduction in constant Mach 10 is caused by the fact that the flaps cannot increase the angle of attack of the vehicle sufficiently to reduce the velocity, due to the limit in flap effectiveness. Figure 4.21 shows this in the bottom two figures. On the right, the controllability constraint is active, and the flaps are at the boundary of their control effectiveness. On the left, the controllability constraint is not active and the controllability of the flap is below the constraint value. Due to the short constant Mach 10 flight and the small Reynolds range, chances are that transition cannot be measured accurately. The transition Reynolds is an assumption and the actual transition Reynolds number might be out of the scope of the measurement phase of the flight. The measurement time for the trajectory without controllability constraint are nearly identical, whereas the Reynolds sweep is increased by 3%, comparing the database of SU^2 with the modified Newtonian database.

Table 4.12: Optimal results for both constrained trajectories using the SU^2 database and from Dijkstra (2012).

	Re_b	Re_e	ΔRe	Δt
SU^2 (cb)	7.47×10^5	1.69×10^6	9.43×10^5	7.24
Dijkstra (2012) (cb)	2.15×10^6	1.10×10^7	8.85×10^6	17.18
SU^2	4.59×10^5	1.25×10^7	1.20×10^7	31.45
Dijkstra (2012)	4.35×10^5	1.21×10^7	1.17×10^7	31.46

Figure 4.21 shows the angle of attack during flight, the flap deflections and the controllability parameter of the flaps, for all cases. On the left are the results without the controllability constraint and on the right are the results with the controllability constraint. The dashed graphs are always related to Dijkstra (2012), the solid lines always to present work. Considering the trajectory without the controllability constraint, the angle of attack during flight is similar. In the work of Dijkstra (2012), the upper flap is not used at all, hence there is no flap deflection nor is there a value for the controllability parameter. The lower flap shows similar behaviour, however, the shock wave boundary layer constraint is not met in previous work. The violation of the controllability constraint is also present in the case of Dijkstra (2012), resulting in flaps that are too effective (low $\Delta\delta/\Delta\alpha$).

Considering the fully constrained case, it shows that the angle of attack has a completely different behaviour. To compensate for the difference in centre of mass position, flap dimensions and moment coefficient, the angle of attack using the SU^2 database must be higher than in the case of Dijkstra (2012). In addition, the constant Mach 10 flight for Dijkstra (2012) occurs later than the constant Mach flight using the SU^2 database. The other graphs also show a different control solution, with the trajectory using the SU^2 database pushing the controllability limit.

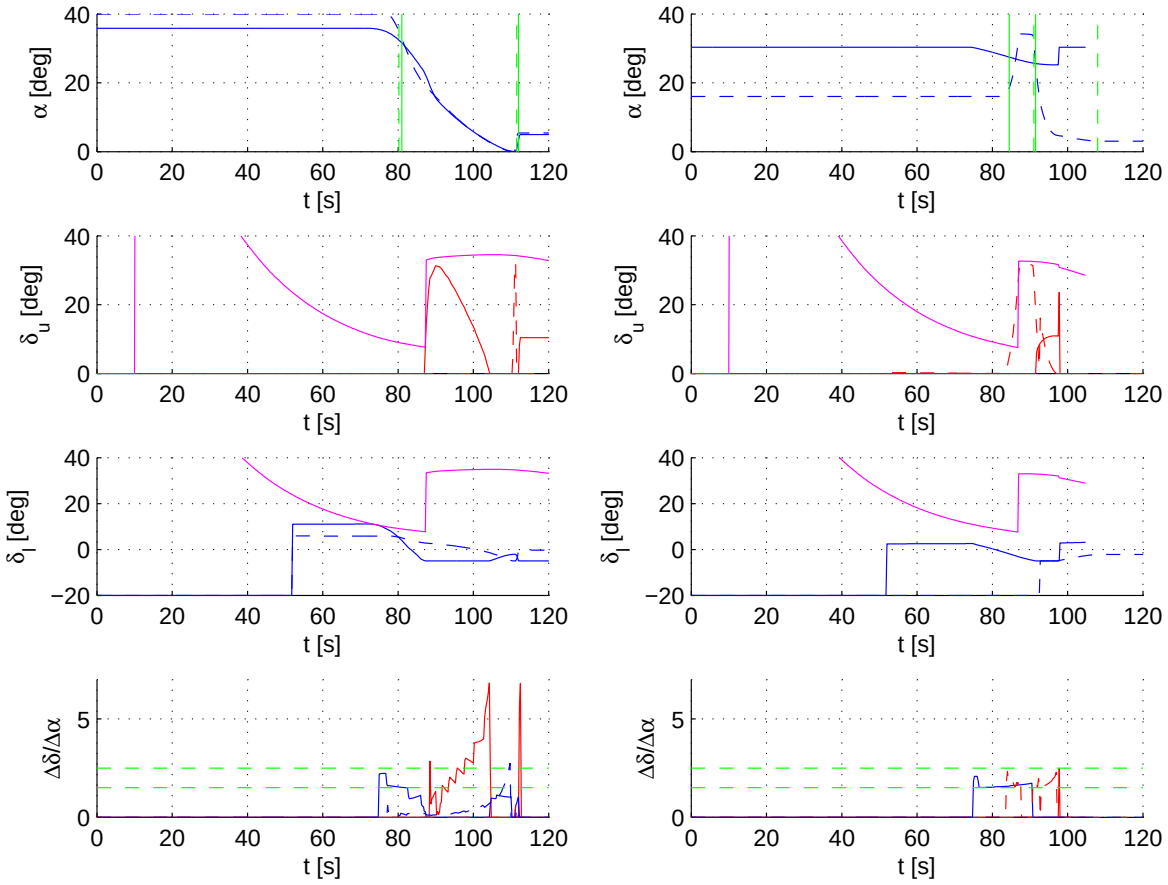

Figure 4.21: Control input results from Dijkstra (2012) and the SU^2 database for the constrained trajectories. On the left, the results without the controllability constraint. On the right the results with controllability constraint. The solid lines are from SU^2 and the dashed lines from Dijkstra (2012).

Chapter 5

Conclusions and recommendations

The answer to the main research question and its subquestions are given in this chapter. To improve the results presented in chapter 4, this chapter will also include a set of recommendations for future research.

5.1 Conclusions

In the introduction of this thesis, the research questions and goals were presented. This section will answer those questions, as well as drawing other conclusions. The main question was formulated as:

Compared to modified Newtonian method results, what is the effect of using Navier-Stokes based aerodynamics for Hyperion-2 on flight-experiment objectives?

The answer to this question has been obtained by completing the following steps. First, the SU^2 software has been validated, focussing on the hypersonic flow regime (shock characteristics, pressure distribution, heat flux). This is done using simple shapes for which measurement data and theory was present. Then, the aerodynamic database of Hyperion-2 has been computed, using SU^2. This database has been compared with a modified Newtonian database of Hyperion-2. Both databases have been used to perform three trajectory optimisations: an unconstrained flight, a constrained flight with controllability constraint and a constrained flight without controllability constrained. These optimisations have also been compared and the performance of all trajectories have been assessed.

The main reasearch question is answered by answering the subquestions. The answer to the main question is partly a result of the CFD simulation and partly that of the trajectory optimisation.

The first subquestion was: *What is the difference in aerodynamic coefficients between the two aerodynamic models?* Chapter 4 has shown that the difference in aerodynamic coefficients can be significant. Given are the modified Newtonian database of Hyperion-2 at Mach 10 and a database that was generated using laminar Navier-Stokes simulations without chemical reactions, body forces, diffusion and radiation (see chapter 2). It was found from the comparison that the lift and drag coefficients are 5% higher in the case of the Navier-Stokes solution for angles of attack of less than 10°. At higher angles of attack (45°), the Navier-Stokes solution has an increase in lift coefficient of 15% and an increase in drag coefficient of 10%. The moment coefficient shows a 50% increase in the case of Navier-Stokes at zero angle of attack and an increase of 28% at 45° angle of attack, compared to a modified Newtonian computation. When trim is not included in the trajectory, the difference in performance between a Navier-Stokes database and a modified Newtonian database does not become clear. Therefore, trim must be used in trajectory optimisation.

The second subquestion was: *What is the difference in estimated maximum heat flux and overall heat flux when comparing the aerodynamic models?* During the validation phase of the thesis work, it was found that the computed heat flux values do not compare with theory (chapter 3). The heat flux can therefore not be compared between aerodynamic models and this subquestion cannot be answered.

The third subquestion is formulated as: *What is the maximum sustained Mach 10 flight time for the improved aerodynamic model given a Reynolds sweep that covers boundary layer transition?* The improved aerodynamic database has been used to optimise the trajectory for a constant Mach 10 flight, whilst measuring transition. The maximum sustained Mach 10 flight time can be achieved with a constrained flight without controllability constraint. This flight time has a duration of 31.45 s. The unconstrained flight has a flight time of 31 s. The worst performance is found in the fully constrained flight, which has a flight time of 7.24 s. It must be noted that the best performance flight with respect to measurement time is violating the controllability constraint, resulting in over- or undereffective flaps. It was found that the upper flap was not effective and the lower flap was too effective. The upper flap can therefore be removed from the vehicle.

The fourth question was: *What is the largest possible Reynolds sweep within the constraints of thermal loads?* The constrained flights do not violate the heat flux constaint. From these two flights it was found that the maximum Reynolds sweep is 1.20×10^7. This is the flight without the controllability constraint. The flight that does take this constraint into account has a Reynolds sweep of only 9.43×10^5. The largest possible Reynolds sweep within the constraints of thermal loads is therefore 1.20×10^7.

By achieving the thesis goal, the main research question can be answered and conclusions not related to the main research question can be drawn. The thesis goal is formulated as:

Determine what the differences are in Reynolds sweep, flight time and optimal centre of mass position using different aerodynamic models, hereby verifying the optimal trajectory of Dijkstra et al. (2013).

In chapter 4, the results obtained to achieve this goal have been presented. Using the aerodynamic database generated by SU^2, the Reynolds sweep could be increased in a constrained flight without controllability constraint by 3%. The difference in constant Mach 10 flight time is negligible. The position of the centre of mass has shifted more towards the nose of the body when using the SU^2 datbase. For the constrained flight with controllability constraint the shift is 9.3% with respect to total body length, whereas without the controllability constraint the shift is 2.9% with respect to the total body length. The final results that are required to reach the final goal are summarised in table 5.1.

Table 5.1: Summary of specific results obtained in the trajectory optimisation. The suffix unc indicates unconstrained flight and cb indicates constrained flight without controllability constraint. The x-position of the centre of mass has been given as percentage of total body length.

	x_{com} (%)	Re_b	Re_e	ΔRe	Δt (s)
SU^2 (unc)	-	4.48×10^5	1.22×10^7	1.18×10^7	31
Dijkstra (2012) (unc)	-	4.85×10^5	1.28×10^7	1.24×10^7	29.75
SU^2 (cb)	67.8	7.47×10^5	1.69×10^6	9.43×10^5	7.24
Dijkstra (2012) (cb)	77.1	2.15×10^6	1.10×10^7	8.85×10^6	17.18
SU^2	65.9	4.59×10^5	1.25×10^7	1.20×10^7	31.45
Dijkstra (2012)	68.8	4.35×10^5	1.21×10^7	1.17×10^7	31.46

5.2 Recommendations

The obtained results in this thesis can be further improved. Recommendations to improve the quality of the work are given in this section.

Aerodynamic model

The aerodynamic model used in this thesis excludes the use of chemical reactions, diffusion, body forces and turbulence. In addition, it was chosen not to use the heat flux computation in SU^2, as it could not properly be validated. The first step in improving the aerodynamic model is to include the heat flux computation in the CFD simulation. To this end, the way the isothermal wall boundary condition is imposed (Neumann) should be changed (to Dirichlet). The engineering method for the heat flux used in this thesis only gives information about the heat flux in the stagnation point, but with a CFD solution, information on the complete surface of the vehicle can be obtained.

Next steps to improve the quality of the results is to include chemical reactions. It has been shown that the increase of drag coefficient below Mach 10 is already 2% when considering finite-rate reacting flow. The increase in drag will increase with Mach number (Wood et al., 1996).

Transition models and turbulence models might increase the fidelity of the aerodynamic model. In present thesis, an increase of 6% in lift coefficient and a 4.7% increase in drag

coefficient has been found when using a turbulence model (SA) for a Mach 10 flight at an angle of attack of 10°. However, this result is not validated, nor the mesh is optimised for turbulence. This must be further investigated.

Numerical methods

In this thesis, the settings of SU^2 have been chosen for robustness and computational time, as a large number of simulations had to be run. The central discretisation scheme has been used mainly since the second order upwind scheme did not produce any results. The upwind scheme is made second order by the MUSCL approach, which relies on the interpolation of primitive variables. In SU^2, every primitive variable is interpolated, rather than only two state variables. The remaining variables can be computed with an equation of state. If the implemented MUSCL approach is changed, the upwind scheme could produce useful results.

The time discretisation method is the implicit Euler method, as this method is able to converge the solution using higher CFL numbers. This decreases computational time with keeping the level of accuracy, comparing to explicit schemes. An implicit Runge-Kutta scheme could be used to increase the order of accuracy, although this is hard to implement.

The quality of the mesh of Hyperion-2 must be improved. Due to limitations of the meshing software, only a fully unstructured three dimensional grid could be produced. To capture the boundary layer properly (thus improving heat flux computation and turbulence models), a structured boundary layer grid with progression is necessary at the surface of the vehicle.

Trajectory optimisation

The conclusions state that a trimmed flight is necessary to take the effect of the moment coefficient into account. The flaps that achieve a trimmed flight are in the trajectory optimisation software modelled using the modified Newtonian theory. The flap aerodynamics can be improved by including the flaps into the aerodynamic database generation. More simulations would be needed to compute the aerodynamic coefficients at several flap deflections. An adjoint approach could be used to analyse the sensitivity of the CFD solution with respect to a certain flap deflection to get a detailed range of flap deflections with a few extra simulations. This adjoint solver is present in SU^2. Furthermore, the upper flaps show limited effectveness in the trajectory optimisation. The use of these flaps for pitch trim should be reconsidered.

Bibliography

[1] Anderson, J.D. *Computational Fluid Dynamics: The Basics with Applications*. McGraw-Hill Education, 1995.

[2] Anderson, J.D. *Hypersonic and High Temperature Gas Dynamics*. American Institute of Aeronautics and Astronautics, 2006.

[3] Billig, F.S. Shock-Wave Shapes Around Spherical- and Cylindrical-Nosed Bodies. *Journal of Spacecraft and Rockets*, 4(6:822,823), June 1967.

[4] Blazek, J. *Computational Fluid Dynamics: Principles and Applications*. Elsevier, 2001.

[5] Butcher, J. *Numerical Methods for Ordinary Differential Equations*. John Wiley & Sons, Ltd, 2008.

[6] Di Benedetto, S., Rufolo, G.C., and Marini, M. European Space Agency Intermediate Experimental Vehicle: Development of an Independent Aerothermodynamic Datbase Tool. *Journal of Aerospace Engineering*, (228:435-454), 2014.

[7] Dijkstra, M. Trajectory Optimization of Hyperion-II for the Study of Hypersonic Aerothermodynamic Phenomena. Master's thesis, Delft University of Technology, 2012.

[8] Dijkstra, M., Mooij, E., and Sudmeijer, K.J. Trajectory Optimization to Support the Study of Hypersonic Aerothermodynamic Phenomena. *AIAA Atmospheric Flight Mechanics (AFM) Conference*, (AIAA-2013-4501), August 2013.

[9] Eggers, T., Longo, J.M.A., Hoerschgen, M., and Stamminger, A. The Hypersonic Flight Experiment SHEFEX. *AIAA/CIRA 13th International Space Planes and Hypersonics Systems and Technologies*, (doi:10.2514/6.2005-3294), May 2005.

[10] European Space Agency, 2011. URL http://www.esa.int/spaceinimages/Images/2011/12/IXV. Retrieved: 06-03-2014.

[11] Fay, J.A. and Riddell, F.R. Theory of Stagnation Point Heat Transfer in Dissociated Air. *Journal of the Aeronautical Sciences*, 25(2:73-85), September 1958.

[12] Feoktistov, V. *Differential Evolution. In Search of Solutions*. Springer, 2006.

[13] Gnoffo, P.A. Planetary-Entry Gas Dynamics. *Annual Review of Fluid Mechanics*, (doi:10.1146/annurev.fluid.31.1.459), 1999.

[14] Griffiths, D. and Higham, D. *Numerical Methods for Ordinary Differential Equations: Initial Value Problems*. Springer, 2010.

[15] Hammond, W.E. *Design Methodologies for Space Transportation Systems*. American Institute of Aeronautics and Astronautics, 2001. ISBN 1563474727.

[16] Hirsch, C. *Numerical Computation of Internal and External Flows*. Elsevier, 2007.

[17] Koppenwallner, G. Fundamentals of Hypersonics: Aerodynamics and Heat Transfer. *Von Kármán Institute for Fluid Dynamics*, February 1984.

[18] Kubota, T. *Investigation of Flow around Simple Bodies in Hypersonic Flow*. PhD thesis, California Institute of Technology, 1957.

[19] Lees, L. and Kubota, T. Inviscid Hypersonic Flow over Blunt-Nosed Slender Bodies. *Journal of the Aeronautical Sciences*, 24(195-202), February 1957.

[20] Lukasiewicz, J. Blast-Hypersonic Flow Analogy Theory and Application. *American Rocket Society Journal*, 32(9:1341-46), September 1962.

[21] Macret, J.L. and Leveugle, T. The ARD (Atmospheric Reentry Demonstrator) Program: An Overview. *9th International Space Planes and Hypersonic Systems and Technologies Conference*, (AIAA-99-4934), 1999.

[22] Meeroff, J. Computational Fluid Dynamic Solutions of Optimized Heat Shields Designed for Earth Entry. Master's thesis, University of Maryland, 2010.

[23] Mooij, E. *The Motion of a Vehicle in a Planetary Atmosphere*. Number LR-768. Delft University of Technology, 1994. URL http://repository.tudelft.nl/view/ir/uuid%3Ae5fce5a0-7bce-4d8e-8249-e23293edbb55/.

[24] Mooij, E. *Aerospace-Plane Flight Dynamics*. PhD thesis, Delft University of Technology, 1998. URL http://repository.tudelft.nl/view/ir/uuid%3Afa4dd59d-3792-4888-8aa5-bdb3c0d90b15/.

[25] Mooij, E. Panel mesh generator based on analytical definitions. Technical Report START-TN-2003, 2005.

[26] Mooij, E. and Hänninen, P.G. Shape Optimisation for a Small Experimental Re-entry Module. *AIAA/AAAF Space Planes and Hypersonic Systems and Technology Conference*, (AIAA-2002-5261), October 2002.

[27] Mooij, E., Kremer, F., and Sudmeijer, K.J. Conceptual Design of a Small Re-entry Test Vehicle. *8th AIAA International Space Planes and Hypersonic Systems and Technologies Conference*, (AIAA-98-1631), November 1998.

[28] Mooij, E., Kremer, F., and Sudmeijer, K.J. Aerodynamic Design of a Low-Cost Re-entry Test Vehicle Using a Taguchi Approach. *9th International Space Planes and Hypersonic Systems and Technologies Conference*, (AIAA-99-4831), 1999.

[29] Palacios, F., Colonno, M.R., Aranake, A.C., Campos, A., Copeland, S.R., Economon, T.D., Lonkar, A.K., Lukaczyk, T.W., Taylor, T.W.R., and Alonso, J.J. Stanford University Unstructured (SU^2): An Open-Source Integrated Computational Environment for Multi-Physics Simulation and Design. *51st AIAA Aerospace Sciences Meeting*, (AIAA-2013-0287), 2013.

[30] Palacios, F., Colonno, M.R., Aranake, A.C., Campos, A., Copeland, S.R., Economon, T.D., Lonkar, A.K., Lukaczyk, T.W., Taylor, T.W.R., and Alonso, J.J. Stanford University Unstructured (SU^2): Open-sourceAnalysis and Design Technology for Turbulent Flows. *52nd AIAA Aerospace Sciences Meeting*, (10.2514/6.2014-0243), 2014.

[31] Pezzella, G., Marino, G., and Rufolo, G.C. Aerodynamic Database Development of the ESA Intermediate Experimental Vehicle. *Acta Astronautica*, (94:57-72), 2014.

[32] Reagan, R. Address Before a Joint Session of Congress on the State of the Union. The American Presidency Project, April 1986.

[33] Stevenson, A. *Oxford Dictionary of English*. Oxford University Press, 2010. ISBN 9780199571123.

[34] Sudmeijer, K.J. Aerodynamic Control Surfaces of Hyperion Model-2. Technical report, 1999.

[35] Sudmeijer, K.J., Mooij, E., and Maree, A.G.M. Aerodynamic Controllability of a Selected Re-entry Test Vehicle. *46th International Astronautical Congress*, (IAF-95-V.4.04), 1995.

[36] Tava, M. and Suzuki, S. Multidisciplinary Design Optimization of the Shape and Trajectory of a Reentry Vehicle. *Transactions of the Japan Society for Aeronautical and Space Sciences*, 45(147:10-19), 2002.

[37] Tewari, A. *Atmospheric and Space Flight Dynamics: Modeling and Simulation with MATLAB and Simulink*. Birkhäuser, 2007.

[38] Walpot, L. *Development and Application of a Hypersonic Flow Solver*. PhD thesis, Delft University of Technology, 2002. URL http://repository.tudelft.nl/view/ir/uuid%3A2e535954-fb97-453f-8365-6e0fb8f17430/.

[39] Weihs, H. Sounding rockets for entry research: Shefex flight test program. Technical report, German Aerospace Center, DLR, 2013. URL http://elib.dlr.de/87623/1/rocket_ballon_2013_shefex.pdf.

[40] Weihs, H., Longo, J.M.A., and Turner, J. The Sharp Edge Flight Experiment SHEFEX II, a Mission Overview and Status. *15th AIAA International Space Planes and Hypersonic Systems and Technologies Conference*, (AIAA-2008-2542), April 2008.

[41] Wood, W.A., Gnoffo, P.A., and Rault, D.F.G. Aerodynamic Analysis of Commercial Experiment Transporter Re-Entry Capsule. *Journal of Spacecraft and Rockets*, 33(5), September 1996.

[42] Zaccagnino, E., Malucchi, G., Marco, V., Drocco, A., Dussy, S., and Préaud, J.P. Intermediate eXperimental Vehicle (IXV), the ESA Re-entry Demonstrator. *AIAA Guidance, Navigation and Control Conference*, (AIAA-2011-6340), August 2011.

Appendix A

Test matrix SU^2 simulations

Angles of attack	0, 2, 4, 6, 8, 10, 12, 14, 16, 20, 25, 30, 35, 40, 45
Freestream viscosity	$1.48835 \times 10^{-5}\,\mathrm{kg/(m\,s)}$
Freestream density	$0.0180199\,\mathrm{kg/m^3}$
Freestream temperature	$266.64\,\mathrm{K}$

Mach number	Reynolds number	Pressure [N/m]
6	2.2×10^6	1.45×10^3
7	2.6×10^6	1.47×10^3
8	2.9×10^6	1.43×10^3
9	3.3×10^6	1.45×10^3
10	3.7×10^6	1.46×10^3
11	4.0×10^6	1.44×10^3
13	4.8×10^6	1.46×10^6
16	5.9×10^6	1.46×10^6

Appendix B

Aerodynamic coefficient curves Hyperion-2 using SU^2

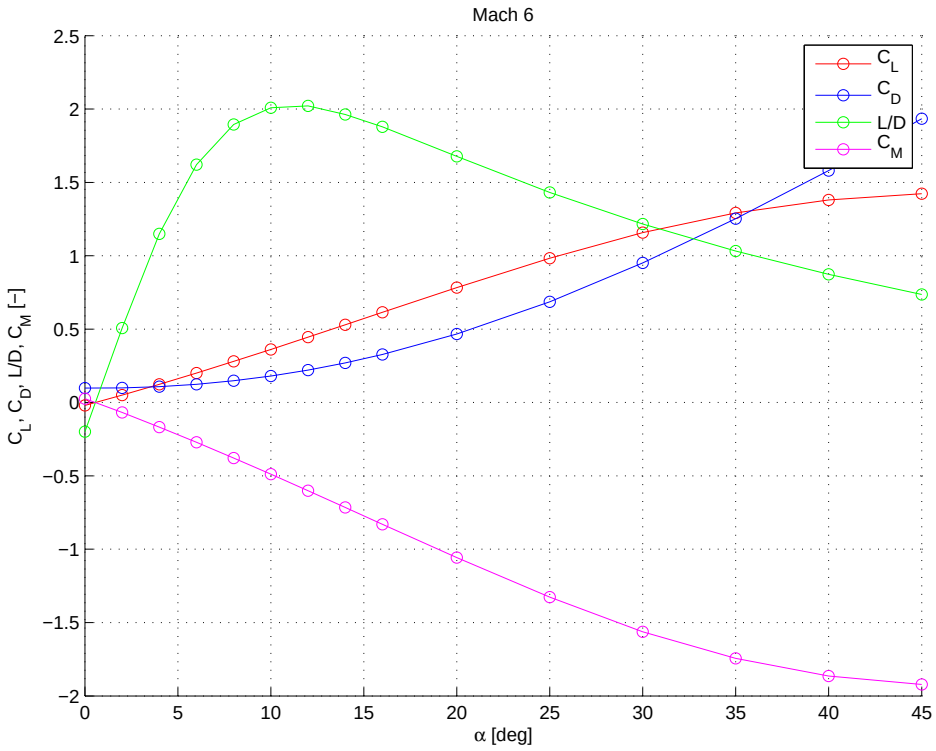

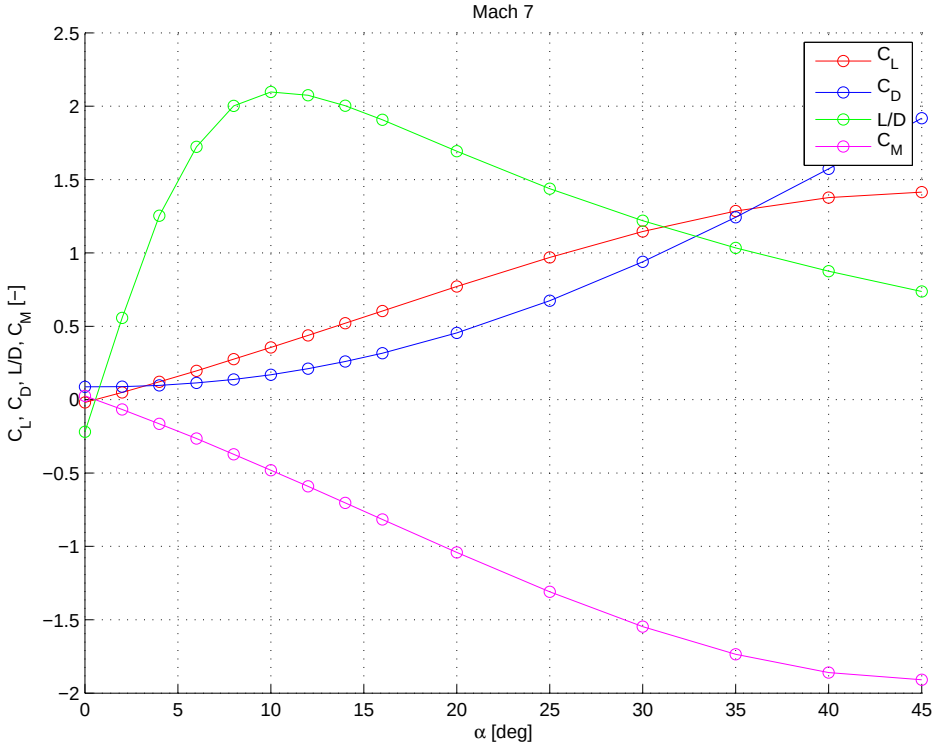
Mach 7
C_L
C_D
L/D
C_M
C_L, C_D, L/D, C_M [–]
α [deg]

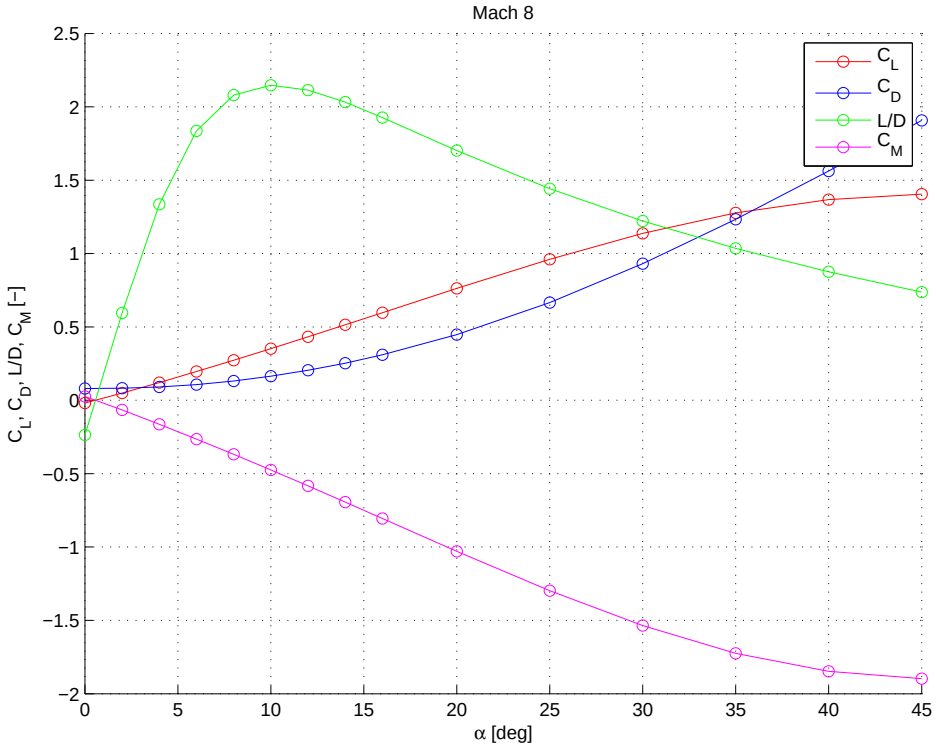
Mach 8
C_L
C_D
L/D
C_M
C_L, C_D, L/D, C_M [–]
α [deg]

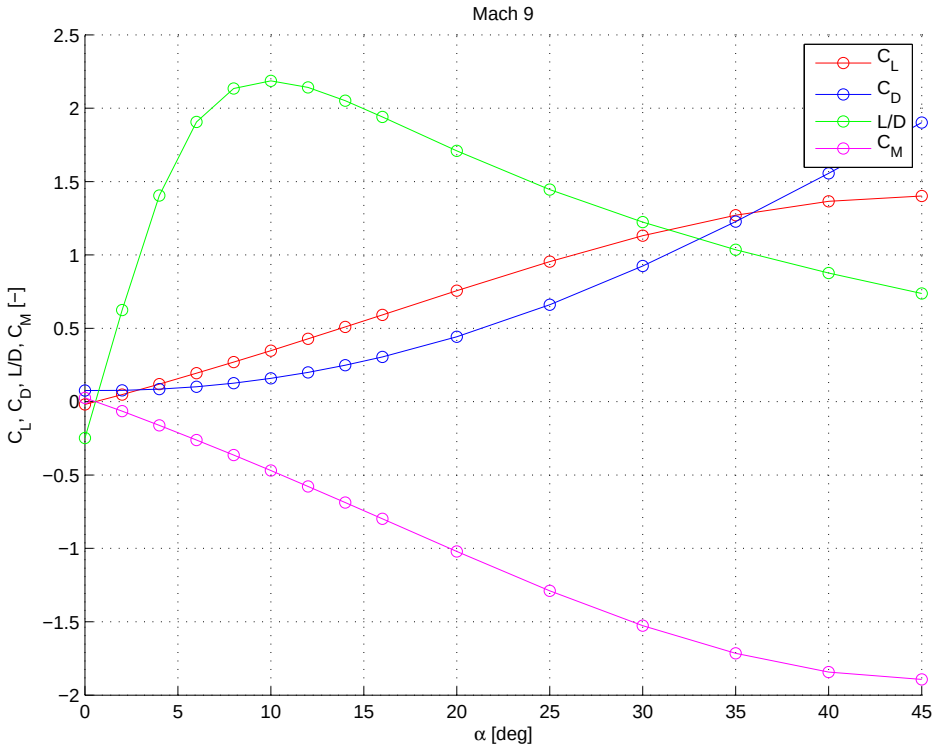
Mach 9
C_L
C_D
L/D
C_M
C_L, C_D, L/D, C_M [–]
α [deg]

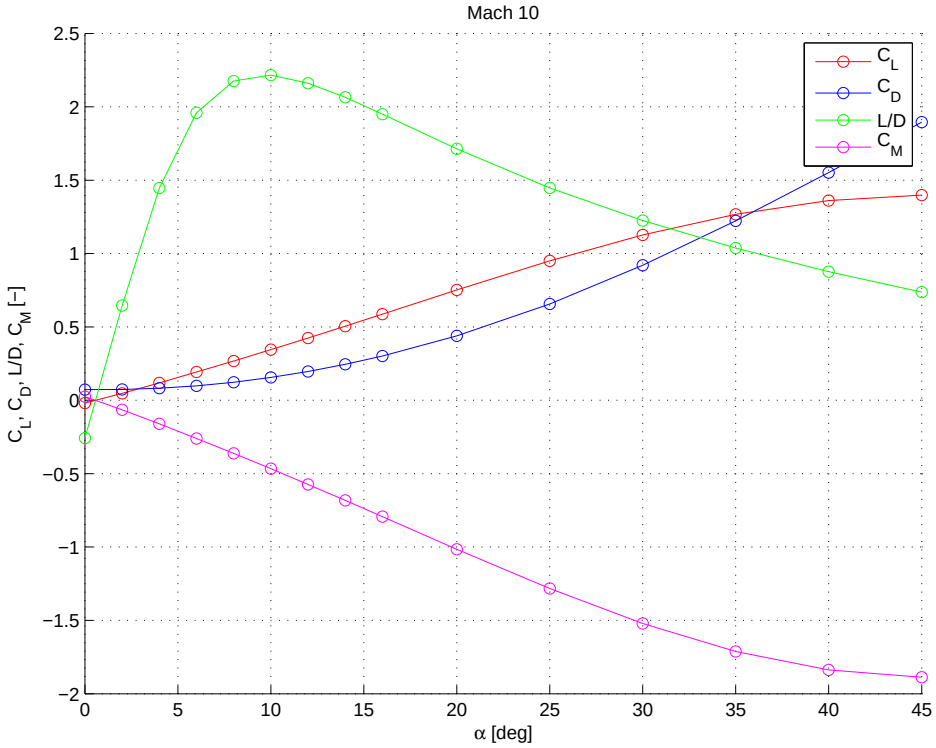
Mach 10
C_L
C_D
L/D
C_M
C_L, C_D, L/D, C_M [–]
α [deg]

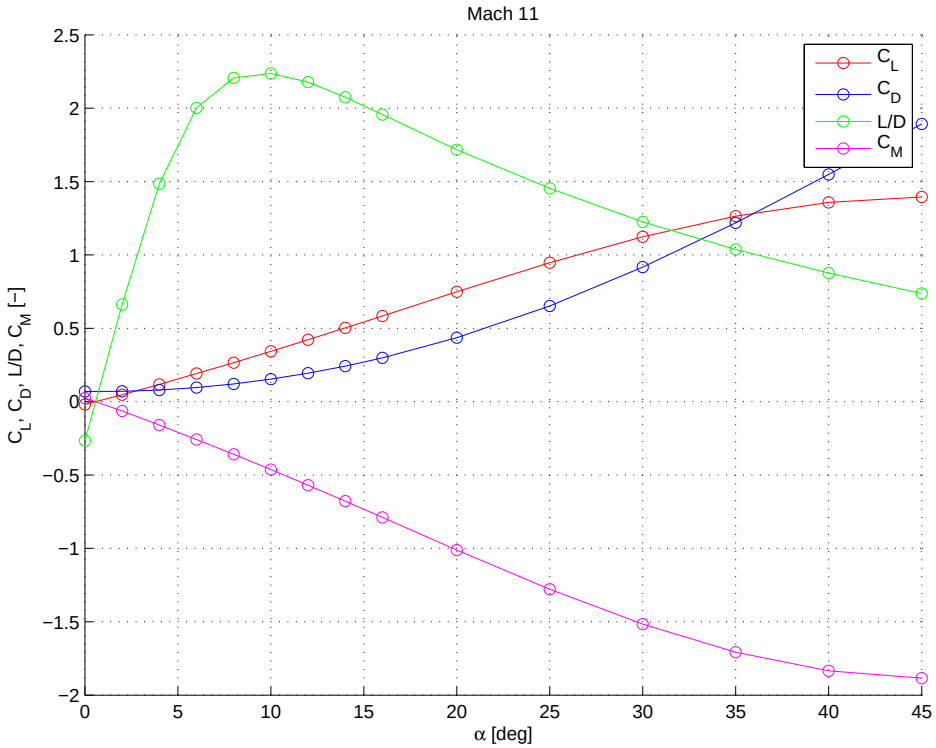
Mach 11
C_L
C_D
L/D
C_M
C_L, C_D, L/D, C_M [–]
α [deg]

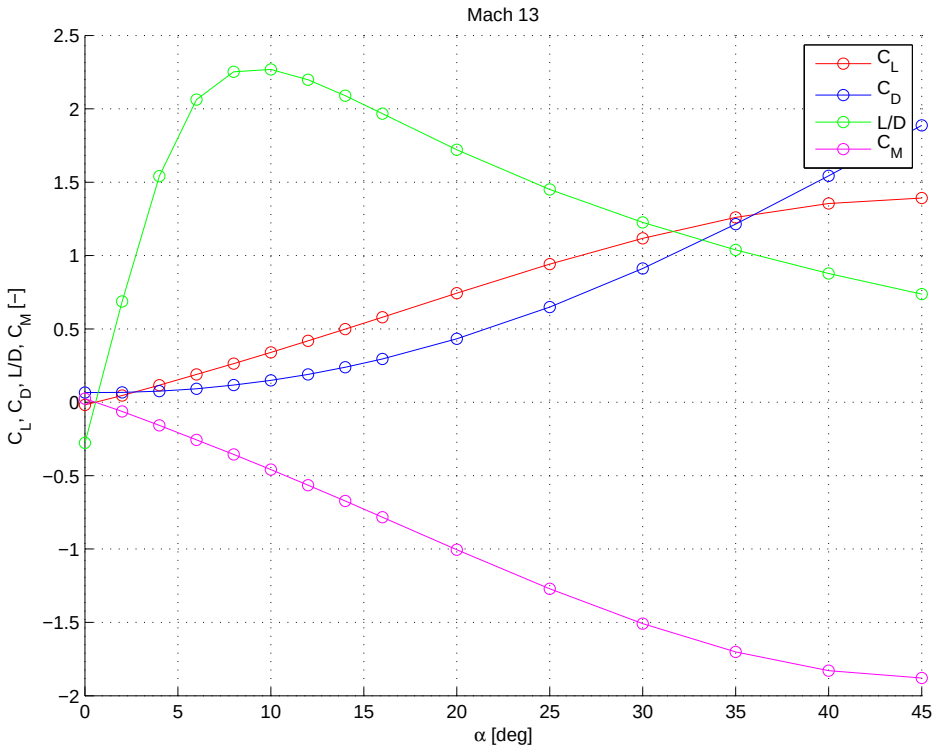
Mach 13
C_L
C_D
L/D
C_M
C_L, C_D, L/D, C_M [–]
α [deg]

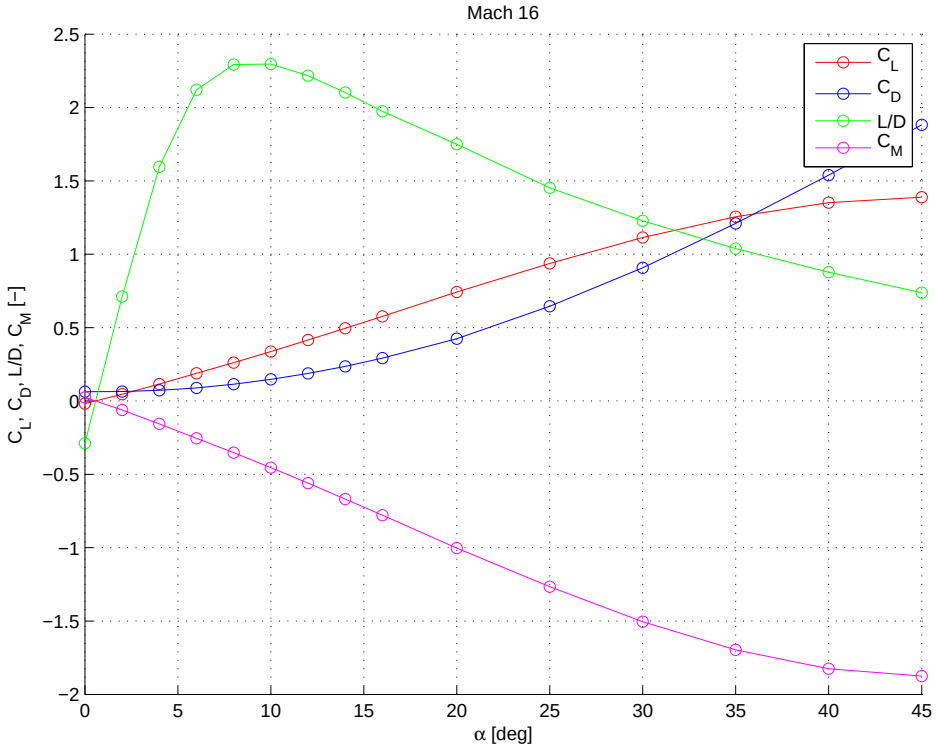
Mach 16
C_L
C_D
L/D
C_M
C_L, C_D, L/D, C_M [−]
α [deg]
2.5
2
1.5
1
0.5
0
−0.5
−1
−1.5
−2
0
5
10
15
20
25
30
35
40
45

Appendix C

Aerodynamic database Hyperion-2 using SU^2

$x_{com} = 1.35$, $z_{com} = 0.0$

α	$\mathbf{C_D}$	$\mathbf{C_L}$	$\mathbf{C_M}$
M = 6			
0	0.097948	-0.019493	0.026315
2	0.099528	0.050472	-0.068137
4	0.10811	0.12423	-0.167711
6	0.123938	0.2009	-0.271215
8	0.147958	0.28036	-0.378486
10	0.179936	0.36148	-0.487998
12	0.22036	0.44544	-0.601344
14	0.27006	0.52996	-0.715446
16	0.32724	0.61492	-0.830142
20	0.46654	0.78282	-1.056807
25	0.68646	0.98292	-1.326942
30	0.95154	1.15788	-1.563138
35	1.25214	1.29194	-1.744119
40	1.5806	1.38084	-1.864134
45	1.93406	1.42328	-1.921428
M = 7			
0	0.08732	-0.019146	0.025848
2	0.08897	0.049564	-0.066911
4	0.097528	0.122218	-0.164994
6	0.113822	0.19615	-0.264802
8	0.137852	0.27606	-0.372681
10	0.169812	0.35604	-0.480654
12	0.21102	0.43784	-0.591084
14	0.25996	0.52084	-0.703134
16	0.31682	0.60446	-0.816021
20	0.45546	0.77104	-1.040904

α	$\mathbf{C_D}$	$\mathbf{C_L}$	$\mathbf{C_M}$
25	0.67434	0.9698	-1.30923
30	0.93958	1.14574	-1.546749
35	1.24284	1.2857	-1.735695
40	1.57258	1.37752	-1.859652
45	1.91808	1.41406	-1.908981
M = 8			
0	0.080514	-0.018974	0.025615
2	0.081992	0.04881	-0.065894
4	0.09048	0.12088	-0.163188
6	0.106688	0.195878	-0.264435
8	0.131064	0.27254	-0.367929
10	0.163852	0.35172	-0.474822
12	0.20444	0.43222	-0.583497
14	0.25304	0.51426	-0.694251
16	0.3099	0.59696	-0.805896
20	0.44794	0.76256	-1.029456
25	0.66628	0.96104	-1.297404
30	0.9308	1.13722	-1.535247
35	1.23342	1.27756	-1.724706
40	1.56222	1.368	-1.8468
45	1.90768	1.40532	-1.897182
M = 9			
0	0.075812	-0.018778	0.02535
2	0.07716	0.048154	-0.065008
4	0.085184	0.119642	-0.161517
6	0.10184	0.194152	-0.262105
8	0.126442	0.26984	-0.364284
10	0.159084	0.34786	-0.469611
12	0.199746	0.42784	-0.577584
14	0.24818	0.50914	-0.687339
16	0.30482	0.59148	-0.798498
20	0.44266	0.75644	-1.021194
25	0.66066	0.95484	-1.289034
30	0.92462	1.13108	-1.526958
35	1.22676	1.27062	-1.715337
40	1.55644	1.36498	-1.842723
45	1.9017	1.4019	-1.892565
M = 10			
0	0.072324	-0.018633	0.025155
2	0.07369	0.04759	-0.064246
4	0.082036	0.11868	-0.160218
6	0.098376	0.192772	-0.260242
8	0.123024	0.26766	-0.361341
10	0.15577	0.34514	-0.465939
12	0.196456	0.42454	-0.573129

α	$\mathbf{C_D}$	$\mathbf{C_L}$	$\mathbf{C_M}$
14	0.24482	0.50544	-0.682344
16	0.30126	0.58738	-0.792963
20	0.43888	0.752	-1.0152
25	0.65654	0.9501	-1.282635
30	0.92002	1.12664	-1.520964
35	1.2225	1.2679	-1.711665
40	1.55172	1.36098	-1.837323
45	1.89598	1.39844	-1.887894
M = 11			
0	0.069674	-0.018503	0.024979
2	0.0711	0.047116	-0.063607
4	0.079398	0.117936	-0.159214
6	0.09572	0.191666	-0.258749
8	0.120482	0.26592	-0.358992
10	0.153342	0.34294	-0.462969
12	0.193806	0.42202	-0.569727
14	0.24222	0.5026	-0.67851
16	0.29858	0.58426	-0.788751
20	0.43626	0.7488	-1.01088
25	0.65172	0.94744	-1.279044
30	0.9168	1.12334	-1.516509
35	1.2189	1.2647	-1.707345
40	1.54884	1.35848	-1.833948
45	1.89214	1.3957	-1.884195
M = 13			
0	0.06611	-0.018286	0.024686
2	0.06752	0.046424	-0.062672
4	0.07579	0.116816	-0.157702
6	0.092134	0.190038	-0.256551
8	0.11702	0.26352	-0.355752
10	0.149816	0.33986	-0.458811
12	0.190316	0.4184	-0.56484
14	0.23864	0.49852	-0.673002
16	0.29492	0.57998	-0.782973
20	0.43228	0.744	-1.0044
25	0.64914	0.94188	-1.271538
30	0.91176	1.11766	-1.508841
35	1.21392	1.26032	-1.701432
40	1.54376	1.35484	-1.829034
45	1.88684	1.3919	-1.879065
M = 16			
0	0.062836	-0.018089	0.02442
2	0.064276	0.045742	-0.061752
4	0.072546	0.115726	-0.15623
6	0.088972	0.18862	-0.254637

α	$\mathbf{C_D}$	$\mathbf{C_L}$	$\mathbf{C_M}$
8	0.113924	0.26118	-0.352593
10	0.146756	0.33696	-0.454896
12	0.187216	0.41506	-0.560331
14	0.23544	0.49494	-0.668169
16	0.29186	0.57634	-0.778059
20	0.42438	0.74276	-1.002726
25	0.6453	0.9377	-1.265895
30	0.90772	1.11438	-1.504413
35	1.20982	1.25624	-1.695924
40	1.53944	1.35134	-1.824309
45	1.88228	1.38884	-1.874934

Appendix D

Aerodynamic database Hyperion-2 using modified Newtonian theory

$x_{com} = 1.35$, $z_{com} = 0.0$

α	$\mathbf{C_D}$	$\mathbf{C_L}$	$\mathbf{C_M}$
M = 3			
0	0.06637	-0.01499	0.01137
2	0.06796	0.0459	-0.0313
4	0.0761	0.11009	-0.07627
6	0.09111	0.17679	-0.12332
8	0.11319	0.24519	-0.17222
10	0.14249	0.31443	-0.22274
12	0.17904	0.38366	-0.27462
14	0.22281	0.45201	-0.32762
16	0.27365	0.51872	-0.38154
18	0.3314	0.58404	-0.4368
20	0.39596	0.64896	-0.49436
25	0.58665	0.80578	-0.64767
30	0.81631	0.94475	-0.81072
35	1.07873	1.05413	-0.97863
40	1.36478	1.12376	-1.1463
45	1.66298	1.14596	-1.30862
M = 4			
0	0.06774	-0.01529	0.0116
2	0.06936	0.04684	-0.03194
4	0.07767	0.11235	-0.07784
6	0.09298	0.18043	-0.12585
8	0.11552	0.25023	-0.17576
10	0.14542	0.32089	-0.22732
12	0.18272	0.39154	-0.28027

α	$\mathbf{C_D}$	$\mathbf{C_L}$	$\mathbf{C_M}$
14	0.22739	0.4613	-0.33436
16	0.27928	0.52938	-0.38938
18	0.33821	0.59604	-0.44577
20	0.4041	0.6623	-0.50452
25	0.5987	0.82234	-0.66098
30	0.83309	0.96417	-0.82738
35	1.1009	1.07579	-0.99874
40	1.39283	1.14686	-1.16986
45	1.69716	1.16951	-1.33552
M = 5			
0	0.06838	-0.01544	0.01171
2	0.07001	0.04729	-0.03224
4	0.0784	0.11342	-0.07857
6	0.09386	0.18214	-0.12704
8	0.11661	0.2526	-0.17743
10	0.14679	0.32393	-0.22947
12	0.18445	0.39525	-0.28292
14	0.22954	0.46567	-0.33752
16	0.28192	0.53439	-0.39307
18	0.34142	0.60169	-0.45
20	0.40793	0.66857	-0.5093
25	0.60438	0.83013	-0.66724
30	0.84098	0.9733	-0.83522
35	1.11133	1.08599	-1.00821
40	1.40602	1.15772	-1.18094
45	1.71324	1.18059	-1.34817
M = 7.5			
0	0.06902	-0.01558	0.01182
2	0.07067	0.04773	-0.03255
4	0.07914	0.11448	-0.07931
6	0.09474	0.18384	-0.12823
8	0.1177	0.25496	-0.17909
10	0.14817	0.32697	-0.23162
12	0.18618	0.39895	-0.28557
14	0.23169	0.47003	-0.34068
16	0.28456	0.5394	-0.39675
18	0.34461	0.60732	-0.45421
20	0.41175	0.67483	-0.51407
25	0.61003	0.83791	-0.67349
30	0.84886	0.98242	-0.84304
35	1.12174	1.09615	-1.01765
40	1.41919	1.16856	-1.192
45	1.72928	1.19165	-1.36079
M = 10			
0	0.06925	-0.01563	0.01186

α	$\mathbf{C_D}$	$\mathbf{C_L}$	$\mathbf{C_M}$
2	0.0709	0.04789	-0.03265
4	0.0794	0.11485	-0.07957
6	0.09505	0.18444	-0.12865
8	0.11809	0.2558	-0.17967
10	0.14865	0.32803	-0.23237
12	0.18679	0.40026	-0.2865
14	0.23245	0.47157	-0.3418
16	0.28549	0.54116	-0.39804
18	0.34574	0.60931	-0.4557
20	0.4131	0.67704	-0.51575
25	0.61203	0.84064	-0.67569
30	0.85163	0.98563	-0.84579
35	1.1254	1.09974	-1.02097
40	1.42382	1.17238	-1.19589
45	1.73493	1.19554	-1.36524
M = 12.5			
0	0.06935	-0.01566	0.01188
2	0.07101	0.04796	-0.0327
4	0.07952	0.11503	-0.07969
6	0.09519	0.18472	-0.12885
8	0.11826	0.25618	-0.17994
10	0.14888	0.32853	-0.23273
12	0.18707	0.40086	-0.28694
14	0.2328	0.47228	-0.34231
16	0.28592	0.54198	-0.39864
18	0.34626	0.61023	-0.45638
20	0.41372	0.67806	-0.51653
25	0.61295	0.84191	-0.67671
30	0.85292	0.98712	-0.84707
35	1.1271	1.1014	-1.02251
40	1.42598	1.17415	-1.1977
45	1.73755	1.19735	-1.3673
M = 20			
0	0.06946	-0.01568	0.0119
2	0.07112	0.04804	-0.03276
4	0.07965	0.11521	-0.07982
6	0.09535	0.18502	-0.12906
8	0.11846	0.2566	-0.18024
10	0.14912	0.32907	-0.23311
12	0.18738	0.40152	-0.28741
14	0.23318	0.47305	-0.34287
16	0.28639	0.54287	-0.3993
18	0.34683	0.61123	-0.45713
20	0.4144	0.67917	-0.51738
25	0.61396	0.84329	-0.67782

α	$\mathbf{C_D}$	$\mathbf{C_L}$	$\mathbf{C_M}$
30	0.85431	0.98873	-0.84846
35	1.12895	1.1032	-1.02419
40	1.42831	1.17608	-1.19966
45	1.7404	1.19931	-1.36954

Appendix E

Result matrix trajectory optimisation using SU^2 database

Sp	Sd	x_{com}	z_{com}	c_{f1}	c_{f2}	L_{f1}	L_{f2}	Δt	ΔRe	Re_b	Re_e
1	2	0.900	0.195	0.398	0.400	0.071	0.438	31.32	1.17E7	4.58E5	1.22E7
1	13	0.899	0.193	0.376	0.398	0.078	0.438	31.31	1.19E7	4.58E5	1.23E7
1	16	0.900	0.200	0.140	0.395	0.209	0.438	31.28	1.20E7	4.59E5	1.25E7
1	26	0.900	0.200	0.373	0.399	0.079	0.435	31.21	1.14E7	4.72E5	1.19E7
1	66	0.900	0.200	0.387	0.400	0.069	0.438	31.31	1.18E7	4.72E5	1.23E7
2	2	0.900	0.194	0.098	0.400	0.323	0.438	31.29	1.16E7	4.58E5	1.21E7
2	13	0.900	0.233	0.399	0.400	0.054	0.438	31.33	1.16E7	4.73E5	1.21E7
2	16	0.900	0.210	0.396	0.400	0.059	0.438	31.31	1.17E7	4.59E5	1.22E7
2	66	0.899	0.195	0.394	0.400	0.070	0.438	31.32	1.20E7	4.58E5	1.25E7
4	2	0.915	0.129	0.394	0.400	0.073	0.438	31.42	1.23E7	4.58E5	1.27E7
4	16	0.920	0.127	0.396	0.400	0.067	0.438	31.45	1.20E7	4.59E5	1.25E7
4	66	0.912	0.144	0.393	0.400	0.070	0.438	31.38	1.21E7	4.58E5	1.26E7

Appendix F

Result matrix trajectory optimisation using modified Newtonian database

Sp	Sd	x_{com}	z_{com}	c_{f1}	c_{f2}	L_{f1}	L_{f2}	Δt	ΔRe	Re_b	Re_e
1	2	0.841	0.152	0.087	0.400	0.022	0.437	31.50	1.17E7	4.35E5	1.21E7
1	13	0.843	0.155	0.092	0.400	0.006	0.438	31.51	1.18E7	4.35E5	1.22E7
1	16	0.832	0.149	0.053	0.400	0.111	0.438	31.41	1.23E7	4.48E5	1.27E7
1	26	0.843	0.155	0.019	0.400	0.022	0.437	31.46	1.17E7	4.35E5	1.21E7
1	66	0.843	0.155	0.019	0.400	0.022	0.437	31.46	1.17E7	4.35E5	1.21E7
2	2	0.833	0.149	0.011	0.400	0.104	0.438	31.47	1.17E7	4.35E5	1.21E7
2	13	0.827	0.153	0.047	0.400	0.103	0.438	31.41	1.23E7	4.48E5	1.27E7
2	16	0.835	0.137	0.025	0.400	0.652	0.438	31.29	1.25E7	4.49E5	1.30E7
2	26	0.841	0.133	0.210	0.400	0.074	0.438	31.26	1.22E7	4.49E5	1.27E7
2	66	0.848	0.138	0.158	0.400	0.071	0.437	31.27	1.22E7	4.49E5	1.27E7
3	2	0.700	0.198	0.046	0.242	0.091	0.433	30.84	1.23E7	4.52E5	1.28E7
3	13	0.700	0.237	0.028	0.274	0.002	0.400	30.82	1.13E7	4.52E5	1.18E7
3	16	0.700	0.189	0.007	0.365	0.003	0.262	30.83	1.18E7	4.52E5	1.22E7
3	26	0.700	0.167	0.123	0.232	0.022	0.426	30.81	1.23E7	4.52E5	1.28E7
3	66	0.700	0.258	0.031	0.266	0.077	0.427	30.34	1.22E7	4.52E5	1.27E7
4	13	0.842	0.160	0.086	0.400	0.012	0.438	31.50	1.18E7	4.35E5	1.22E7
4	16	0.850	0.154	0.022	0.399	0.052	0.438	31.50	1.18E7	4.35E5	1.22E7
4	26	0.850	0.154	0.022	0.399	0.052	0.438	31.50	1.18E7	4.35E5	1.22E7
4	66	0.833	0.154	0.030	0.400	0.042	0.438	31.31	1.16E7	4.48E5	1.21E7